博士論文

Microscopic understanding of electrochemical stability of lithium-ion battery electrolyte using molecular simulation

(分子シミュレーションに基づくリチウムイオン二次電池

電解液の電気化学的安定性の微視的解明)

宮﨑かすみ

Contents

List of abbreviations

AC	alternating current
AFM	atomic force microscopy
$BETI^-$	$N(SO_2C_2F_5)_2^-$
BO	Born-Oppenheimer
c-BC	*cis*-butylene carbonate
CPMD	Car-Parrinello molecular dynamics
CV	Cyclic Voltammetry
DFT	density functional theory
DMC	dimethyl carbonate
EC	ethylene carbonate
EIS	electrochemical impedance spectroscopy
FF	force field
FP	first-principles
FPMD	first-principles molecular dynamics
FTIR	Fourier transform infrared spectroscopy
GAFF	generalized AMBER force field
H-bond	hydrogen bond
HF	Hartree-Fock
HOMO	highest occupied molecular orbital
LCAO	linear combination of atomic orbital
LIB	lithium ion battery
LUMO	lowest unoccupied molecular orbital
MC	Monte Carlo
MD	molecular dynamics
MM	molecular mechanical
MO	molecular orbital
NMR	nuclear magnetic resonance
NR	neutron reflectometry
OTf^-	$SO_2CF_3^-$
PC	propylene carbonate
PDOS	projected density of states
PES	potential energy surface
$PTFSI^-$	$N(SO_2CF_3)(SO_2C_2F_5)^-$
QC	quantum chemical
QM	quantum mechaniccal
RDF	radial distribution function
RM	Red Moon
SA	simulated annealing
SCF	self-consistent field
SEI	solid electrolyte interphase
SEM	scanning electron microscopy
STM	scanning tunneling microscopy
t-BC	*trans*-butylene carbonate
TEM	transmission electron microscopy
$TFSI^-$	$N(SO_2CF_3)_2^-$
XPS	X-ray photoelectron spectroscopy
XRD	X-ray diffraction

Chapter 1 General introduction

1.1 Lithium ion battery

Among rechargeable batteries that can be charged and discharged repeatedly, high-power and compact lithium ion batteries (LIB) have been popularized mainly for small devices since the commercialization of LIBs in 1990s. [1, 2] Figure 1.1 schematically shows the basic structure and operating principle of LIB. LIB consists of a positive electrode, a negative one, and an electrolyte between the two. In LIB, Li ions transfer from the

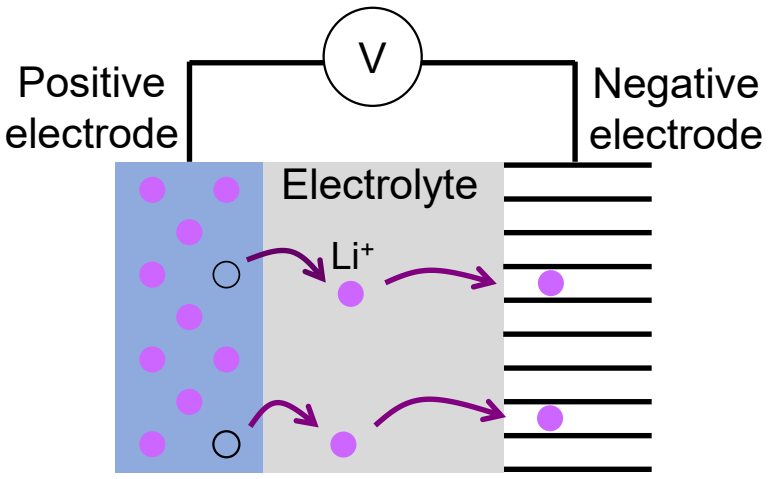

Figure 1.1: Schematic illustration of lithium ion battery. During the charging process, lithium ions move from the positive electrode to the negative electrode through the electrolytic solution as shown in the figure. Conversely, during the discharging process, lithium ions move from the negative electrode to the positive electrode.

positive electrode to the negative one through the electrolyte during a charging process, and vice versa during a discharging process. Nowadays, most of commercially available products of LIBs consist of $LiCoO_2$, graphite, and organic solvent-based $LiPF_6$ solutions for the positive, negative electrodes, and electrolyte, respectively.

In 2019, the Nobel Prize in Chemistry was awarded to three scientists, Whittingham, Goodenough, and Yoshino, who contribute to development of LIB. It is definite that the award reflects recent growth of social expectations and importance of LIB. For example, stable power supply becomes possible by using a temporary power storage facility even though stability of solar and/or wind power generations strongly depend on the weather. In addition, a conventional fossil fuel vehicle can be replaced by an electric one with an electric storage device. In anticipation of such social demands, LIB has been required to be applied to large-scaled devices. [3] However, to apply it to the large-scale devices, there are still rooms for its improvement in safety, cost, and performance. [4, 5] First of all, LIB is not inherently safe, and has a risk of ignition and explosion due to the use of flammable organic electrolyte. Secondly, the cost of lithium is not stable because of uneven distribution and rapidly growth of social demand of lithium. Thirdly, from the viewpoint of the performance, the energy density of a current LIB is insufficient for the application to electric vehicle (e.g., short cruising distance).

1.2 Electrolyte and solid electrolyte interphase

The improvement of the electrolyte leads to the resolution of many problems in LIB because the electrolyte is directly related to LIB's safety, cost, and performance. However, in comparison with the electrode materials, the development status of electrolytes is sluggish [6] due to the severe requirement of the electrolyte for LIB as follows:

1. High resistance to oxidation/reduction and stability against potential fluctuation.
2. Low viscosity and high ionic conductivity.
3. Staying liquid over a wide temperature range.
4. Inflammability, non-toxicity, and safety.
5. Forming a stable solid electrolyte interphase (SEI) film.

The formation of the SEI film is an essential condition for the electrolyte material because it controls the electrochemical stability of the electrolyte and governs the reversibility of Li^+ intercalation. The SEI film can be formed during the initial charging cycle as a result of the reductive decomposition of the electrolyte. It is known that this film can protect the electrolyte from the further reductive decomposition during the subsequent cycles, while allowing Li^+ to transfer to anode (as shown in Figure 1.2). As a result, the SEI film plays an important role to improve the electrochemical stability of the electrolyte. Furthermore, the SEI film can suppress a phenomenon called graphite exfoliation in which

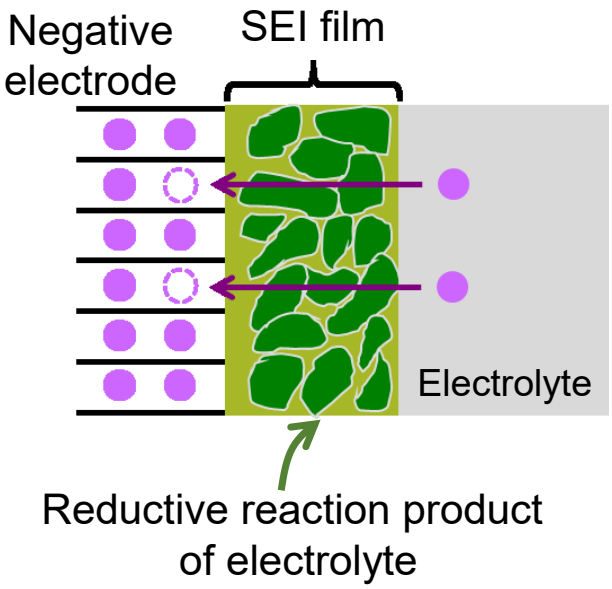

Figure 1.2: Schematic illustration of SEI.

layered structure of graphite is destroyed due to the co-intercalation into graphite of Li^+ and the coordinated solvent molecules.

The electrolyte used in commercially available LIBs is an ethylene carbonate (EC)-based organic electrolyte as shown in Figure 1.3. Except for EC, it contains c.a. 1 mol L^{-1} $LiPF_6$ as a Li salt and a linear carbonate such as dimethyl carbonate (DMC, Figure 1.3). The co-solvent such as DMC is added to dissolve EC because EC is solid at room temperature. This electrolyte has been used up to now even though it contains dangerous flammable organic solvents because there are few methods to form good SEI films without EC. For example, the propylene carbonate (PC) (Figure 1.4) [6] is one of promising candidates because the molecular property of PC is similar to that of EC andit is liquid at room temperature without co-solvent. However, when the pure PC-based electrolyte is used in LIB with the graphite anode, LIB loses the reversible charge-discharge property due to the graphite exfoliation. Although the formation of the SEI film strongly depends on

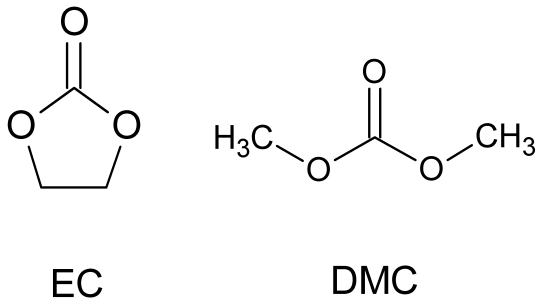

Figure 1.3: Structure of ethylene carbonate (EC) and dimethyl carbonate (DMC).

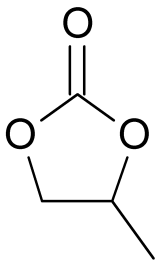

Figure 1.4: Structure of propylene carbonate (PC).

the selection of solvent molecules, its origin has not been elucidated since it is extremely difficult to directly observe the SEI film formation during the device operation in an experiment. [6]

However, the commercial organic electrolyte is insufficient to use for the LIB operation with high voltage. For example, since the electrolyte is not suitable in LIB with 5V-class electrode materials [7, 8], more durable electrolyte materials are required. Thus, it is necessary to develop a new electrolyte that satisfies safety, low cost, and high durability by controlling the formation of the SEI film.

Table 1.1: Kinds of experimental methods dealing with analysis of SEI film.

Category	Method	Properties
Electrochemistry	EIS, CV	Formation, evolution, ionic conductivity
Microscope	SEM, STM, TEM, AFM	Morphology, thickness
Spectroscopy	XPS, FTIR, XRD, Raman, NMR, NR	Chemical composition, morphology, thickness

1.3 Experimental observation of SEI

In this section, experimental methods to investigate SEI film formation are introduced. From the first observation of a passivation film on a Li metal anode in 1970 and a graphite anode in 1990, experimental researches to characterize the SEI film properties have been conducted so far. [9–11] The typical experimental methods for SEI film observation can be classified into three categories as summarized in Table 1.1. Overview of the experimental methods on the basis of the above three categories are given hereafter.

1. Electrochemical measurements

   Electrochemical measurement methods make use of the response against an electrical signal that is applied to the sample. The representative methods for SEI film analysis are electrochemical impedance spectroscopy (EIS) and Cyclic Voltammetry (CV). CV measurements are the basis for electrochemical measurements and are often used in LIB researches. In a CV measurement, the current value is monitored as a function of the applied potential to investigate the characteristics of the electrochemical reaction such as Li^+ co-intercaration into the graphite anode, reduction reactions at the interface including SEI film formation, and Li^+ intercaration. EIS is suitable for evaluating interfacial chemistry that consists of multiple kind of ion/electron transfer

processes. [12] In an EIS measurement, current to voltage ratio, i.e., the impedance is monitored as a function of the frequency of the applied alternating current (AC). Generally, timescales of Li^+/electron transport depend on each elementary process, e.g., Li^+ transport in bulk region of electrolyte and electrode, Li^+ transport in SEI film, and ion/charge transfer at interface. Namely, if an SEI film is formed on the anode surface, EIS can detect the formation by observing resistance originated from the film. Furthermore, EIS can evaluate not only whether SEI film is formed but also Li^+ conductivity in the film. The advantage of EIS is that it is non-destructive measurement under the condition of in situ. [13, 14] Note that it is very difficult to separate processes with similar timescale. Moreover, to understand the observed impedance changes, complex interfacial reactions should be modeled and interpreted as an appropriate model circuit. [12, 15]

2. Microscope

   Microscopes are mainly used to observe the surface state of an electrode. [15] Representative methods are scanning electron microscopy (SEM), transmission electron microscopy (TEM), scanning tunneling microscopy (STM), and atomic force microscopy (AFM). We can obtain an image of the surface states at micro to nano scale. For example, it is possible to know whether there is an SEI film or not by observing the surface of the electrode that has already undergone the charge-discharge cycle. Additionally, since AFM can detect the difference of the depth at the Angstrom resolution, it is useful to measure the thickness of the formed SEI film. Namely, we can obtain the 3D-image of the SEI film. [16] Furthermore, in situ AFM was

applied to observe the time evolution of the SEI film by Cresce et al. [17] The authors successfully described the SEI film evolution as a function of anode potential. In situ TEM technique is also one of the powerful tools to obtain time evolution of the SEI film. [18] It should be noted that the surface condition can be changed depending on the sample preparation procedure and/or damage by electron beam because these techniques are usually applied under the ex situ condition.

3. Spectroscopy

X-ray photoelectron spectroscopy (XPS) and Fourier transform infrared spectroscopy (FTIR) are representative methods that have been used to identify the components contained in the SEI film. [15] Since these methods have surface sensitivity, they are suitable for observing a thin layer of the SEI film. As will be mentioned later, such experimental identification of the SEI film components is also essential for simulation studies. In addition to these methods, X-ray diffraction (XRD), Raman spectroscopy, nuclear magnetic resonance (NMR), etc. are used to analyze the chemical composition and/or surface condition of SEI film. [15] Techniques of neutron spectroscopy, e.g., neutron reflectometry (NR), are also applied to reveal morphology and thickness of the SEI film because light elements such as hydrogen and lithium are sensitively detected by neutrons, which is quite difficult by the X-ray techniques. [19] Although these methods are indispensable for composition analysis of SEI film, its condition can change during the measurement because they are basically measured under ex situ conditions. For example, exposure to ambient should change the chemical composition of SEI film because of reaction with O_2,

CO_2, and H_2O. [6,15] Generally, samples of SEI film for ex situ analysis are prepared under an inert gas atmosphere to prevent such reactions. [15] Furthermore, there is possibility of SEI film dissolution during washing anode with electrolyte, which is also standard procedure for sample preparation. In fact, the results of SEI film composition analysis by various groups lack consistency. [20]

In summary, experimental measurement can reveal the following properties of the formed SEI film:

1. Existence of the film.
2. Micro to nano-order morphology.
3. Time evolution of the film shape, i.e., surface morphology and thickness.
4. Chemical composition.
5. Ionic conductivity.

In addition, the following has been proposed about SEI film experimentally: [6,9,14,20,21]

1. The films are formed during the first or the first few times of charging.
2. The films have a heterogeneous and complex composition due to various reductive decomposition reaction of electrolyte components.
3. The films have spatially non-uniform morphology.

4. The films have approximately tens of nanometers thick.

5. The films have layered structure with an inorganic compound inside and an organic compound outside.

1.4 Role of computational chemistry

Although experimental observations are effective for elucidating the chemical composition and morphology of SEI films, it is still difficult to observe directly the formation process, investigate thermodynamic and kinetic properties, and analyze the atomic level structure. [9] To cope with these difficulties, various kinds of computational chemistry methods have been performed.

In recent LIB researches, the contributions from computational chemistry are gaining importance. [22,23] By improving the performance of computers and developing theories and methods, the computational chemistry enables a deeper understanding of the phenomena in LIB that are difficult or impossible to investigate only by experiments. One of important contributions by the computational chemistry is to understand the SEI film formation mechanism that is difficult to investigate only by experiment. [22] By using quantum chemical (QC) calculations, we can obtain the transition state structures, activation barriers, and reaction energies for each elementary process. In fact, such calculations are indispensable to clarify the elementary reactions relating with the whole SEI film formation. On the other hand, by using the molecular simulations, we can investigate the three-dimensional geometric structure of SEI film at the atomic level.

Table 1.2: Kinds of molecular simulation methods dealing with SEI film formation.

Method	N_{atom}	time	Target properties
QC	10^2	-	Elementary reaction path and its potential energy
FPMD	10^2	10^1 ps	Elementary reaction path and its free energy
reactive MD (classical/ semiempirical)	10^3	10^3 ps	Elementary reaction path and its free energy
classical MD	10^5	10^5 ps	Transport and mechanical properties
Red Moon	10^5	equilibrium	Film formation process

In the computational chemistry, according to the target system and research purpose, it is important to select a suitable calculation method. The typical calculation methods used for computational researches on the SEI film formation are QC, first-principles molecular dynamics (FPMD), MD with the reactive force field (reactive MD), classical MD, and mixed Monte Carlo/MD simulation (Red Moon). [22] Table 1.2 shows the number of atoms handled, time scale, and computable properties obtained by each method. As shown in Table 1.2, it is impossible to elucidate the entire properties of SEI film formation only by one kind of simulation method. As shown in Table 1.2, it is impossible to elucidate the entire properties of SEI film formation only by one kind of simulation method.

As introduced in Chapter 2, there are various simulation methods based on computational chemistry. The combination of these methods is also important to solve the issues in LIB. Further, it is efficient to incorporate experimental knowledge that has already obtained into the computational calculations.

- QC

  As will be described in detail later, QC is the series of methods that calculate energies and electronic states of molecules on the basis of quantum mechanics. By using QC, we can obtain for example the transition state structures, activation barriers, and reaction energies for each elementary process. In the research of SEI film, QC was first applied to identify the reduction path of EC molecules by Li and Balbuena. [24] In the report, the authors constructed the reduction reaction pathways by calculating the plausible elementary reactions based on experimentally suggested SEI components. [25] In fact, such calculations are indispensable to clarify the elementary reactions relating to the whole SEI film formation because it is quite difficult to extract only a specific elementary reaction during the formation process of SEI film. Thus, there is a complementary relationship between chemical composition analysis of SEI film by experiment and reaction pathway analysis by QC. Generally, QC can be performed under the condition of gas phase or with implicit solvation model like polarizable continuum model (PCM).

- FPMD

  FPMD is series of methods for tracking the time evolution of dynamics of the system based on first-principles (FP) calculations. Generally, the target system of FPMD is larger than that of QC. The SEI film formation occurs in the electrolyte that contains both the ions and solvent molecules with high dielectric constant. Therefore, it is natural that Coulomb interactions between chemical species in the electrolyte become strong in comparison to those in the pure solvent. Such strong interactions

should affect the reactivity of each reactant. In such a case, the calculation with an explicit model is required. For example, although CO gas was observed as one of the reduction decomposition products from EC by experiment, [26] it was theoretically predicted for the first time by FPMD with an explicit model of solvent/graphite interface. [27]

Furthermore, by using FPMD, we can obtain not only thermodynamic properties, e.g., reaction free energy, but also kinetic properties, e.g., activation free energy of a chemical reaction. For example, Ushirogata et al. reported that in EC-based electrolyte, vinylene carbonate (VC) as an additive contributes to protection of anode by suppressing gas generation derived from two-electron reduction reaction of EC. [28] It is true that FPMD is the most accurate method to calculate energy and electronic states, however, it requires the huge computational power. As shown in Table 1.2, the time- and space-scales that can be handled by FPMD is limited due to its high calculation cost. In general, the target of FPMD is limited to tracking the system with a few degrees of freedom.

- Classical MD, reactive MD, and semiempirical MD

  In classical MD, energy calculations can be performed without much effort because it uses potential energy function that depends only on the nuclei configuration. This potential energy function is called force field (FF). Thus, the classical MD can be calculated much faster than FPMD. Namely, by employing classical MD, we can extend the limitation of number of atoms and simulation time. Usually, classical MD is used to investigate solution structure and transport properties. [9, 22, 23] However,

it cannot be applied to analyses of chemical reactions because breaking/formation of covalent bonds cannot be described by using general FF.

To overcome the limitation of classical MD, the semi-empirical MD and reactive FF, ReaxFF [29] are useful because they can treat qualitatively the chemical reactions. Nakai et al. have developed divide-and-conquer density-functional tight-binding (DC-DFTB) method [30] for massive-parallel computing environment, and applied it to the analyses on the structural and dynamical properties in secondary batteries [31–34]. On the other hand, reactive MD with ReaxFF is one of powerful simulation methods although the appropriate parameters are necessary for the target system. In fact, the reduction reaction pathways in EC-based electrolyte were investigated with the considerably large model (10^3 atoms) by applying improved method, eReaxFF. [28] However, since the calculation results of DC-DFTB and ReaxFF depend on the empirical parameters, it is necessary to perform the time-consuming parameter fitting for each target system. Thus, if there is no reference data, i.e., from experimental results and/or QC, for parameter fitting, it is difficult to predict the properties of new and unknown systems.

- Red Moon method

  The above three methods are generally used to analyze only a part of the SEI film formation process, e.g., elementary reaction. As explained in Chapter 2, it is difficult to observe chemical reactions only by MD simulation because we have to wait for the occurrence of chemical reactions which are rare events during the simulations. Nevertheless, in order to obtain an overall picture of the SEI film

formation process, we need to simulate the process from the initial state of the electrolyte-anode interface to formation of SEI film via a number of elementary reactions. Under the circumstances, Red Moon (RM) method developed by Nagaoka et al. is one of the methods that can achieve this objective. [35, 36] By combining the MD with the Monte Carlo (MC), RM simulation can simulate multiple chemical reaction process consisting of a lot of elementary reactions in a condensed phase. In addition to the information of formation process, we can obtain the morphology of SEI film at atomistic level because RM method is on the basis of an explicit atomistic model. In fact, RM has applied to EC and PC systems by Takenaka et al., [37] and revealed the difference of SEI film density between in EC and PC systems. Subsequently, the SEI film formation in various electrolytes have been investigated by RM simulation. [36, 38–41] The RM method can be an adequate technique to analyze the formation process and structure of the SEI film, however, it must be noted that some approximations are necessary. For example, RM needs to prepare a set of elementary reactions involved in the SEI film formation in advance. Usually, the dominant elementary reactions are selected by referring to the experimental composition analysis of the SEI film and the reaction pathway analysis by QC.

1.5 Purpose of this study

In this thesis, I aimed to elucidate the microscopic mechanism of electrochemical stability of electrolytes by molecular simulation.

First, in Chapter 3, I focused on geometric isomers, *cis*- and *trans*-2,3-butylene carbonates (*c*/*t*-BC) as the model electrolyte solvents. Despite their similar structure and chemical properties, *t*-BC-based electrolytes have been reported to enable the reversible reaction of graphite anodes (as in EC-based one), while *c*-BC-based electrolytes cause the exfoliation of graphite (as in PC-based one). To understand the microscopic origin of the different electrochemical behaviors of *t*-BC and *c*-BC, I applied Red Moon simulation to elucidate the microscopic SEI film formation processes.

Next, in Chapter 4, I investigated the origin of the tremendous stability of the hydrate-melt electrolyte, $Li(TFSI)_{0.7}(BETI)_{0.3}\cdot 2H_2O$, which possesses an extremely wide potential window. Aqueous electrolytes have great potential to improve the safety and production costs of LIB. To clarify the detailed liquid structure and electronic states of this unique aqueous system, a first-principles molecular dynamics study has been conducted.

Subsequently, in Chapter 5, I applied the present method to Na and K salt based hydrate melt electrolytes, and investigated the origin of the difference in the potential window between the different alkali cation's systems.

Chapter 2 Theoretical background

In computational chemistry, actual chemical systems are modeled based on theoretical chemistry, and numerical calculations are performed in simulations. In particular, molecular simulations are crucial to clarify the properties of molecules and molecular aggregates. In this chapter, the details are described focusing on the methods used in this study. The theoretical description in this chapter is based on Reference [42]

2.1 Energy calculation methods

Energy calculations of molecules and their aggregates are the basis of molecular simulations. Here, the energy calculation methods are divided into a quantum mechanical (QM) method that handles electrons in a quantum manner and a molecular mechanical (MM) method that utilizes empirical potential energy functions. The QM and MM are regarded as complementary methods, playing important roles in molecular simulations.

2.1.1 Quantum mechanical method

The molecules that form the assembly are made up of atoms, and the atoms consists of nuclei and electrons. Schrödinger's equations are fundamental to handle such nuclei and

electrons. For an electron bound by electrostatic potential from a nucleus, the following time-independent Schrödinger's equation is expressed as Eq. (2.1), is fundamental to the handling of nuclear and electron's quantum mechanics:

$$\left(-\frac{\hbar^2}{2m}\,\nabla^2 + V\right)\Psi(\boldsymbol{x}) = E\Psi(\boldsymbol{x}), \tag{2.1}$$

where m and $\hbar$ are the mass of electron and reduced Planck's constant, respectively. V indicates the external potential originated from nucleus. Ψ is a wave function of a four-dimensional coordinate $\boldsymbol{x}$ consisting of three position variables and one spin variable. E is an eigenvalue of operator $\left(-\frac{\hbar^2}{2m}\,\nabla^2 + V\right)$, which corresponds to the energy. The left-hand side of Eq. (2.1) is abbreviated as Hamiltonian, $\mathcal{H}$ as follows.

$$\mathcal{H}\Psi\left(\boldsymbol{x}\right) = E\Psi\left(\boldsymbol{x}\right). \tag{2.2}$$

$$E = \frac{\int \Psi\left(\boldsymbol{x}\right)^* \mathcal{H}\Psi\left(\boldsymbol{x}\right) d\boldsymbol{x}}{\int \Psi\left(\boldsymbol{x}\right)^* \Psi\left(\boldsymbol{x}\right) d\boldsymbol{x}}. \tag{2.3}$$

Solving Schrödinger's wave equation means finding the value of E, which is the eigenvalue of the Hamiltonian, and the wave function Ψ, which is the corresponding eigenfunction of E. These solutions describe the nature of the particles. In other words, we can analyze or predict the properties that depend on the electron distribution such as chemical reaction, by setting the Hamiltonian appropriately for the target atoms/molecules or their aggregates and finding Schrödinger's equation. However, the analytical solution of Schrödinger's equations is limited to the simple model systems such as a particle in quantum well or harmonic oscillator. In fact, although Schrödinger's equation for a hydrogen atom with one-electron can be solved analytically, it is impossible to obtain the analytical solution

for the equation of the multiple atoms containing two or more electrons. Therefore, series of molecular orbital (MO) methods with several approximations have been developed to obtain energies and wave functions in multielectron and/or polyatomic molecular systems. First, the Hartree-Fock (HF) method, which is the basis of MO methods and the starting point for more accurate approximation methods, is explained. Then, the density functional theory (DFT)-based MO method used in this study is introduced.

Hartree-Fock method [43]

For simplicity, the atomic unit system is used hereafter. Considering a system with M nuclei and N electrons, the Hamiltonian is given by

$$\mathcal{H} = -\sum_{i=1}^{N} \frac{1}{2}{\nabla_i}^2 - \sum_{A=1}^{M} \frac{1}{2M_A}{\nabla_A}^2 - \sum_{i=1}^{N}\sum_{A=1}^{M} \frac{Z_A}{|\mathbf{r}_i - \mathbf{R}_A|} + \sum_{i=1}^{N}\sum_{j>i}^{N} \frac{1}{|\mathbf{r}_i - \mathbf{r}_j|} + \sum_{A=1}^{M}\sum_{A>B}^{M} \frac{Z_A Z_B}{|\mathbf{R}_A - \mathbf{R}_B|}, \tag{2.4}$$

where $\mathbf{r}_i$ is position vector of ith electron, and M_A, Z_A, and $\mathbf{R}_A$ are mass, atomic number, and position vector for Ath nucleus, respectively. In Eq. (2.4), each term corresponds to kinetic energy of electrons, kinetic energy of nuclei, Coulomb attractive interaction between nuclei and electrons, repulsion interaction between nuclei, and repulsion interaction between electrons, respectively. By using the Born-Oppenheimer (BO) approximation, we can eliminate the second term and can consider the fifth term is constant in Eq. (2.4). The BO approximation is based on the idea that the motion of nuclei and electrons can be separately handled because the mass of the nucleus is much larger than that of the electron. Since adding an arbitrary constant to the operator does not affect the eigenfunction, only

the remaining three terms are enough to construct electronic Hamiltonian,

$$\mathcal{H}_{\mathrm{e}} = -\sum_{i=1}^{N} \frac{1}{2}{\nabla_i}^2 - \sum_{i=1}^{N}\sum_{A=1}^{M} \frac{Z_A}{|\mathbf{r}_i - \mathbf{R}_A|} + \sum_{i=1}^{N}\sum_{j>i}^{N} \frac{1}{|\mathbf{r}_i - \mathbf{r}_j|}. \tag{2.5}$$

Then, Schrödinger's equation with $\mathcal{H}_{\mathrm{e}}$ is given as

$$\mathcal{H}_{\mathrm{e}}\Psi_{\mathrm{e}} = E_{\mathrm{e}}\Psi_{\mathrm{e}}. \tag{2.6}$$

Equation (2.6) cannnot be solved due to its complexity of the system including N electrons. Thus, we introduce here a further approximation, i.e., independent-particle model, which treats the motion of one electron as being independent of the dynamics of all other electrons in the system. Under this approximation, we can set the one-electron Hamiltonian as follow.

$$f\left(i\right) = \left(-\frac{1}{2}{\nabla_i}^2 - \sum_{A=1}^{M} \frac{Z_A}{|\mathbf{r}_i - \mathbf{R}_A|}\right) + \sum_{j\neq i}^{N} \frac{1}{|\mathbf{r}_i - \mathbf{r}_j|} = \hat{h}\left(i\right) + \sum_{j\neq i}^{N} \frac{1}{|\mathbf{r}_i - \mathbf{r}_j|}. \tag{2.7}$$

The suitable eigenfunction for $f\left(i\right)$ is a one-electron wave function, i.e., orbital. Here, let $\chi(\boldsymbol{x})$ stands for one-electron spin-orbital which is a function of the four-dimensional coordinate $\boldsymbol{x}$. Generally, spin-orbitals are represented as the following linear combination of K atomic orbitals with appropriate coefficient c_{va}.

$$\chi_a\left(\boldsymbol{x}\right) = \sum_{v=1}^{K} c_{va}\varphi_v\left(\boldsymbol{x}\right). \tag{2.8}$$

Equation (2.8) is called linear combination of atomic orbital (LCAO) approximation. Here, the set of atomic orbitals used for expansion of spin-orbital is called basis function. Usually, we used more numbers of basis functions than the minimum one that can accommodate N electrons. Further, the wave function in Eq. (2.7) is expressed as the production of N

spin-orbitals,

$$\Psi_{\mathrm{e}} \approx \Psi^{\mathrm{HP}}\left(\boldsymbol{x}_1, \boldsymbol{x}_2, \cdots \boldsymbol{x}_N\right) = \chi_a\left(\boldsymbol{x}_1\right) \chi_b\left(\boldsymbol{x}_2\right) \cdots \chi_c\left(\boldsymbol{x}_N\right), \tag{2.9}$$

which satisfy the following orthogonal and normalized condition,

$$\int \chi_a \chi_b d\boldsymbol{x}_1 d\boldsymbol{x}_2 = \delta_{ab} \begin{cases} 1 \text{ if } a = b \\ 0 \text{ if } a \neq b. \end{cases} \tag{2.10}$$

However, the formulation of Eq. (2.9) is insufficient because there is no restriction on the anti-symmetry of the wave function. As shown in Eq. (2.11), the sign of the wave function becomes reversed for any commutation of electrons.

$$\chi_a\left(\boldsymbol{x}_1\right) \chi_b\left(\boldsymbol{x}_2\right) \cdots \chi_c\left(\boldsymbol{x}_N\right) = -\chi_a\left(\boldsymbol{x}_2\right) \chi_b\left(\boldsymbol{x}_1\right) \cdots \chi_c\left(\boldsymbol{x}_N\right) \tag{2.11}$$

In addition, Eq. (2.9) describes electrons as distinguishable particles, meaning that spin-orbitals $\chi_a, \chi_b, \cdots$ correspond to electrons $1, 2, \cdots$. The following Slater determinant is appropriate as a wave function description.

$$\Psi\left(\boldsymbol{x}_1, \boldsymbol{x}_2, \cdots \boldsymbol{x}_N\right) = \frac{1}{\sqrt{N!}} \begin{vmatrix} \chi_a\left(\boldsymbol{x}_1\right) & \chi_b\left(\boldsymbol{x}_1\right) & \cdots & \chi_c\left(\boldsymbol{x}_1\right) \\ \chi_a\left(\boldsymbol{x}_2\right) & \chi_b\left(\boldsymbol{x}_2\right) & \cdots & \chi_c\left(\boldsymbol{x}_2\right) \\ \vdots & \vdots & \ddots & \vdots \\ \chi_a\left(\boldsymbol{x}_N\right) & \chi_b\left(\boldsymbol{x}_N\right) & \cdots & \chi_c\left(\boldsymbol{x}_N\right) \end{vmatrix}. \tag{2.12}$$

In Slater determinant, the rows correspond to the electrons, while the columns correspond to the spin orbitals. Moreover, since the replacement of electrons corresponds to the replacement of rows, the sign is inverted, so that the anti-symmetry requirement is satisfied.

Furthermore, if two or more electrons occupy one spin orbital, the value of the determinant becomes 0, indicating that there is no such wave spaufunction. Namely, this condition satisfies Pauli's exclusion principle. Therefore, after expanding and organizing the Slater determinant, the energy E^{HF} of the N-electron system with the approximation is as follows:

$$\begin{aligned} E^{\mathrm{HF}} &= \int \Psi(\boldsymbol{x}_1, \boldsymbol{x}_2, \cdots \boldsymbol{x}_N)^* \mathcal{H}_{\mathrm{e}} \Psi(\boldsymbol{x}_1, \boldsymbol{x}_2, \cdots \boldsymbol{x}_N) d\boldsymbol{x}_1 d\boldsymbol{x}_2 \cdots d\boldsymbol{x}_N \\ &= \sum_{i=1}^{N} \sum_{a=1}^{N} \int \chi_a{}^* (\boldsymbol{x}_i)\, \hat{h}\,(i)\, \chi_a\,(\boldsymbol{x}_i)\, d\boldsymbol{x}_i \\ &+ \sum_{i=1}^{N} \sum_{j\neq i}^{N} \sum_{a=1}^{N} \sum_{b\neq a}^{N} \int \chi_a^*\,(\boldsymbol{x}_i)\, \chi_a^*\,(\boldsymbol{x}_i)\, \frac{1}{\left|\mathbf{r}_i - \mathbf{r}_j\right|} \chi_b\,\left(\boldsymbol{x}_j\right) \chi_b\,\left(\boldsymbol{x}_j\right) d\boldsymbol{x}_i d\boldsymbol{x}_j \\ &- \sum_{i=1}^{N} \sum_{j\neq i}^{N} \sum_{a=1}^{N} \sum_{b\neq a}^{N} \int \chi_a^*\,(\boldsymbol{x}_i)\, \chi_b^*\,\left(\boldsymbol{x}_j\right) \frac{1}{\left|\mathbf{r}_i - \mathbf{r}_j\right|} \chi_a\,\left(\boldsymbol{x}_j\right) \chi_b\,(\boldsymbol{x}_i)\, d\boldsymbol{x}_i d\boldsymbol{x}_j. \end{aligned} \tag{2.13}$$

The first term of last side of Eq. (2.13) is one-electron integral corresponding to sum of one-electron kinetic energy and potential energy originated from interaction with nuclei. The second and third terms are Coulomb and exchange integrals, respectively. Coulomb integral can be interpreted classically as Coulomb repulsion between two electron clouds. On the other hand, as for exchange integral, there is no such a classically interpretation, but it is interpreted as a correlation between two electrons having parallel spins (exchange energy).

According to the variational principle, the energy of the true wave equation is always smaller than that of the approximated solution. Then, we can find solution E^{HF} from a spin-orbital set that minimizes E^{HF} under the orthogonal and normalized condition of Eq. (2.10) with the method of Lagrange multiplier. Namely, the sum of the derivative of

the function is minimized, and the derivative of the Lagrange multiplier multiplied by the constraint is set to 0. By putting Lagrange multiplier λ, the equation is expressed by

$$\delta E^{\mathrm{HF}} + \delta \sum_{a=1}^{N} \sum_{b=1}^{N} \lambda_{ab} S_{ab} = 0, \tag{2.14}$$

where $S_{ab} (= \int \chi_a(\mathbf{r}) \chi_b(\mathbf{r}) d^3\mathbf{r})$ is overlap integral. Then, HF equation is derived as

$$\begin{aligned} \hat{h}(1)\chi_a(1) + \sum_{b \neq a} \left[\int |\chi_b(2)|^2 \frac{1}{|\mathbf{r}_i - \mathbf{r}_j|} d^3\mathbf{r}_2 \right] \chi_a(1) \\ - \sum_{b \neq a} \left[\int \chi_b{}^*(2)\chi_a(2) \frac{1}{|\mathbf{r}_i - \mathbf{r}_j|} d^3\mathbf{r}_2 \right] \chi_b(1) \\ = \varepsilon_a \chi_a(1) \\ (a = 1, 2, \cdots, N). \end{aligned} \tag{2.15}$$

For simplicity, $\hat{\mathcal{J}}_b(1)$ and $\hat{\mathcal{K}}_b(1)$ are introduced as operators corresponding to Coulomb and exchange integral, respectively.

$$\begin{aligned} \hat{\mathcal{J}}_b(1)\chi_a(1) &= \left[\int |\chi_b(2)|^2 \frac{1}{|\mathbf{r}_i - \mathbf{r}_j|} d^3\mathbf{r}_2 \right] \chi_a(1) \\ \hat{\mathcal{K}}_b(1)\chi_a(1) &= \left[\int \chi_b{}^*(2)\chi_a(2) \frac{1}{|\mathbf{r}_i - \mathbf{r}_j|} d^3\mathbf{r}_2 \right] \chi_b(1). \end{aligned} \tag{2.16}$$

Using Eq. (2.16), HF equation can be expressed as the following eigenvalue equation.

$$\begin{aligned} \left[\hat{h}(1) + \sum_a \left\{ \hat{\mathcal{J}}_b(1) - \hat{\mathcal{K}}_b(1) \right\} \right] \chi_a(1) = \varepsilon_a \chi_a(1) \\ (a = 1, 2, \cdots, N). \end{aligned} \tag{2.17}$$

However, the operator in the bracket of Eq. (2.17) includes Coulomb and exchange operators depending on the solution $\{\chi_a\}$. In the HF method, the following iterative method is applied.

1. A spin orbital set $\Psi(\boldsymbol{x}_1, \boldsymbol{x}_2, \cdots \boldsymbol{x}_N)$ is prepared as a trial function, and the HF equation is solved to obtain the Coulomb operator and the exchange operator.

2. Solve the equation again and obtain the second solution. $\Psi(\boldsymbol{x}_1, \boldsymbol{x}_2, \cdots \boldsymbol{x}_N)$ obtained as a solution is used in the next iteration.

3. The individual electronic solutions are gradually improved so that the total electron energy becomes low, and this operation is repeated until the results for all electrons remain unchanged.

The method of repeating until the input value matches the solution is called self-consistent field (SCF) method. By using this HF method, we can obtain nearly 99% of the exact energy of atoms and molecules. However, considering that even the electron energy of a hydrogen atom is about 300 kcal mol^{-1}, an error of 1% exceeds the accuracy of about 1 kcal mol^{-1} required for chemical discussions. This error is originated from insufficient description of the electronic correlation in the HF method. In the HF method, electrons are considered to move in the average potential created by other electrons. However, in reality, the electrons are moving while avoiding them to adopt a more stable electronic configuration more than they are described in the HF method. To solve this problem, a lot of methods for calculating more accurate energy by incorporating electron correlation have

been proposed. The methods are called Post-HF methods because they take an approach that starts with the solution of the HF equation. In the HF method, the wave function of the whole system is described as a single Slater determinant corresponding to the ground-state configuration. On the other hand, in the Post-HF method, we use the linear combination of multiple wave functions corresponding to configurations of excited state at unoccupied levels. Although these methods dramatically increase the calculation cost, it is possible to find the most accurate solution from small to medium molecules. Thus, the post-HF methods are used in situations where higher accuracy is required.

Density functional theory [44]

The HF method is an approach based on wave functions. On the other hand, the DFT is based on the Hohenberg-Kohn theorem where electronic energy of the ground state is uniquely determined by the electronic density. In the DFT, the electronic state and the energy of the system are calculated by using the electronic density. This means that the electronic energy can be expressed as a functional of electronic density, $E\left[\rho\left(\mathbf{r}\right)\right]$.

$$E\left[\rho\left(\mathbf{r}\right)\right] = \int V_{ext}\left(\mathbf{r}\right)\rho\left(\mathbf{r}\right)d\mathbf{r} + F\left[\rho\left(\mathbf{r}\right)\right]. \tag{2.18}$$

In Eq. (2.18), the first term on the right-hand side is the interaction between the electron and the external potential, and the second term is the sum of the kinetic energy of the electrons and the interaction between electrons. Since $E\left[\rho\left(\mathbf{r}\right)\right]$ becomes a minimum value when $\rho\left(\mathbf{r}\right)$ is a true ground state, $E\left[\rho\left(\mathbf{r}\right)\right]$ is obtained by a variational method as

in the HF method. Here, total number of electrons, N, is expressed as

$$N = \int \rho\left(\mathbf{r}\right) d\mathbf{r}. \tag{2.19}$$

and the equation with Lagrange multiplier becomes

$$\frac{\delta}{\delta\rho\left(\mathbf{r}\right)}\left[E\left[\rho\left(\mathbf{r}\right)\right] - \mu\int \rho\left(\mathbf{r}\right) d\mathbf{r}\right] = 0. \tag{2.20}$$

Suppose that the nuclei positions are fixed, i.e., V_{ext} is set as a constant, the following equation is derived:

$$\left(\frac{\delta E\left[\rho\left(\mathbf{r}\right)\right]}{\delta\rho\left(\mathbf{r}\right)}\right)_{V_{ext}} = \mu. \tag{2.21}$$

This equation corresponds to the Schrödinger equation of wave function theory. In the early DFT-based methods, the electronic density was described as a uniform electronic gas, that is, a model in which the electronic density was constant over the system. This model gives relatively good results for systems in which electrons are delocalized, e.g., the state of metal valence electrons under periodic boundary conditions, while it fails to describe chemical bonds in the molecular system of which electronic density is localized on chemical bonds. The application of DFT-based methods to molecular systems was accomplished based on an approximation method for $F\left[\rho\left(\mathbf{r}\right)\right]$ of Eq. (2.18) and orbitals by Kohn and Sham. In Kohn-Sham method, unknown $F\left[\rho\left(\mathbf{r}\right)\right]$ is approximated by three terms corresponding to kinetic energy, Coulomb energy between electrons, and exchange-correlation energy, expressed as

$$F\left[\rho\left(\mathbf{r}\right)\right] = E_{\mathrm{KE}}\left[\rho\left(\mathbf{r}\right)\right] + E_{\mathrm{H}}\left[\rho\left(\mathbf{r}\right)\right] + E_{\mathrm{XC}}\left[\rho\left(\mathbf{r}\right)\right]. \tag{2.22}$$

Note that the terms corresponding to kinetic energy and Coulomb energy between electrons are the same as HF method.

$$\begin{aligned} E_{\mathrm{KE}}\left[\rho\left(\mathbf{r}\right)\right] &= \sum_{i=1}^{N}\int \psi_i\left(\mathbf{r}\right)\left(-\frac{\nabla^2}{2}\right)\psi_i\left(\mathbf{r}\right)d\mathbf{r} \\ E_{\mathrm{H}}\left[\rho\left(\mathbf{r}\right)\right] &= \frac{1}{2}\iint \frac{\rho\left(\mathbf{r}_1\right)\rho\left(\mathbf{r}_2\right)}{\left|\mathbf{r}_1-\mathbf{r}_2\right|}\,d\mathbf{r}_1 d\mathbf{r}_2. \end{aligned} \tag{2.23}$$

In addition, the electronic density of the whole system is assumed to be equal to the sum of the electron densities of each orbital for a set of one electron orbitals (Kohn-Sham orbitals) ψ_i that satisfies the following normalized and orthogonal condition.

$$\rho\left(\mathbf{r}\right) = \sum_{i=1}^{N}\left|\psi_i\left(\mathbf{r}\right)\right|^2. \tag{2.24}$$

By combining these equations together with the electron-nucleus attractive term, the equation for calculating the energy can be written as

$$\begin{aligned} E\left[\rho\left(\mathbf{r}\right)\right] &= \sum_{i=1}^{N}\int \psi_i\left(\mathbf{r}\right)\left(-\frac{\nabla^2}{2}\right)\psi_i\left(\mathbf{r}\right)d\mathbf{r} \\ &+ \frac{1}{2}\iint \frac{\rho\left(\mathbf{r}_1\right)\rho\left(\mathbf{r}_2\right)}{\left|\mathbf{r}_1-\mathbf{r}_2\right|}\,d\mathbf{r}_1 d\mathbf{r}_2 + E_{\mathrm{XC}}\left[\rho\left(\mathbf{r}\right)\right] \\ &+ \sum_{A=1}^{M}\int \frac{Z_A}{\left|\mathbf{r}-\mathbf{R}_A\right|}d\mathbf{r}. \end{aligned} \tag{2.25}$$

One electron Kohn-Sham equation can be obtained by appropriate variational conditions as follow.

$$\left\{-\frac{{\nabla_1}^2}{2} - \left(\sum_{A=1}^{M}\frac{Z_A}{\left|\mathbf{r}-\mathbf{R}_A\right|}\right) + \int \frac{\rho\left(\mathbf{r}_2\right)}{\left|\mathbf{r}_1-\mathbf{r}_2\right|}d\mathbf{r}_2 + V_{\mathrm{XC}}\left[\mathbf{r}_1\right]\right\}\psi_i\left(\mathbf{r}_1\right) = \varepsilon_i\psi_i\left(\mathbf{r}_1\right), \tag{2.26}$$

where ε_i corresponds to orbital energy, and $V_{\mathrm{XC}}[\mathbf{r}_1]$ is exchange-correlation functional

$$V_{\mathrm{XC}}[\rho(\mathbf{r})] = \left(\frac{\delta E_{\mathrm{XC}}[\rho(\mathbf{r})]}{\delta\rho(\mathbf{r})}\right). \tag{2.27}$$

The above equation is solved by the SCF method in the similar way as the HF equation. The form and solution of the Kohn-Sham equation based on one-electron orbital, is in common with the HF equation. Furthermore, the computational cost of the DFT-based methods is comparable to or less than the HF method. The two methods treat the effects of exchange and electronic correlation in the different ways. In the HF method, the exchange term is formulated in the equation. However, other computational techniques are necessary to incorporate electronic correlation. On the other hand, DFT directly incorporates exchange and correlation effects through exchange-correlation functionals. When the energy is expressed as an electron density functional in Eq. (2.25), only the exchange correlation functional is unknown. That is, if an accurate exchange-correlation functional is known, the accurate energy including electronic correlation can be calculated. However, the true exchange correlation functional is not known. Fortunately, even when the exchange correlation functional is described as a relatively simple functional, the calculation results are accurate enough to discuss semi-quantitatively in chemistry. In the DFT-based method, to improve the calculation accuracy, the improvement of exchange correlation functional is indispensable because the systematic dealing such as the increase of the basis function as used in the HF method cannot be applied. The typical functionals are listed hereafter.

Local (spin) density approximation (L(S)DA)

Approximation based on uniform electron gas model. In this case, the exchange-correlation energy is expressed as

$$E_{\mathrm{XC}}\left[\rho\left(\mathbf{r}\right)\right] = \int \rho\left(\mathbf{r}\right)\varepsilon_{\mathrm{xc}}(\rho\left(\mathbf{r}\right))d\mathbf{r}, \tag{2.28}$$

and the exchange-correlation functional is obtained by,

$$V_{\mathrm{XC}}\left[\rho(\mathbf{r})\right] = \rho\left(\mathbf{r}\right)\frac{d\varepsilon_{\mathrm{xc}}(\rho\left(\mathbf{r}\right))}{d\rho\left(\mathbf{r}\right)} + \varepsilon_{\mathrm{xc}}\left(\rho\left(\mathbf{r}\right)\right), \tag{2.29}$$

where $\varepsilon_{\mathrm{xc}}$ is exchange-correlation energy per electron. LDA assumes a uniform electron density within the volume element. Usually, $\varepsilon_{\mathrm{xc}}(\rho\left(\mathbf{r}\right))$ is expressed by an analytic function of electronic density. One of the examples is the following Gunnarsson-Lundqvist formula.

$$\begin{aligned}
\varepsilon_{\mathrm{xc}}\left(\rho\left(\mathbf{r}\right)\right) &= -\frac{0.458}{r_s} - 0.0666G\left(\frac{r_s}{11.4}\right) \\
G\left(x\right) &= \frac{1}{2}\left[(1+x)\log\left(1+x^{-1}\right) - x^2 + \frac{x}{2} - \frac{1}{3}\right] \\
{r_s}^3 &= \frac{3}{4\pi\rho\left(\mathbf{r}\right)}.
\end{aligned} \tag{2.30}$$

The Gunnarsson-Lundqvist equation uses a single function, but it is common to consider exchange energy and correlation energy separately. In that case, the following formula is often used as the exchange energy.

$$E_{\mathrm{X}}^{\mathrm{LSDA}}\left[\rho_\alpha\left(\mathbf{r}\right), \rho_\beta\left(\mathbf{r}\right)\right] = -\frac{3}{2}\left(\frac{3}{4\pi}\right)^{\frac{1}{3}}\int\left(\rho_\alpha{}^{\frac{4}{3}}\left(\mathbf{r}\right) + \rho_\beta{}^{\frac{4}{3}}\left(\mathbf{r}\right)\right)d\mathbf{r}, \tag{2.31}$$

where $\rho_\alpha\left(\mathbf{r}\right)$ and $\rho_\beta\left(\mathbf{r}\right)$ correspond to density of up and down spin, respectively. On the other hand, there are various formulations for the correlation energy. For example, the

Perdew-Zunger equation is

$$\varepsilon_{\mathrm{C}}\left(\rho\left(\mathbf{r}\right)\right)=\begin{cases}\dfrac{-0.1423}{\left(1+1.9529{r_s}^{\frac{1}{2}}\right)+0.3334r_s} & (r_s\geq 1)\\ -0.0480+0.0311\ln r_s-0.0116r_s+0.0020r_s\ln r_s & (r_s<1)\end{cases} \tag{2.32}$$

and Vosko-Wilk-Nusair equation is

$$\begin{aligned}\varepsilon_{\mathrm{C}}\left(\rho\left(\mathbf{r}\right)\right) &= \frac{A}{2}\left\{\ln\frac{x^2}{X\left(x\right)}+\frac{2b}{Q}\tan^{-1}\left(\frac{Q}{2x+b}\right)\right.\\ &- \left.\frac{bx_0}{X\left(x_0\right)}\left[\ln\frac{\left(x-x_0\right)}{X\left(x\right)}+\frac{2\left(b+2x_0\right)}{Q}\tan^{-1}\frac{Q}{2x+b}\right]\right\},\\ x &= {r_s}^{\frac{1}{2}},\ X\left(x\right)=x^2+bx+c,\ Q=\left(4c-b^2\right)^{\frac{1}{2}}\\ A &= 0.0621814,\ x_0=-0.409286,\ b=13.0720,\ c=42.7198.\end{aligned} \tag{2.33}$$

Generalized gradient approximation (GGA)

To improve the accuracy of the approximation, an extended theory of LDA approximation has been developed. GGA that considers not only the density but also its gradient is the most common method. A typical exchange functional is the following formula proposed by Becke:

$$E_{\mathrm{X}}^{\mathrm{B88}}\left[\rho\left(\mathbf{r}\right)\right]=E_{\mathrm{X}}^{\mathrm{LSDA}}\left[\rho\left(\mathbf{r}\right)\right]-b\sum_{\sigma=\alpha,\beta}\rho_\sigma^{\frac{4}{3}}\frac{x_\sigma^2}{1+6bx_\sigma\sinh^{-1}x_\sigma}d\mathbf{r}$$
$$x_\sigma=\frac{\left|\nabla\rho_\sigma\right|}{{\rho_\sigma}^{\frac{4}{3}}},\ b=0.0042\ \text{a.u.} \tag{2.34}$$

A correlation functional was proposed by Lee-Yang-Parr as follows.

$$\begin{aligned} E_{\mathrm{C}}^{\mathrm{LYP}}[\rho(\mathbf{r})] &= -a \int \frac{1}{1+d\rho^{-\frac{1}{3}}} \left\{ r + b\rho^{-\frac{2}{3}} \left[C_{\mathrm{F}}\rho^{-\frac{5}{3}} \right.\right. \\ &- \left.\left. 2t_w + \left(\frac{1}{9}t_w + \frac{1}{18}\nabla^2\rho \right) \right] e^{-cr^{-1/3}} \right\} d\mathbf{r} \\ t_w(\mathbf{r}) &= \sum_{i=1}^{N} \frac{|\nabla\rho_\alpha(\mathbf{r})|^2}{\rho_\alpha(\mathbf{r})} - \frac{1}{8}\nabla^2\rho, \;\; C_{\mathrm{F}} = \frac{3}{10}\left(3\pi^2\right)^{\frac{2}{3}} \\ a &= 0.049, \; b = 0.132, \; c = 0.2533, \; d = 0.349 \end{aligned} \tag{2.35}$$

A combination of Becke's exchange functional and Lee-Yang-Parr's correlation functional is widely used as BLYP.

Hybrid-GGA

In HF method, the exact exchange energy with independent-particle model is formulated. Then, in Hybrid-GGA functional, the exchange energy $\varepsilon_{\mathrm{X}}^{\mathrm{exact}}$ by the HF method is obtained from a set of Kohn-Sham orbitals and used in combination with LDA and GGA. Among them, the following Becke's B3 hybrid functional is often used.

$$\begin{aligned} E_{\mathrm{XC}}^{\mathrm{B3}} = E_{\mathrm{XC}}^{\mathrm{LSDA}} + a_0\left(E_{\mathrm{X}}^{\mathrm{exact}} - E_{\mathrm{X}}^{\mathrm{LSDA}}\right) + a_{\mathrm{X}}\Delta E_{\mathrm{X}}^{\mathrm{B88}} + a_{\mathrm{C}}\Delta E_{\mathrm{C}}^{\mathrm{GG}} \\ a_0 = 0.20, a_{\mathrm{X}} = 0.72, a_{\mathrm{C}} = 0.81 \end{aligned} \tag{2.36}$$

Here, $E_{\mathrm{C}}^{\mathrm{GG}}$ is a GGA correction of the correlation functional, and the combination of the B3 functional and the LYP functional is the most commonly used functional as B3LYP.

2.1.2 Morecular mechanical method

QM methods are computationally expensive and difficult to use in molecular simulations where a lot of energy calculations are necessary for a large number of molecular assemblies. On the other hand, by using the MM method, it is possible to execute the energy calculations without much effort because it uses potential energy function that depends only on the nuclei configuration. In the MM method, under the assumption the BO approximation, the motion of electrons can be ignored, and the electron density of the whole molecule is assigned to each atom as a set of point charge. Most of the molecular simulations of large scale systems use the potential function prepared based on the MM method, i.e., force field (FF) for energy calculation. Many of the molecular FFs describe intra- and inter-molecular forces with the four terms shown in Figure 2.1. The FF is described by using the position of N particles $\mathbf{R}^N$ as follows:

$$\begin{aligned} V\left(\mathbf{R}^N\right) &= \sum_{\text{bonds}} \frac{k_i}{2}\left(l_i - l_{i,0}\right)^2 \\ &+ \sum_{\text{angles}} \frac{k_i}{2}\left(\theta_i - \theta_{i,0}\right)^2 + \sum_{\text{torsions}} \frac{V_n}{2}\left[1 + \cos\left(n\omega - \gamma\right)\right]^2 \\ &+ \sum_{i}^{N}\sum_{j>i}^{N}\left(\frac{q_i q_j}{4\pi\varepsilon_0\left|r_j - r_i\right|} + 4\varepsilon_{ij}\left[\left(\frac{\sigma_{ij}}{\left|r_j - r_i\right|}\right)^{12} - \left(\frac{\sigma_{ij}}{\left|r_j - r_i\right|}\right)^{6}\right]\right). \end{aligned} \tag{2.37}$$

The first, second, and third terms of Eq. (2.37) indicate bond-streching, bending of bond angle, and bond rotation, respectively. These three terms correspond to the intramolecular forces. In the first and second terms, the energetic penalty due to the deviation from the reference bond length $l_{i,0}$ and bond angle $\theta_{i,0}$ is calculated based on the spring (harmonic

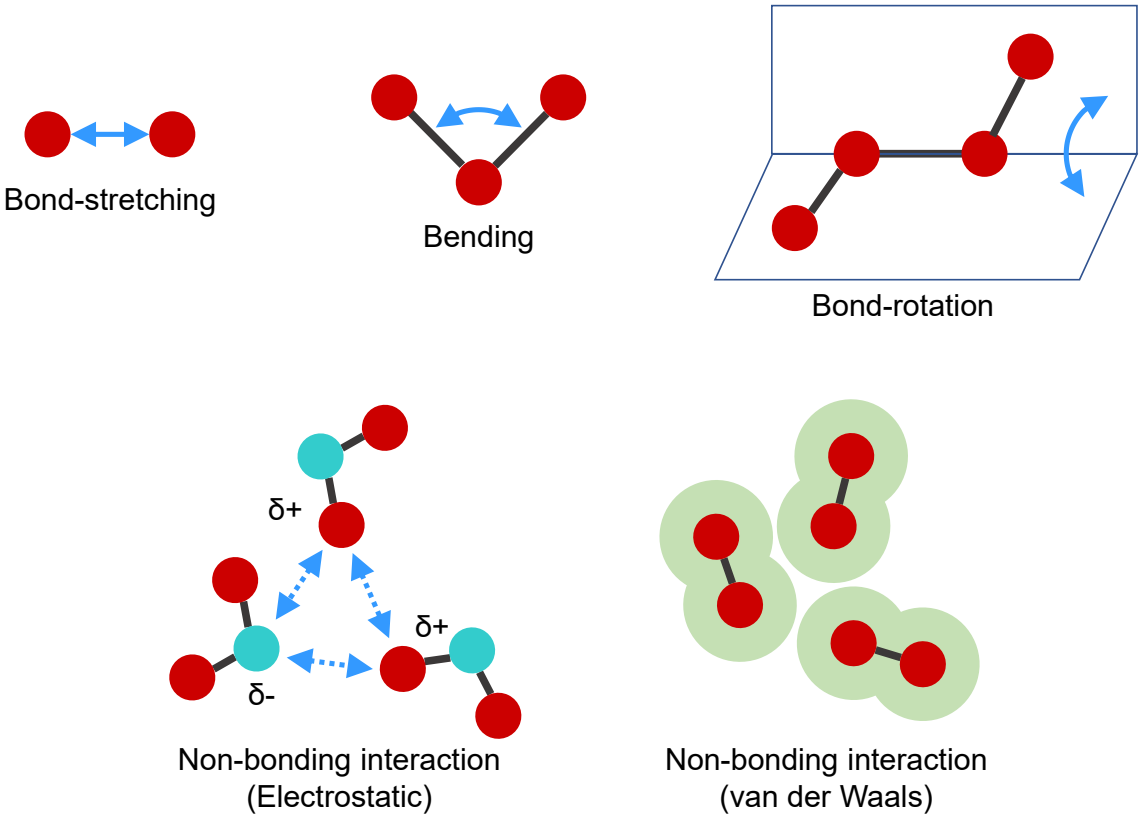

Figure 2.1: Main terms contributing to intra/intermolecular mechanics.

oscillator) model. The third term describes the potential change according to the angle of bond rotation. The fourth term corresponds to the intermolecular force consisting of non-bonded interactions, i.e., electrostatic potential and van der Waals interaction for all atom pairs. Eq. (2.37) includes empirical parameters, k_i, V_n, and σ_{ij}. A molecular FF is prepared by assembling a functional system and its associated parameters to reproduce the results of experiments and/or precise QM calculations. In many cases, the fitting of FF parameters is necessary for the specific target system. In molecular simulations with well-defined FFs, structure and thermodynamic quantities of molecular groups can be reproduced with considerable accuracy. Since the number of calculations is greatly increased as the number of atoms increases, MM-based molecular simulations are quite

useful for the large-scaled systems that are impossible to use the QM method. However, the MM method is less versatile than QM, and is difficult to predict the properties of new and unknown systems where there are few experimental results. Furthermore, in many cases, it is not possible to describe chemical reactions involving bond breakage/generation that greatly change the electronic state.

2.2 Molecular simulations

This section gives an overview of the Monte Carlo (MC) method and the molecular dynamics (MD) method, which are typical methods for molecular simulation. To simulate a system consisting of N atoms, $3N$ coordinate components ($\{\mathbf{r}_1, \mathbf{r}_2, \cdots, \mathbf{r}_N\} \equiv \mathbf{R}^N$) and $3N$ momentum components are required to define a state of the system. This space composed of a $6N$ dimensions is called a phase space. Generally, molecular simulations are executed by assuming BO approximation. Thus, the potential energy is a function of nuclear coordinates $\mathbf{R}^N$. Since the dimension of $\mathbf{R}^N$ is $3N$, its potential energy $V\left(\mathbf{R}^N\right)$ is a hypersurface defined by $3N$-dimensional variables. This is called the potential energy surface (PES). In principle, if the potential energies corresponding to all points in the phase spaces of the system, i.e., entire PES can be obtained, we can obtain an accurate partition function by summing up Boltzmann factors. However, except when the target system is a small molecule consisting of several atoms, it is computationally impossible to search all of the phase space. Thus, in a molecular simulation, it is important to search efficiently a phase space that has a huge dimension.

2.2.1 Monte Carlo method

The MC method refers to a series of techniques for obtaining statistical information by repeating random sampling. In the Random sampling, we have to create a system state with (pseudo) random numbers. This technique is widely used not only for molecular simulations but also for other computational simulations. In the MC-based molecular simulation, the particle position $\mathbf{R}^N$ consisting of $3N$ dimensions is randomly generated to sample the potential energy and objective physical quantity. This operation searches for a point on the structural phase space that does not contain momentum coordinates at random. However, the number of sampling points are limited due to the computational cost. Moreover, most of sampling points in the phase space correspond to the structures that have low stability, a very low appearance rate, and very little contribution to the partition function. For these reasons, it is extremely difficult to calculate an accurate physical quantity by the uniform sampling. To solve this problem, an efficient sampling method to choose the point with a large contribution to the distribution function is required. The typical method is the Metropolis method shown below (Figure 2.2).

1. Generate the initial configuration $\mathbf{R}_0^N$ of the system and calculate the potential energy $V\left(\mathbf{R}_0^N\right)$.

2. Generate the next configuration $\mathbf{R}_1^N$ by random numbers and calculate $V\left(\mathbf{R}_1^N\right)$. Generally, a generation method that changes a part of the previous configuration $\mathbf{R}_0^N$ is used.

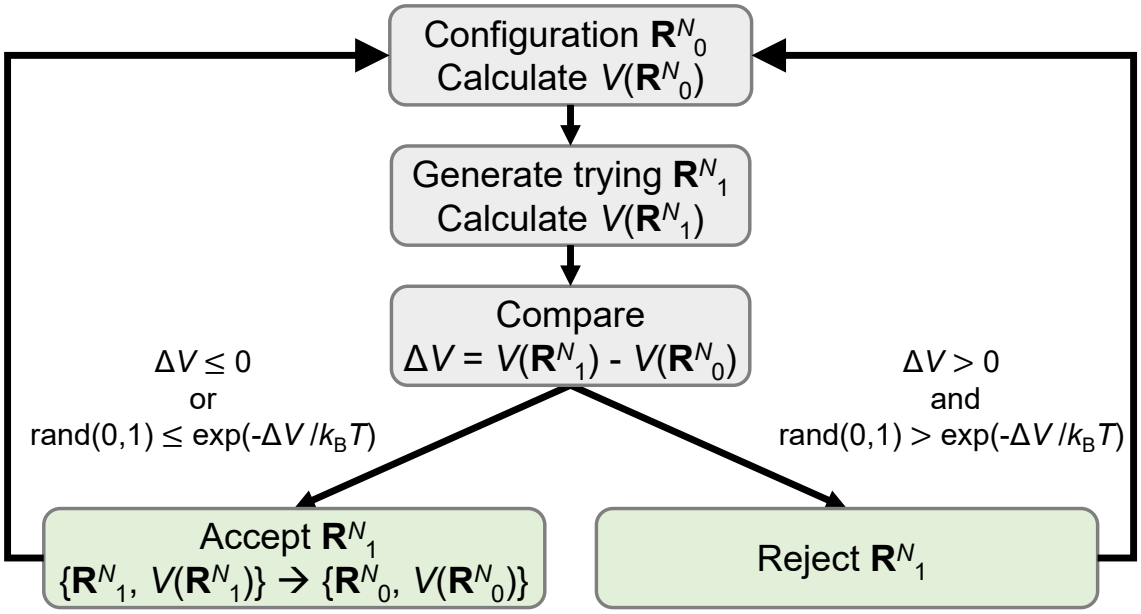

Figure 2.2: Schematic flowchart of Metropolis method.

3. Compare $V\left(\mathbf{R}_0^N\right)$ and $V\left(\mathbf{R}_0^N\right)$. If the energy of configuration $\mathbf{R}_1^N$ is lower than that of $\mathbf{R}_0^N$, namely, $\Delta V = V\left(\mathbf{R}_1^N\right) - V\left(\mathbf{R}_0^N\right)$, accept $\mathbf{R}_1^N$. In the case of $\Delta V > 0$, acceptance or rejection of $\mathbf{R}_1^N$ is judged using a random number between 0 and 1, rand $(0, 1)$. Accept $\mathbf{R}_1^N$ if rand $(0, 1) \leq \exp\left(-\frac{\Delta V}{k_B T}\right)$, otherwise reject it.

4. If accepted, replace $\mathbf{R}_1^N$ as new $\mathbf{R}_0^N$; if rejected, do not change $\mathbf{R}_0^N$. Then, return to step 1.

In the Metropolis method, it is possible to sample focusing on stable configurations that greatly contributes to the partition function. Also, even if the configuration has higher energy than that of previous one, if ΔV is small, the acceptance possibility of the configuration is relatively high because the Boltzmann factor approaches 1. MC simulation based on Metropolis method is fundamental in molecular simulation.

In addition, by changing the value of a variable T included in the Boltzmann factor, it is possible to change the acceptance rate of the unstable configurations. A typical method using this scheme is simulated annealing (SA). SA is a method that simulates the annealing process in which a molten material is slowly cooled to form a large single crystal. SA is often used for optimization problems because it is effective to look for the minimum even for the phase space that might have many local minima. In typically SA, T is initially set to a large value and gradually decreased. This operation corresponds to searching most stable configuration with wider sampling around the phase space because larger T increases probability of acceptance of unstable configuration and vice versa.

In general, the MC method has a lower calculation cost per sampling than the MD method, which is described later. It has an advantage in quick convergence for calculating a physical quantity in an equilibrium state and for structure optimization. Also, the algorithm is simple and easy to implement. However, it is often difficult to construct the random sampling method which has efficiency and physical meaning. Furthermore, since the MC method generally does not include time-series information, the MD method is required to calculate a time correlation function such as a diffusion coefficient.

2.2.2 Molecular dynamics method

The molecular dynamics (MD) method refers to a method of tracking the time evolution of particle position and velocity based on the equation of motion. In general MD simulations, time evolution of nuclear motion is tracked under the BO approximation. The equation

of motion when the force F_{xi} is applied from the direction x_i in the nucleus of mass m_i is given as follows:

$$\frac{d^2x_i}{dt^2} = \frac{F_{xi}}{m_i}. \tag{2.38}$$

In the case of molecular simulation, the force acting on the particle is obtained as a spatial derivative of potential energy. In the potential energy calculation, there are a case where the above-described QM calculation is used and a case where a FF is used. Among the former, those based on FP calculations are called FPMD. The latter is called classical MD or MMMD. In any case, the force acting on the particles is a complex function depending on the positional relationship with a huge number of other particles. Therefore, the differential equation cannot be solved analytically and is generally solved by the difference method. Figure 2.3 shows a schematic diagram of MD simulation progress based on the difference method. In the difference method, the integration interval is equally divided by a minute time Δt, and the integration is performed in each interval. The force acting on each particle at time t is calculated, and the acceleration of the particle is obtained. At this time, if the force is constant between time t and $t + \Delta t$, the position and velocity of the particle at $t + \Delta t$ can be obtained. By repeating this MD step, the trajectory of the time change of the particles in the system is obtained.

There are many integration algorisms for equations of motion using the difference method. Algorithms often used in molecular simulation are the Verlet method, the velocity Verlet method, the Leap-frog method, etc. A common assumption in these algorithms is that mechanical properties such as position, velocity, and acceleration can be approximated

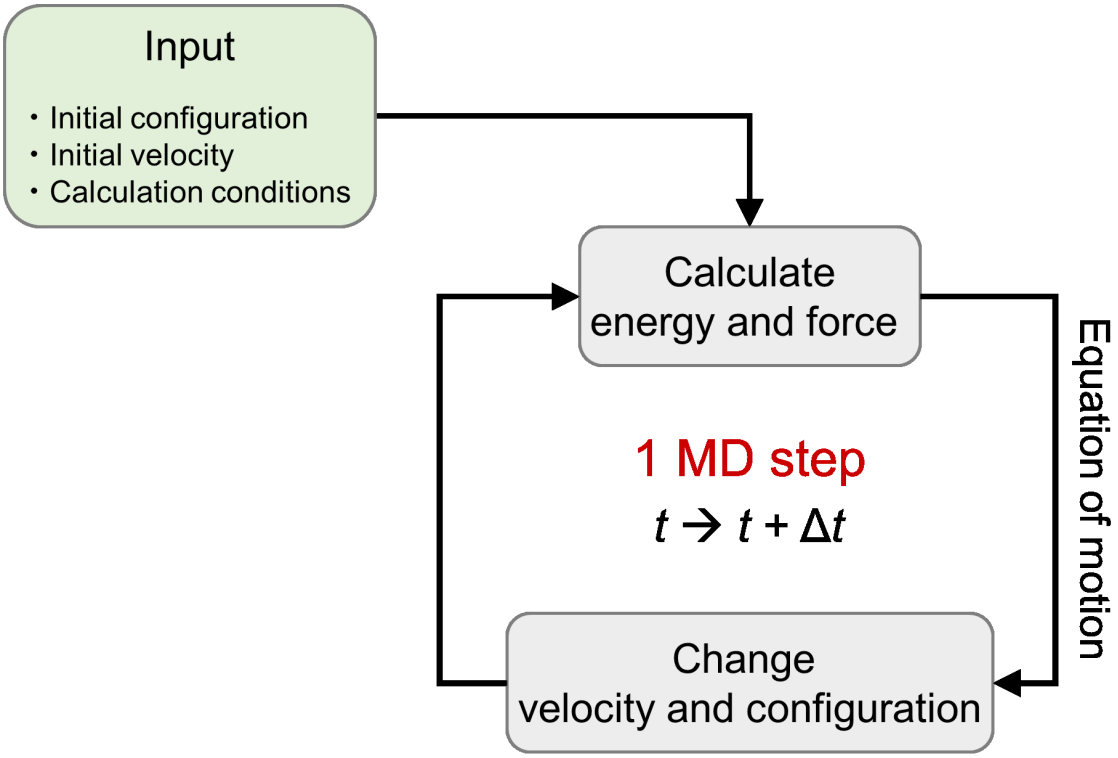

Figure 2.3: Schematic flowchart of molecular dynamics method.

by a Taylor series expansion equation. Suppose that the position, first derivative, second derivative, and third derivative are symbolized **r**, **v**, **a**, and **b**, respectively, the Taylor expansion is expressed as

$$\mathbf{r}(t+\Delta t) = \mathbf{r}(t) + \mathbf{v}(t)\,\Delta t + \frac{1}{2}\mathbf{a}(t)\,\Delta t^2 + \frac{1}{6}\mathbf{b}(t)\,\Delta t^3 + \cdots . \tag{2.39}$$

In the Verlet method, to calculate a new position $\mathbf{r}(t+\Delta t)$ at time $(t+\Delta t)$, position $\mathbf{r}(t)$ and acceleration $\mathbf{a}(t)$ at time t and the position $\mathbf{r}(t-\Delta t)$ of the previous step as shown below,

$$\mathbf{r}(t-\Delta t) = \mathbf{r}(t) - \mathbf{v}(t)\,\Delta t + \frac{1}{2}\mathbf{a}(t)\,\Delta t^2 - \frac{1}{6}\mathbf{b}(t)\,\Delta t^3 + \cdots . \tag{2.40}$$

Adding each side of Eqs. (2.39) and (2.40), the terms after the third order are deleted as

follows:

$$\mathbf{r}(t+\Delta t) = 2\mathbf{r}(t) - \mathbf{r}(t-\Delta t) + \mathbf{a}(t)\Delta t^2. \tag{2.41}$$

Although this equation does not include the velocity, it can be easily calculated as follows:

$$\mathbf{v}(t) = \frac{\mathbf{r}(t+\Delta t) - \mathbf{r}(t-\Delta t)}{2\Delta t}. \tag{2.42}$$

The Verlet method has the following advantages: it is simple and requires less storage capacity because it uses only one acceleration and two positions for each MD step. However, Eq. (2.41) is the sum of the difference between large numbers (first and second terms) and the very small value (third term), which causes an error in numerical calculation. In addition, the velocity at time t cannot be obtained until the calculation of the position at the next $\mathbf{r}(t+\Delta t)$ is completed. Since there is no information on the previous step at the start time, it must be estimated separately. Due to these drawbacks, other methods such as Leap-frog method and velocity Verlet method have been proposed.

In the Leap-frog method, the average acceleration between time $t - \frac{1}{2}\Delta t$ and $t + \frac{1}{2}\Delta t$ is assumed to be equal to the acceleration at time t, which is the midpoint, and the velocity at time $t + \frac{1}{2}\Delta t$ is calculated from the velocity at time $t - \frac{1}{2}\Delta t$ and the acceleration at time t,

$$\mathbf{v}\left(t + \frac{1}{2}\Delta t\right) = \mathbf{v}\left(t - \frac{1}{2}\Delta t\right) + \mathbf{a}(t)\Delta t. \tag{2.43}$$

Next, assuming that the average velocity between time t and $t + \Delta t$ is equal to the velocity at time $t + \frac{1}{2}\Delta t$, which is the midpoint, the position at time $t + \Delta t$ is calculated from velocity

at $t + \frac{1}{2}\Delta t$ and the position at time t as follows:

$$\mathbf{r}(t + \Delta t) = \mathbf{r}(t) + \mathbf{v}\left(t + \frac{1}{2}\Delta t\right)\Delta t. \tag{2.44}$$

The velocity at time t can also be calculated as follows:

$$\mathbf{r}(t) = \frac{1}{2}\left[\mathbf{v}\left(t - \frac{1}{2}\Delta t\right) + \mathbf{v}\left(t + \frac{1}{2}\Delta t\right)\right]. \tag{2.45}$$

This method overcomes the disadvantages of the Verlet method, i.e., the velocity is absent in the equation and the difference between large numbers should be calculated. However, a new drawback arises in that the velocity and position cannot be calculated simultaneously. Namely, the total energy cannot be calculated from the potential energy and the kinetic energy.

On the other hand, the velocity Verlet method is a method that can simultaneously calculate the position, velocity, and acceleration with improvement of the calculation accuracy at the expense of additional calculation costs. First, the position at time $t + \Delta t$ calculated from the velocity and acceleration at time t, as follows:

$$\mathbf{r}(t + \Delta t) = \mathbf{r}(t) + \mathbf{v}(t)\Delta t + \frac{1}{2}\mathbf{a}(t)\Delta t^2. \tag{2.46}$$

Subsequently, the velocity at time $t + \frac{1}{2}\Delta t$ is calculated by

$$\mathbf{r}\left(t + \frac{1}{2}\Delta t\right) = \mathbf{v}(t) + \frac{1}{2}\mathbf{a}(t)\Delta t, \tag{2.47}$$

and a new velocity at $t + \Delta t$ is obtained with $\mathbf{a}\,(t + \Delta t)$,

$$\mathbf{v}\,(t + \Delta t) = \mathbf{v}\left(t + \frac{1}{2}\Delta t\right) + \frac{1}{2}\mathbf{a}\,(t + \Delta t)\,\Delta t. \tag{2.48}$$

Additionaly, there are many other numerical integration algorithms such the Beeman methods and predictor-corrector method. An appropriate one is selected in consideration of the calculation cost, the magnitude of Δt, and the conditions such as ensemble to be used.

Fist-principles molecular dynamics based on Car-Parrinello method [45, 46]

The following describes the Car-Parrinello (CP) method, which is one of the FPMD methods. Car-Parrinello molecular dynamics (CPMD) is slightly different from the MD framework introduced so far.

If we want to follow the chemical reaction or apply the MD method to a new system with insufficient data, it is desirable to perform the first-principle MD, in which the potential energy and the force of each MD step are obtained from the FP calculation. Even if the FP calculation is a method based on the HF method or DFT, the energy calculation requires optimization of the set of orbitals by the SCF method. Along with the increase in the number of atoms in the target system, a huge calculation cost proportional to the third or more power is required. Therefore, it is difficult to apply to MD simulations that need to perform FP calculation many times.

On the other hand, the CP method can realize FPMD with reduced calculation costs by the following procedure:

1. Combine molecular dynamics and SA to minimize electron energy in a nuclei configuration (in the SCF method, that corresponds to convergence).

2. Using the above nuclei configuration and electronic structure as the initial structure, solve the equations of motion of electrons and nuclei simultaneously.

Under the BO approximation, a point on the PES is expressed with a set of Kohn-Sham orbitals $\{\psi_i\}$, a set of nuclear coordinates $\{\mathbf{R}_I\}$, and an external constraint by constants of volume condition, etc., $\{\alpha_v\}$,

$$\begin{aligned} E\left[\{\psi_i\},\{\mathbf{R}_I\},\{\alpha_v\}\right] &= \sum_i \int_\Omega {\psi_i}^*(\mathbf{r})\left[-\frac{\hbar^2}{2m_\mathrm{e}}{\nabla_i}^2\right]\psi_i(\mathbf{r})\,d^3\mathbf{r} \\ &+ U\left[n(\mathbf{r}),\{\mathbf{R}_I\},\{\alpha_v\}\right], \end{aligned} \tag{2.49}$$

where Ω and $n(\mathbf{r})$ $(=\sum_i |\psi_i(\mathbf{r})|^2)$ indicates the volume and the electronic density of the system, respectively. In Eq. (2.49), U includes repulsion between nuclei, attractive force between nuclei and electrons, and the exchange-correlation term. To consider the dynamics of parameters of E, namely, $\{\psi_i\}$, $\{\mathbf{R}_I\}$, and $\{\alpha_v\}$, Lagrangian L can be written

as

$$\begin{aligned} L &= \sum_i \frac{1}{2}\mu \int_\Omega \left|\dot{\psi}_i\right|^2 d^3\mathbf{r} \\ &+ \sum_I \frac{1}{2} M_I \dot{\mathbf{R}}_I{}^2 + \sum_v \frac{1}{2}\mu_v \dot{\alpha_v}{}^2 \\ &- E\left[\{\psi_i\}, \{\mathbf{R}_I\}, \{\alpha_v\}\right] \\ &+ \sum_{i,j} \Lambda_{ij} \left(\int_\Omega \psi_i{}^* (\mathbf{r}, t)\psi_j (\mathbf{r}, t)\, d^3\mathbf{r} - \delta_{ij} \right), \end{aligned} \tag{2.50}$$

where the dot indicates time derivative, M_I is mass of nucleus I, μ and μ_v are parameters corresponding to mass in the dynamics, and Λ_{ij} is Lagrange multiplier. Note that the last term of the r.h.s. of Eq. (2.50) has come from the normalized and orthogonal constraint of $\{\psi_i\}$, i.e., $\int_\Omega \psi_i{}^* (\mathbf{r}, t)\psi_j (\mathbf{r}, t)\, d^3\mathbf{r} = \delta_{ij}$. From the above, a set of the equation of motion for $\{\psi_i\}$, $\{\mathbf{R}_I\}$, $\{\alpha_v\}$ is as follows:

$$\begin{aligned} \mu\ddot{\psi}_i (\mathbf{r}, t) &= \frac{\delta E}{\delta \psi_i{}^* (\mathbf{r}, t)} + \sum_{i,j} \Lambda_{ij}\psi_j (\mathbf{r}, t) \\ M_I\ddot{\mathbf{R}}_I &= -\nabla_{R_I} E \\ \mu_v\ddot{\alpha_v} &= -\frac{\partial E}{\partial \alpha_v}. \end{aligned} \tag{2.51}$$

Kinetic energy K is given by

$$K = \sum_i \frac{1}{2}\mu \int_\Omega \left|\dot{\psi}_i\right|^2 d^3\mathbf{r} + \sum_I \frac{1}{2} M_I \dot{\mathbf{R}}_I{}^2 + \sum_v \frac{1}{2}\mu_v \dot{\alpha_v}{}^2. \tag{2.52}$$

In Eqs. (2.51) and (2.53), terms and equations of motion for $\{\psi_i\}$ and $\{\alpha_v\}$ are virtual and have no meaning for actual physical system. These terms and equations are the tools for execution of CPMD. For example, if $\{\psi_i\}$ is optimized, it corresponds to the electronic

ground state, and $\ddot{\psi}_i$ and kinetic energy become 0. In this case, the eigenvalue of Λ_{ij} coincides with the set of eigenvalues obtained by the Kohn-Sham equation. As long as this condition is satisfied, CPMD is identical to the BOMD, then it can describe the actual physical picture.

In CPMD, the system is first optimized by combining SA and MD according to Eq. (2.51) so that the other kinetic energies are zero while the nuclear configuration is fixed. Then start MD to move the nuclear configuration. The trajectory is obtained according to the Eq. (2.51) within a range in which the kinetic energy except for the nuclear is very small compared with the nuclear kinetic energy. If it goes out of this range, the optimization is performed to make kinetic energy except for the nuclear zero.

As described above, by avoiding the SCF calculation, the computational cost for each MD step can be greatly reduced. However, with CPMD, it is necessary to make the time step smaller than when performing SCF calculation at every MD step, resulting in larger number of MD steps.

2.3 Red Moon method

In this section, we explain the Red Moon (RM) method, [35, 36] which can simulate a stepwise reaction consisting of multiple elementary reaction processes in a condensed phase by combining MC and MD methods.

The probability of appearance of a high energy state that can cross the barrier of

chemical reaction is very low compared to a low energy state. The chemical reaction with the order of seconds to hours that we observe daily is familiar to us. However, it becomes difficult to observe these reactions directly by molecular simulation because the FPMD simulation can be handled a much smaller range of up to 10^3 atoms and 10^{-10} seconds. Therefore, chemical reactions are rare events that are difficult to observe even with a single elementary reaction, simply by performing an MD simulation. For this problem, Blue Moon ensemble [47, 48], which sets a limit on the movement of the reactant to the direction along the reaction coordinates, and Meta-dynamics method [49], which prohibits pass again the point on the free energy surface once passed to sample a wide phase space in a shorter time, have been developed. However, even with these methods, it is only possible to observe the elementary reaction processes one by one. With conventional MD methods, it is hard to deal with a complex reacting system such as multiple kinds of elementary reactions occur one after another while competing in a condensed phase.

The Red Moon (Rare Event-Driving MethOdology Of Necessity) method, developed by Nagaoka et al., is a technique that enables simulation of complex reacting systems. In RM method, by repeating the MC/MD cycle, it is possible to follow the stepwise change of the system that consists of the accumulation of elementary reactions. A MC/MD cycle consists of two parts: the MC part selects a possible elementary reaction by Metropolis method and the MD part describes the dynamics of molecules in the system. This method enables a simulation from an initial state to an equilibrium state where no elementary reaction occurs in a system with 10^5 atoms. The detailed procedure is as follows:

1. Preparation for RM simulation. Prepare an initial structure to start RM simulation and set the simulation parameters, i.e., a list of elementary reactions and conditions for selecting as a reaction candidate. The condition as a reaction candidate is, for example, approach of an atomic pair where a bond is generated after the reaction. It is set as a threshold value of an interatomic distance.

2. Start the simulation. Let r be the configuration state of the current system, and search for molecules and atom pairs that satisfy the conditions as reaction candidates.

3. If the number of candidates N_{cand} is 0, namely, no reaction candidate is found and the RM simulation itself has not converged, perform a short MD to update the state r and the procedure returns to 1. If it has converged, stop the simulation. If $N_{\mathrm{cand}} < 0$, select one from all candidate by weighted selection with Boltzmann factor of activation energy E_{a}, $\exp\left(-\frac{E_{\mathrm{a}}}{k_{\mathrm{B}}T}\right)$.

4. Create a state s which corresponds to the state after occurring the selected reaction. For example, if selected reaction is A + B $\rightarrow$ C, apply a molecular force field parameter of C to a group of atoms constituting A + B in state r, and then perform a short MD simulation to relax whole systems.

5. Compare the potential energy of state r with that of state s to decide whether to accept or reject the selected reaction by the Metropolis method. The energy difference ΔU_{rs} used at this time is

$$\Delta U_{rs} = U_r - U_s = \left(U_r^{\mathrm{MM}} - U_s^{\mathrm{MM}}\right) + \Delta U_0^{\mathrm{reac}}, \tag{2.53}$$

where U_r^{MM} and U_s^{MM} are potential energy by molecular mechanics and $\Delta U_0^{\mathrm{reac}}$ is reaction potential energy of the selected one. $\Delta U_0^{\mathrm{reac}}$ is calculated by quantum chemical methods under the condition of gas phase with correction of zero-point energy. If $\Delta U_{rs} \leq 0$ or rand $(0, 1) \leq \exp\left(-\frac{E_{\mathrm{a}}}{k_{\mathrm{B}}T}\right)$ accept state s, otherwise reject the state.

6. If accepted, state s is newly set as state r, and the initial configuration is updated. Otherwise, the process returns to candidate selection in step 3.

7. Stop the RM simulation when there is almost no change in the composition of the system (corresponds to the equilibrium state).

RM method was first applied to the simulation of the racemization of 2-chlorobutane in *N*,*N*-dimethylformamide solvent. [35] From the system that consists only of (*R*)-2-chlorobutane and has an optical purity of 100% as an initial state, a composition close to a racemate is finally obtained by the RM simulation. Further, it is applied successfully to the formation of an aromatic polyamide film, [50] the formation of a solid electrolyte interphase (SEI) film for secondary batteries, [36–41] and an olefin polymerization. [51]

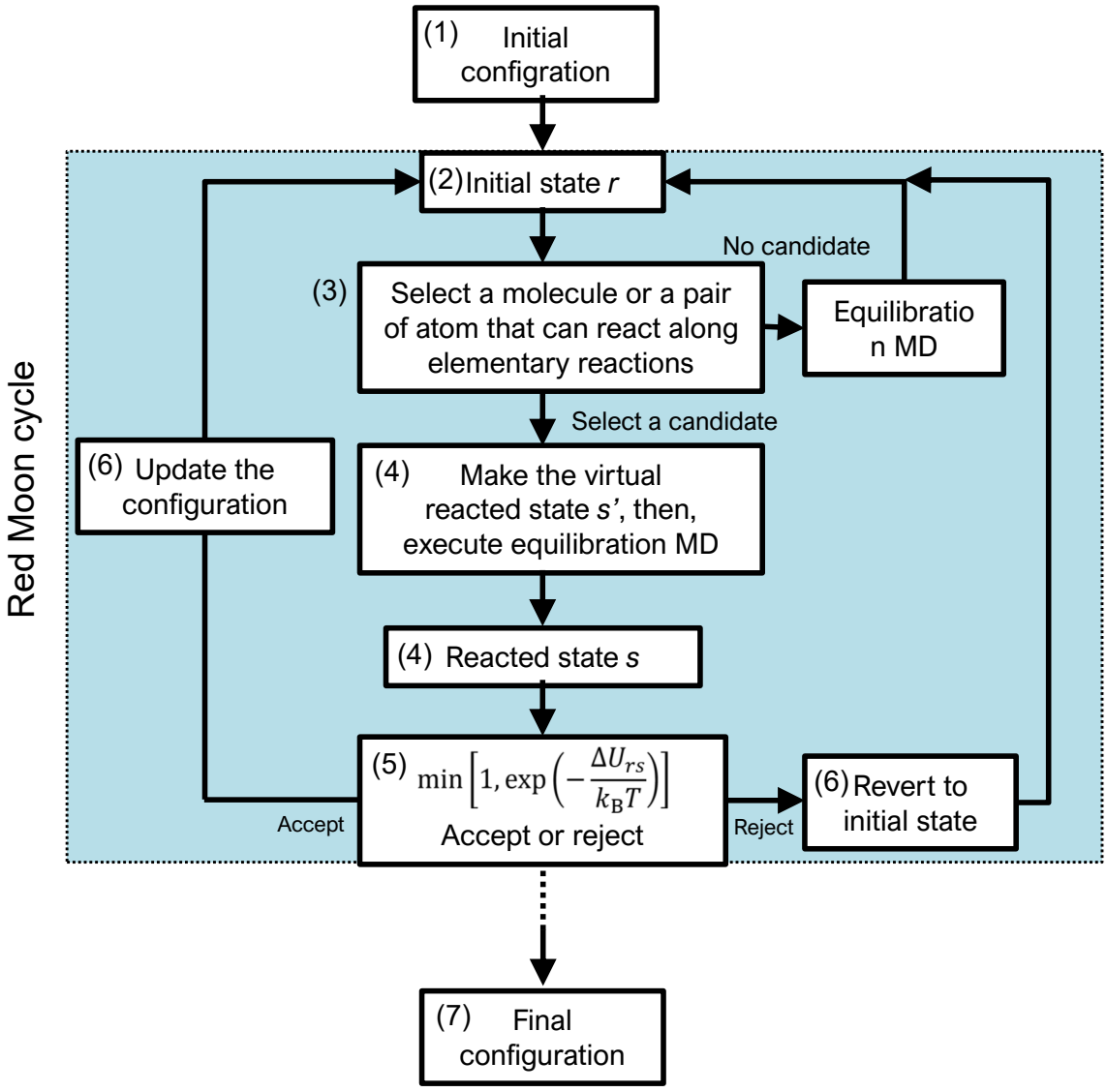

Figure 2.4: Schematic flowchart of molecular dynamics method.

Chapter 3 Impact of *C*is- versus *T*rans-Configuration of Butylene Carbonate Electrolyte on Microscopic SEI Formation Processes in LIBs

3.1 Introduction

Although the use of LIBs in small-scale devices is widespread, increasing focus is now being directed into applying them to large-scale devices such as electric vehicles and renewable energy storage equipment, in response to social demands. [3] These applications require the development of higher energy-density battery systems, but generally, having a higher energy density increases the risk of fire and/or explosion from a flammable electrolyte. [4] It is therefore challenging to develop a safe LIB with a high energy density and a long lifetime. An SEI film is key for achieving a stable battery performance. [6, 14, 15, 52, 53] An SEI film is a passive layer, which is formed by the reductive decomposition of the electrolyte on anode materials during the first charging process, enables electron blocking while also maintaining the permeability of the Li^+. SEI films prevent electrolytes from undergoing undesirable continuous reductive decomposition, which otherwise causes an increase in the irreversible capacity, exfoliation of graphite anodes, and gas evolution, and has other negative impacts on batteries. Of particular importance when designing

SEI films is their strong dependence on the electrolyte solvent. The most representative examples are the distinctive features observed in EC and PC. EC-based electrolytes are used in most commercialized LIBs, because of their ability to form a good SEI film on the graphite anode's surface, thus protecting the electrolyte against reductive decomposition. PC-based electrolytes, however, cannot form SEI films, despite only differing slightly from EC (only one additional methyl group). Concerning this phenomenon, referred to as "EC-PC mystery," [6] previous studies have applied RM simulation, [35, 36] thereby revealing the microscopic origins of the different SEI film formation processes in EC and PC electrolytes. [37] It is claimed that SEI film components cannot aggregate efficiently in PC electrolytes, as compared to their aggregation in EC, because the methyl group in PC exerts steric hindrance towards the formation of a dense and stable SEI film. Therefore, SEI film formation is very sensitive to the molecular structures and their interactions, during the elemental processes of reductive decomposition and deposition. In contrast, through their previous research on the "EC/PC mystery," Xing et al. proposed that the stronger solvation ability of PC enhances the formation of the anion-free solvation structure of $Li^+(PC)_4$ as a result of competitive solvation by anions and solvent molecules, and thus hinders the LiF production associated with the reduction of PF_6^- anions. [54] A similar relationship to the "EC-PC mystery" has also been found in other cyclic carbonates: *t*-BC versus *c*-BC. [55] These molecules have the same atomicity and structure, except for their cis-trans geometry (Figure 3.1); here, the difference between the two is even smaller than that of EC and PC. Moreover, each provides the same product following a one-electron reductive ring-opening reaction of a single molecule. [56] It has been reported, however,

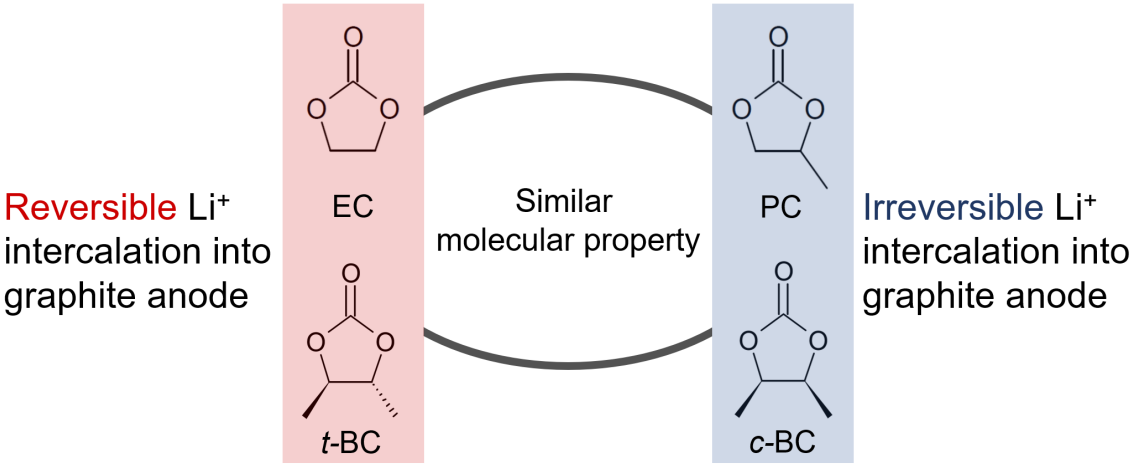

Figure 3.1: Distinct electrochemical behaviors of *t*-BC and *c*-BC electrolytes, despite their similarity at the molecular level.

that a *t*-BC-based electrolyte enables the reversible intercalation of Li^+ into graphite anodes, similar to EC, while a *c*-BC-based electrolyte causes irreversible exfoliation of graphite, similar to PC. [55, 57] This implies that only the cis-trans geometry in single molecules can be changed to effectively modify the microscopic formation of SEI films, and hence achieve reversible Li^+ intercalation into a graphite anode.

Although SEI films have been observed on graphite anodes in *t*-BC elertrolyte, [56] no one has reported the existence of SEI films in *c*-BC electrolyte. Therefore, the dependence of the SEI film formation process on the orientation of two methyl groups in geometric isomers remains a debatable issue. Computational simulation is an effective tool for unveiling the details of the SEI film formation processes, considering the difficulty of experimental in-situ surface observations under electrochemical conditions. In particular, RM simulation [35, 36] is suitable for the observation of the SEI film formation process at the atomistic level. SEI film formation is the result of numerous sequential elementary reactions in a condensed electrochemical system, dealing with large numbers of atoms

over a long time period. The RM method is able to efficiently simulate such systems, with explicit description of the surrounding environment. [35–41, 50, 51] Indeed, RM simulations have been successfully applied to unveil the origin of the "EC-PC mystery," [37] and explore the effects of additives, [38, 39] and the results have revealed the SEI formation process in a highly concentrated electrolyte. [41] In this study, RM simulations were performed to investigate the differences in the SEI film formation process on a graphite anode in both 1 mol L^{-1} $LiPF_6$/*t*-BC and 1 mol L^{-1} $LiPF_6$/*c*-BC. First, we analyzed the differences in the SEI films, quantified by their mass density, and by the number of each reaction component in each film. Second, we attempted to clarify the origin of distinct SEI film formation routes in the *t* and *c*-BC electrolytes, to determine the solvation effect. Finally, we discuss the analogies between *t*/*c*-BC and EC/PC, to obtain a general perspective on how SEI film formation is affected by the electrolyte solvent.

3.2 Method

3.2.1 Model system

The SEI film formation process was simulated using the RM method to clarify the origin of different electrochemical behaviors experimentally observed in *t*-BC and *c*-BC. RM simulations were executed with the primary chemical reactions shown in Figure 3.2, which were assumed based on previous experimental and theoretical studies. [37,56,58,59] Here, we ignore the reactions of linear carbonates, because in most cases, the reduction of cyclic carbonates is known to be dominant. [56,59] The main components are therefore generated

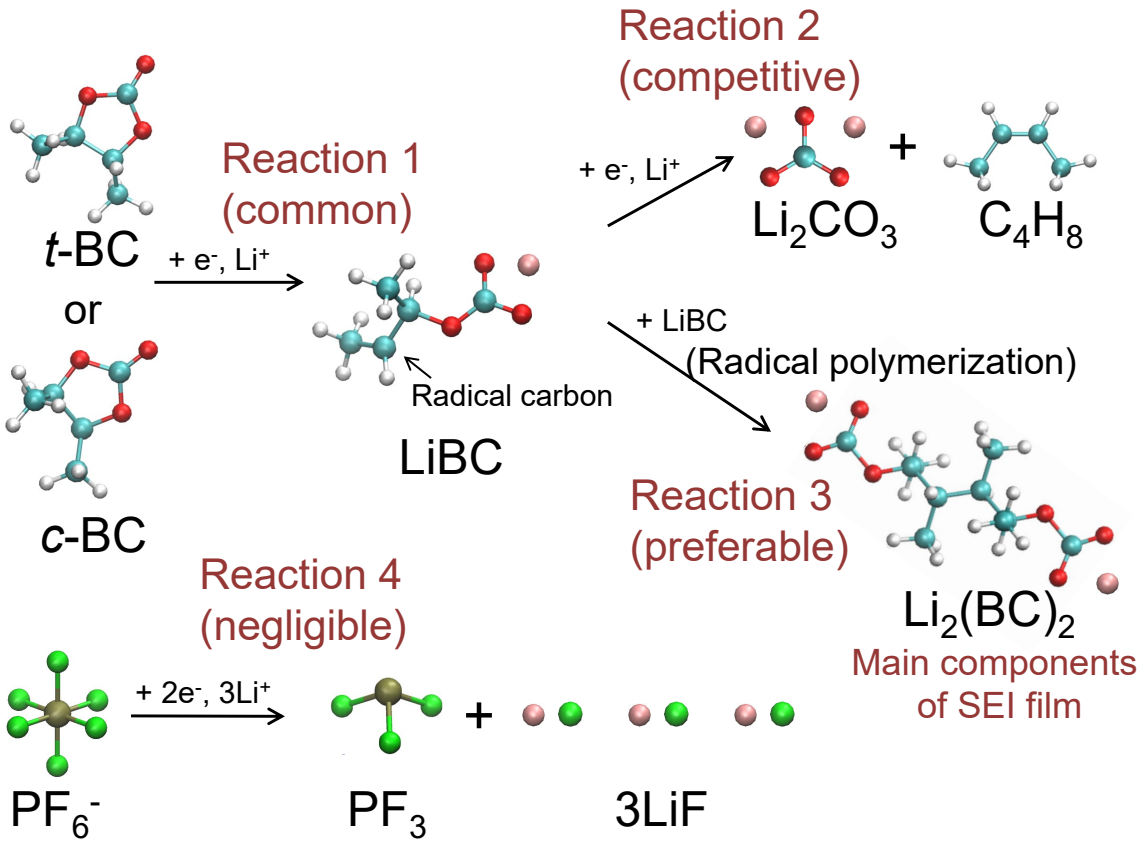

Figure 3.2: Primary chemical reactions of SEI film formation in the *t*/*c*-BC-based 1 M $LiPF_6$ electrolyte. The important features of each reaction found from simulation results are shown in parentheses.

from cyclic carbonate, regardless of the existence of any linear carbonates that may act as co-solvents. In this regard, we employed Reactions 1-3 as the primary decomposition reactions of *t*-BC and *c*-BC. Additionally, we applied two-electron reduction of the PF_6^- anion on the graphite anode. [58] In this study, the chemical reactions associated with the direct attack of radical ("LiBC" in Figure 3.2) to solvents, i.e., *t*/*c*-BC was not included because such reactions are assumed to be the endothermic one in the EC electrolyte as reported in the FPMD simulation. [28] The details of RM simulations may be found in previous reports. [36, 37, 41] In this study, we calculated the reaction energy, ΔU_{rs}, using

Table 3.1: Reaction energy of each primary elementary reaction [kcal mol^{-1}]

Reaction	$\Delta U_0^{\mathrm{reac}}$	$\Delta \overline{U}_{rs}^{\mathrm{MM(sol)}}$
1-a) *t*-BC + Li^+ + e^- → LiBC	-1.3	-55.5
1-b) *c*-BC + Li^+ + e^- → LiBC	-3.0	-45.5
2) LiBC + Li^+ + e^- → Li_2CO_3 + C_4H_8	0.3	77.6
3) 2LiBC → $Li_2(BC)_2$	-4.3	87.1
4) PF_6^- + $2e^-$ + $3Li^+$ → PF_3 + 3LiF	110.2	-0.5

Eq. (3.1):

$$\begin{aligned} \Delta U_{rs} &= \Delta U_{rs}^{\mathrm{MM}} + \Delta U_0^{\mathrm{reac}} - \Delta \overline{U}_{rs}^{\mathrm{MM(sol)}} \\ &= \Delta U_{rs}^{\mathrm{MM(sol)}} + \Delta U_{rs}^{\mathrm{MM(sol-svt)}} + \Delta U_0^{\mathrm{reac}} - \Delta \overline{U}_{rs}^{\mathrm{MM(sol)}} \end{aligned} \tag{3.1}$$

where $\Delta U_{rs}^{\mathrm{MM}}$, $\Delta U_0^{\mathrm{reac}}$, and $\Delta \overline{U}_{rs}^{\mathrm{MM(sol)}}$ are the differences in the local potential energies obtained in the FF, the intra-molecule potential energy change calculated by gaussian09 at the B3LYP/6-311G(3df,3dp) level, and the intra-molecule potential energy change from the FF calculation, respectively. Note that both $\Delta U_{rs}^{\mathrm{MM}}$ and $\Delta U_0^{\mathrm{reac}}$ contain intra-molecule energy change, and $\Delta \overline{U}_{rs}^{\mathrm{MM(sol)}}$ is a correction term for the double counting of intra-molecule energy change. This treatment for ΔU_{rs} is different from that of a previous study on EC/PC. [37] The values of $\Delta U_0^{\mathrm{reac}}$ and $\Delta \overline{U}_{rs}^{\mathrm{MM(sol)}}$ for each elementary reaction are summarized in Table 3.1.

An example of the three-dimensional supercell used as a model for the anode-electrolyte interface in this study is shown in Figure 3.3. This supercell had a size of 30.0 nm × 3.70 nm × 3.41 nm. The dimensions of the carbon anode, electrolyte, and vacuum ranged from 0 to 2.583 nm, 2.583 to ~17 nm, and ~17 to 30.0 nm, respectively. We prepared the

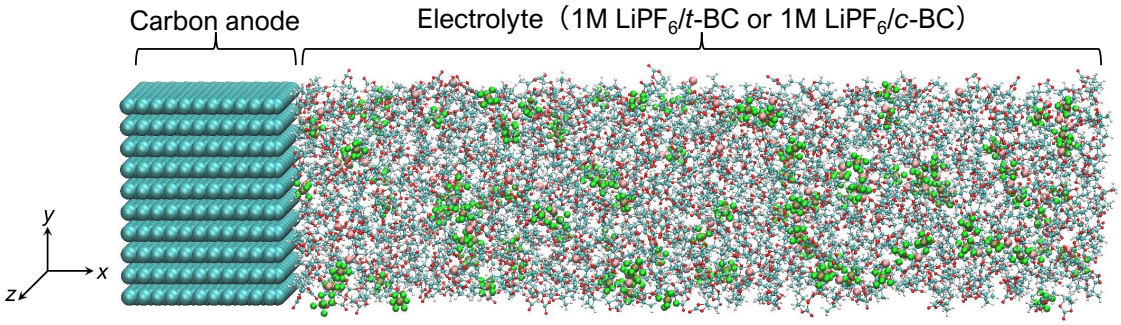

Figure 3.3: Model system for simulation of SEI film formation.

Table 3.2: Number of components of each 1.0 mol L^{-1} $LiPF_6$ electrolyte in the *t*-BC and *c*-BC supercells. These compositions were obtained by *NPT*-MD (1 bar, 298 K)

	t-BC based electrolyte		*c*-BC based electrolyte	
Solvent	*t*-BC (*R*-body)	500	*c*-BC	1000
	t-BC (*S*-body)	500		
Li salt	Li^+	110	Li^+	107
	PF_6^-	110	PF_6^-	107

1.0 mol L^{-1} $LiPF_6$ electrolyte by setting the number of molecules as shown in Table 3.2. To confirm the statistical reproducibility, we also executed a set of RM simulations from 10 independent initial configurations, and we evaluated standard error of these 10 results using a two-sided 95% confidence interval for each system.

3.2.2 Computational details

The MD simulations in this study were executed using the SANDER module in the Amber9 [60] or Amber16 [61] packages. We used the generalized AMBER force field (GAFF) for all chemical species except for PF_6^-; [62] further, we obtained the FF for PF_6^- from a previous study. [63] We obtained atomic point charges using the RESP method, [64] by performing quantum chemical calculations at the B3LYP/6-311G(3df,3pd) level. In line with previous studies, we scaled the point charges of electrolyte solvents by 0.8 to

Table 3.3: Calculated and experimental diffusion constants of each solvent [10^{-10} m^2 s^{-1}]. 1 ns *NVT*-MD (313 K for EC and 298 K for PC and *t*/*c*-BC) simulations were executed.

	EC	PC	*t*-BC	*c*-BC
Calculated	7.31	4.18	3.12	0.95
Experiment	8.0[a]	4.9[b]	-	-

[a] at 313 K, from reference [67]
[b] at 298 K, from reference [68]

reproduce the experimental dipole moments for *t*/*c*-BC, EC, and PC. [14, 37] We set the time step to 1 fs using the SHAKE method, [65] which constrains the bond distance between hydrogen atoms and heavy atoms. We set the temperature of the MD simulations to be 298 K, controlled by a Berendsen thermostat. [66] We applied an *NVT* ensemble to all of the MD parts in the RM simulations. In order to confirm the validity of the present MD simulations, we investigated the diffusion constants of each solvent (see Table 3.3). In the EC and PC solvents, the calculated diffusion constants well agreed with experimental ones. Therefore, the calculation accuracy of the MD simulations used in this study must be sufficient.

The supercell (Figure 3.3) contains a vacuum region that is large enough to avoid interactions with neighboring cells along its *x* direction. We applied a repulsive potential at the border between the electrolyte and the vacuum region to prevent the electrolyte from vaporizing. The RM method repeats a cycle consisting of MC and MD processes, which is called the "RM cycle." In the RM simulations, each RM cycle contains at least one short MD run. We therefore executed a 10 ps MD run to search for the candidates of the possible primary reactions. Moreover, in cases where the reduction reaction was selected

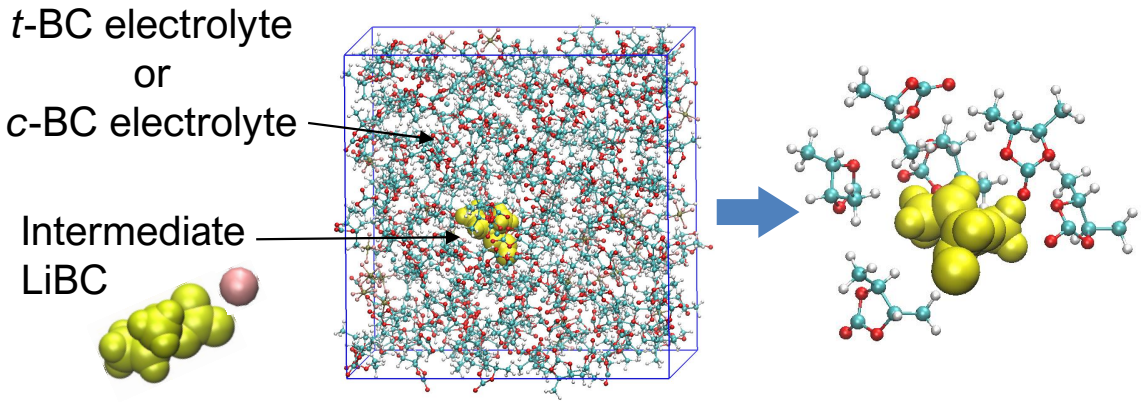

Figure 3.4: Schematic example of supercell for MD and surrounding solvents.

and accepted, we executed another MD run after the reaction. Since the neutrality of the system should be maintained when using the Ewald method, we injected cations (i.e., Li^+) into the cell to keep the charge balance neutral when electrons were consumed by the reduction reaction. Following the acceptance of the reduction reaction and the injection of cations, we executed a further 40 ps run to accelerate the ion diffusion while the reaction products were being fixed. These 40 ps MD runs were divided into two parts; a 20 ps run under the conditions of smaller electrostatic interaction (i.e., a scaling parameter of 0.1), followed by 20 ps run in normal conditions.

We also performed another MD simulation, independent of the above RM protocol, to analyze the solvation properties of the intermediate species in the bulk electrolyte. A schematic for these MD simulations is shown in Figure 3.4, where the supercells for MD consist of single intermediate species in 1 M $LiPF_6$ electrolyte. The composition of each supercell is shown in Table 3.4. We also prepared a set of 30 initial configurations of the supercell for each of the following four systems: "LiBC" in *t*-BC electrolye, "LiBC" in *c*-BC electrolye, "LiEC" in EC electrolyte, and "LiPC" in PC electrolyte. We performed

Table 3.4: The number of each component in each supercell used for MD simulation to analyze the solvation properties of the intermediate species in the bulk electrolyte.

	In *t*-BC electrolyte	In *c*-BC electrolyte	In EC electrolyte	In PC electrolyte
Number of solvents	250	250	250	250
Number of $Li^+ + PF_6^-$	28	27	18	23
Intermediate	LiBC	LiBC	LiEC	LiPC

each of these MD simulations for 10 ns under a *NPT* (1 bar, 298 K) ensemble as a product run, after a series of equilibration runs. All the other settings for these MD simulations were identical to the MD runs in the RM simulation. Using these trajectories, we calculated the number of solvents coordinating to the intermediate and interaction energies between the coordinated solvents and intermediates, every 1 fs. We defined coordinated solvents as solvents that make contact with the intermediate in van der Waals radii. The interaction energy, E_{int} is calculated as follows:

$$E_{\text{int}} = E_{\text{tot}} - (E_{\text{slv}} + E_{\text{im}}) , \tag{3.2}$$

where E_{tot}, E_{slv}, and E_{im} are the potential energies of the cluster consisting of intermediate and coordinated solvents, the coordinated solvents, and the intermediate, respectively.

3.3 Results and discussion

3.3.1 Unstable SEI Film Formation in the *c*-BC Electrolyte

Densities of the SEI films. SEI films were formed during RM simulation in both the *t*-BC and *c*-BC-based electrolytes, as shown in Figure 3.5. We further analyzed the mass

density distributions of the SEI films along with their thicknesses for quantitative and statistical comparison (Figure 3.6). Overall, the density of each component was negligible in regions exceeding 3 nm from the electrode surfaces (Figure 3.6a-b), indicating similar SEI thicknesses for the *t*- and *c*-BC electrolytes. The local distributions of dominant components were also similar for the two films: the gaseous C_4H_8 (from Reaction 2, black) is in the vicinity of the electrode surface (peak at 0.3 nm), and the other inorganic salts (Li_2CO_3 from Reaction 2, red) and organic salts ($Li_2(BC)_2$ from Reaction 3), with a peak position at a distance of $\sim$ 1 nm. We note that in both electrolytes, Reaction 4 scarcely occurred, as only a few PF_3 and LiF were observed during the simulations. This might be due the repulsive interaction between the negatively charged anode surfaces and the anions, which prevents the reductive decomposition of anions at the interface. [37]

The quantitative difference in the two SEI films was exclusively found in the density of $Li_2(BC)_2$ i.e., the dimerized products of Reaction 3, as shown in Figure 3.6c. On one hand, the SEI film formed in *c*-BC electrolyte had 12 % fewer $Li_2(BC)_2$ compounds than that in the *t*-BC electrolyte (2.2 nm^{-3} for *c*-BC versus 2.5 nm^{-3} for *t*-BC, as shown in Table 3.5), originating from the lower mass density distribution of $Li_2(BC)_2$ at x = 1-2.5 nm (Figure 3.6c). On the other hand, the distributions of other products were almost identical in the *t*- and *c*-BC electrolytes. Therefore, the density of $Li_2(BC)_2$ presumably affects the stability of the SEI films. We expect that a larger difference in SEI film density will be observed if we apply a longer timescale to the MD simulation in one RM cycle. Analogous with the fact that dimerized products have been proposed as the primary component of SEI films

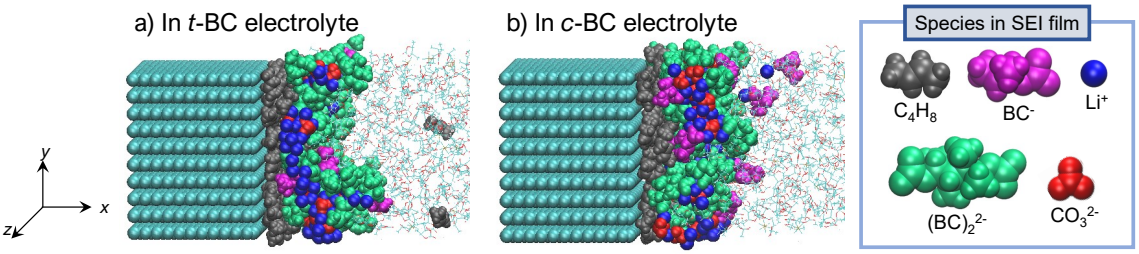

Figure 3.5: Computational SEI films formed in a) *t*-BC electrolyte and b) *c*-BC electrolyte.

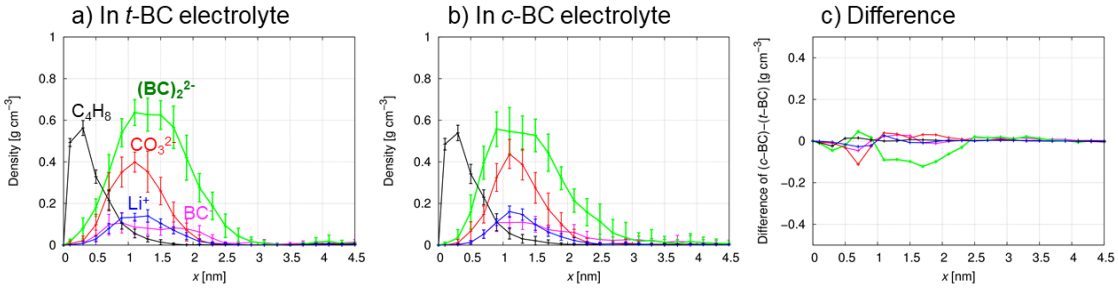

Figure 3.6: Mass density distributions of the reaction products as a function of distance, x, from the electrode surface in the final equilibrium states of RM simulations, for a) the *t*-BC electrolyte, b) the *c*-BC electrolyte, and c) the difference between the two. The average values of 10 RM simulations are used in each panel, and standard errors are estimated to a two-sided 95% confidence interval.

formed in EC-based electrolyte, [52] the decrease in the dimerized product $Li_2(BC)_2$ could be key for explaining the distinct electrochemical behavior observed in *t*-BC (reversible) and *c*-BC (irreversible) films.

In previous studies, the different Li^+ intercalation behavior observed in the *cis-trans*

Table 3.5: Number density of the reaction products in the final states of RM simulations for the *t*-BC and *c*-BC electrolytes

Type	Formula	In *t*-BC electrolyte	In *c*-BC electrolyte
Organic salt	LiBC	0.95 ± 0.1	1.0 ± 0.2
	$Li_2(BC)_2$	2.5 ± 0.2	2.2 ± 0.2
Inorganic salt	Li_2CO_3	4.0 ± 0.3	4.0 ± 0.4
Gas	C_4H_8	4.0 ± 0.3	4.0 ± 0.4

isomers of cyclic carbonate has been attributed to the steric hindrance of solvated Li^+, which occurs in graphite during co-intercalation, [55] because their ring-opening reduction products are identical. However, our results show for the first time that the *cis-trans* isomers cause a distinct difference in the nature of the SEI film, even without the consideration of the co-intercalation process. This difference in the SEI film may directly dominate whether or not reversible Li^+ intercalation occurs; the dense and stable SEI film in *t*-BC can prevent solvent co-intercalation, while the unstable SEI film in *c*-BC cannot.

SEI film formation process. To unveil the differences in the $Li_2(BC)_2$ formation process, the variations of the number densities of the main SEI components ("LiBC", "$Li_2(BC)_2$", and "Li_2CO_3 + C_4H_8") at each RM cycle are summarized in Figure 3.7. The difference in the number densities of $Li_2(BC)_2$ in the two electrolytes increased gradually during the RM cycle; its accumulation lead to a lower number density of $Li_2(BC)_2$ in the c-BC electrolyte. For further investigation, we analyzed the LiBC-LiBC collision frequency. As the dimerized reaction occurred through contact between two LiBC compounds, LiBC-LiBC collision frequency should be one of the indicators for the probability of Reaction 3 occurring (see Figure 3.2). Note that in the RM simulations, we counted each LiBC-LiBC pair as a candidate for Reaction 3 if the distance between two radical carbons was shorter than sum of van der Waals radii of a carbon atom, i.e., 0.3816 nm. We defined the collision frequency as the event number of formations of such candidate LiBC pairs, which are shown in Figure 3.8 as a function of the RM cycles. At around 200-400 cycles, the collision frequency in the *c*-BC electrolyte was lower than that in the *t*-BC electrolyte.

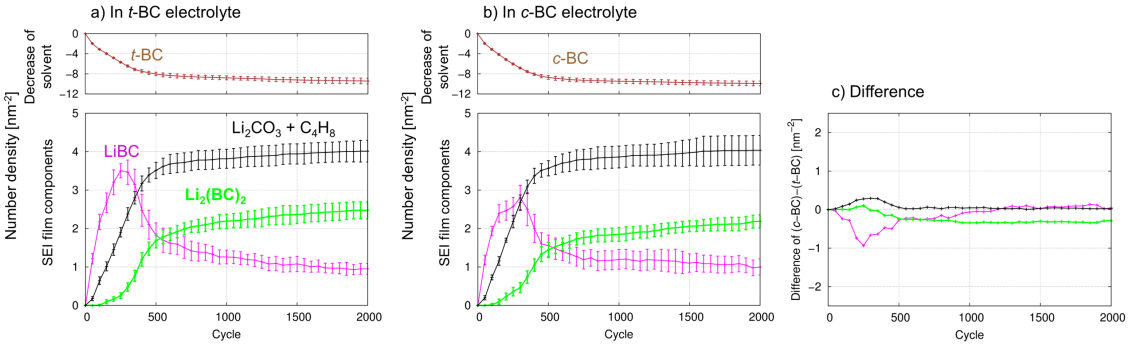

Figure 3.7: Variations in the surface number densities of the solvent molecules and reaction products during the SEI film formation processes, following RM cycles in the (a) *t*-BC-based, (b) *c*-BC-based electrolytes, and (c) the difference between the two. The average values of 10 RM simulations were used, and standard errors were estimated to a two-sided 95% confidence interval.

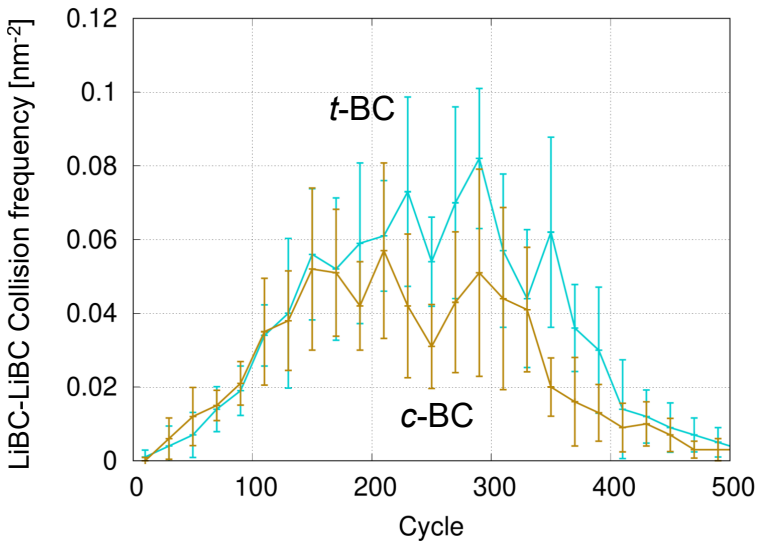

Figure 3.8: Variations in LiBC-LiBC collision frequency during RM cycles in *t*-BC-based and *c*-BC-based electrolytes.

This is consistent with the smaller number density of $Li_2(BC)_2$ in the *c*-BC electrolyte, as shown in Figure 3.7.

Additionally, the existence of a competitive reaction can also decrease the occurrence of dimerizing reactions. LiBC is the intermediate that is consumed, not only by the dimerizing reaction (Reaction 3 in Figure 3.2), but also by the competing two-electron

Table 3.6: Ratio of each reaction product from LiBC [%]

	Li_2CO_3 + C_4H_8 by Reaction 2	$Li_2(BC)_2$ by Reaction 3	Unreacted
In *t*-BC electrolyte	40.5 ± 2.5	49.8 ± 2.6	9.7 ± 1.6
In *c*-BC electrolyte	42.8 ± 2.7	46.5 ± 3.0	10.8 ± 2.0

reduction reaction (Reaction 2 in Figure 3.2). Table 3.6 shows the production ratio of each reaction from LiBC. Evidently, the consumption ratio of the dimerizing reaction was large in the *t*-BC electrolyte than for *c*-BC.

3.3.2 Effect of strong solvation on the stability of an SEI film

Comparison of t-BC and c-BC as solvents. Based on the aforementioned analysis of the SEI film formation process, we determined that less dimerization of LiBC occurred in the *c*-BC electrolyte, making the SEI film less dense and less stable than that formed in the *t*-BC electrolyte. To clarify the origin of this difference, we investigated these molecules as "solvents," because single molecules of *t*-BC and *c*-BC themselves do not shows any peculiar chemical differences. We focused on the solvation of the intermediate LiBC, because this directly influences the collision probability of two LiBC units, forming $Li_2(BC)_2$ as a stable SEI film component. As summarized in Table 3.7, both solvent coordination and interaction energy with LiBC were much larger in the *c*-BC electrolyte than in the *t*-BC electrolyte. As a consequence, the diffusion constant of LiBC is significantly smaller in the *c*-BC electrolyte than in the *t*-BC electrolyte.

Effect of solvation on SEI film formation. We now discuss why the unstable SEI film

Table 3.7: Comparison of the diffusion constants of LiBC and its related solvation properties.

	In *t*-BC electrolyte	In *c*-BC electrolyte
Diffusion constant of LiBC [$\times 10^{-11} m^2\ s^{-1}$]	2.6 ± 0.6	0.6 ± 0.1
Coordination number of solvents	5.63 ± 0.18	6.57 ± 0.16
Solvents-LiBC interaction energy (/a molecule) [kcal mol^{-1}]	−22.5 ± 2.8 (-4.0)	−36.4 ± 3.3 (-4.9)

formation is initiated by strong solvation. Most intuitively, the strong solvation can hinder the dimerization reaction (Reaction 3) because solvation shells disturb direct contact between the two LiBC compounds to form the $Li_2(BC)_2$-based stable SEI film. Kinetically, slower diffusion of LiBC largely diminishes the collision frequency of LiBC, thereby promoting the competitive two-electron reduction reaction (Reaction 2 in Figure 3.2), which making the SEI film unstable.

Furthermore, the competitive reaction can be accelerated at the electrode surface, because the important intermediate LiBC is originally formed by the one-electron reduction reaction of *t*-BC or *c*-BC at the anode surface. If the migration of the LiBC product is slow, this intermediate near the anode surface stays for a longer duration, and therefore undergoes further reduction to form Li_2CO_3 and C_4H_8. Indeed, the collision frequency of LiBC and the anode surface is higher in the *c*-BC electrolyte than in the *t*-BC electrolyte, as shown in Figure 3.9. It should be noted that the steric hindrance of *c*-BC should also affect the SEI film formation. In fact, in our previous report on EC/PC, we clarified that

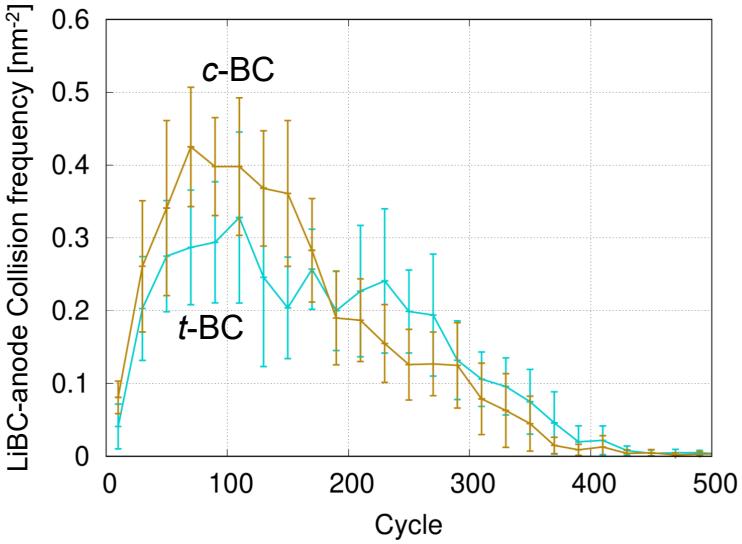

Figure 3.9: Changes in the LiBC-anode surface collision frequency at each cycle in *t*-BC-based and *c*-BC-based electrolytes during the RM simulations. In the RM simulations, LiBC was determined as a candidate for Reaction 2 if the distance between the radical carbon in LiBC and a carbon atom in the anode surface was smaller than the sum of the van der Waals radii of carbon atoms, i.e., 0.3816 nm.

the steric hindrance of the methyl group in PC prevents the aggregation of their reduction products so as to make the SEI unstable. [6] Therefore, the steric hindrance of *c*-BC should decrease the collision frequency between two LiBCs, as shown in Figure 3.8. Overall, the ratio of $Li_2(BC)_2$ decreased in the *c*-BC electrolyte.

In summary, strong solvation could have negative impacts on the growth of a stable SEI film, and is the origin of the continuous solvent reduction/co-intercalation observed in *c*-BC.

3.3.3 Relationship between the "mysteries" in EC/PC and in *t*-BC/*c*-BC

Two pairs of solvents, i.e., EC/PC and *t*-BC/*c*-BC, both consist of good/bad solvents for LIB electrolyte. The "good" solvents, namely EC and *t*-BC, enable reversible Li^+ intercalation

into the graphite anode, whereas the "bad" solvents, PC and *c*-BC are continuously decomposed, causing the exfoliation of graphite instead of Li^+ intercalation. In this regard, our theoretical work demonstrates that dense and stable SEI films can be formed in EC and *t*-BC (good solvents), while sparse and unstable films are formed in PC and *c*-BC (bad solvents). That is, the reversibility of Li^+ intercalation is commonly linked to the stability of the SEI film. [37]

To universalize the solvation effect on destabilization of the SEI film in all those solvents, we next discuss the stability of the SEI film in EC/PC electrolytes, from the viewpoint of their solvation strengths. Table 3.8 shows the calculated diffusion constants of the intermediates (LiEC/LiPC in the EC/PC electrolyte), and their related solvation properties. As for the *c*-BC electrolyte, the PC electrolyte exhibits a lower diffusion constant for its intermediate than the EC electrolyte. However, the strength of solvation to intermediate (LiEC/LiPC) is almost similar in EC/PC pair. Moreover, the diffusion constants of LiPC is comparable to that of LiBC in *t*-BC electrolyte. These results indicate that it is difficult to explain the difference between EC/PC electrolytes based on the solvation to intermediate as with *t*-BC/*c*-BC. In fact, it was experimentally reported that components of SEI film formed in PC electrolyte have higher solubility than that in EC electrolyte. [69] Furthermore, the previous RM simulation also revealed that ratio of dissolved components during the SEI film formation is significantly higher in PC electrolyte than that of EC electrolyte due to the steric hindrance of methyl group of PC. [37] It should be noted that there is no difference in the solubility of SEI film

Table 3.8: Comparison of the diffusion constant of LiEC/LiPC and its related solvation properties.

	In EC electrolyte	In PC electrolyte
Diffusion constant of LiEC/LiPC [$\times 10^{-11} m^2\ s^{-1}$]	5.0 ± 1.5	2.5 ± 0.6
Coordination number of solvents	6.29 ± 0.21	6.10 ± 0.17
Solvents-LiEC/LiPC interaction energy (/a molecule) [kcal mol^{-1}]	−20.8 ± 2.0 (-3.3)	−20.4 ± 2.9 (-3.3)

Table 3.9: Ratio of dissolved components during SEI film formation [%]. In the analyses, the products which exist outside of SEI film (i.e., 3 nm) is regarded as "dissolved components."

Type		In *t*-BC electrolyte	In *c*-BC electrolyte
Organic salt	LiBC	15.4 ± 9.2	15.5 ± 10.9
	$Li_2(BC)_2$	2.7 ± 2.8	3.3 ± 7.0
Inorganic salt	Li_2CO_3	0.2 ± 0.4	0.9 ± 1.9
Gas	C_4H_8	3.1 ± 1.4	2.1 ± 1.4

components in the *t*-BC/*c*-BC electrolytes (see Table 3.9).

In summary, it is concluded that there are two negative effects on the stability of SEI film in *c*-BC and PC electrolytes, respectively (Table 3.10): (1) Strong solvation to intermediate species hinders the generation of SEI film components in *c*-BC-electrolyte and (2) the dissolution of SEI film components proceeds in PC-electrolyte.

Table 3.10: Summary of Li^+ intercalation behavior in relation to the nature of the SEI film and its solvation.

	In *t*-BC electrolyte	In *c*-BC electrolyte	In EC electrolyte	In PC electrolyte
Li^+ intercalation to graphite anode	Reversible	Irreversible	Reversible	Irreversible
SEI film density	Higher density	Lower density	Higher density	Lower density
SEI film stability (cause)	Stable	Unstable (by formation) inhibition)	Stable	Unstable (by dissolution)

3.4 Conclusion

In this study, we performed RM simulations on the process of SEI film formation to unveil the origin of the different charge-discharge behavior of the graphite anode in *t*-BC and *c*-BC electrolytes. We found that the density of the SEI film is lower in the *c*-BC electrolyte than in the *t*-BC electrolyte because of the smaller number of dimerized organic compounds. The origin of different SEI formation processes can also be a stronger solvation of the intermediate compound, which hinders its dimerization reaction. Our results suggest that the use of solvents that satisfy both the weak solvation and low solubility is essential to stabilize the SEI film toward a better charge-discharge performance.

Chapter 4 First-Principles Study on the Peculiar Water Environment in a Hydrate-Melt Electrolyte

4.1 Introduction

To facilitate the development of high-energy-density and safe LIBs, several approaches have been applied to identify new functional electrolytes over the past few decades. In particular, aqueous electrolytes [70] are a promising group of potential replacements for conventional organic electrolytes [14] with regards to safety and low production costs. However, the low electrochemical stability of water and narrow potential window have hindered the application of aqueous electrolytes to LIBs. A key approach to addressing these obstacles is the concept of super-concentrated Li-salt electrolytes. [71] It has widely been reported that, in organic systems, super-concentrated electrolytes have an extraordinarily high electrochemical stability arising from their unique liquid structures, [72, 73] where most of the Li-salt anions are in direct contact with one or more alkali cations. [72, 73] These aggregated structures have significantly modified electronic states that expose the anion states at the lowest unoccupied molecular orbital (LUMO) and form a highly stable anion-derived SEI, which largely improves the reduction stability of the electrolyte at the

negative electrode. [72]

By applying this strategy to an aqueous system, Suo et al. developed a water-in-salt electrolyte with a wide electrochemical window (3.0 V) by dissolving a high concentration of $LiN(SO_2CF_3)_2$ (LiTFSI). [74] Our research group has independently succeeded in further increasing the salt concentration and minimizing the water content to identify a new class of aqueous electrolyte, the hydrate melt, with a negligible amount of free water molecules. This was realized by utilizing a eutectoid of two lithium salts with organic imide anions, TFSI and $N(SO_2C_2F_5)_2^-$ (BETI), to form the dihydrate melt, $Li(TFSI)_{0.7}(BETI)_{0.3}\cdot 2H_2O$, [75] which provides an extremely wide potential window of ca. 3.8 V. Although Raman spectra and FPMD simulations have shown that most of the water molecules coordinate with Li^+, possible partial aggregation caused by structural fluctuation and its influence on the electronic states are now crucial fundamental issues. Unveiling the accurate microscopic coordination structure of water molecules in the hydrate melt will provide technical clues toward further enhancing the electrochemical stability of aqueous electrolytes.

In this study, we investigated the microscopic structures of the dihydrate melt by using FPMD simulations (without empirical parameters) to quantify the number of hydrogen bonds (H-bonds) in various intermolecular couplings and the size distribution of H_2O clusters. Subsequently, we analyzed the calculated projected density of states (PDOS) to achieve better insights into the enhanced electrochemical stability of the dihydrate melt.

4.2 Method

4.2.1 Computational details

FPMD simulations were conducted with the CPMD code [45,76] to investigate the solution structures of a hydrate-melt electrolyte and bulk water for comparison, because we can obtain not only solution structure but also electronic structure without any parameter modification to each target. [72, 73] Figure 4.1 shows the supercells used for the FPMD simulations. The cubic supercell for the hydrate melt (Figure 4.1a) contains 14 LiTFSI ion pairs, 6 LiBETI ion pairs, and 40 H_2O molecules and a cell edge of 18.74 Å, which was set to reproduce the experimental mass density (1.783 g cm^{-3} at 298 K). [75] For the bulk water system, the supercell contains 200 H_2O molecules, and the cell edge length was set to 18.17 Å (Figure 4.1b), which is fitted to the experimental mass density (0.997 g cm^{-3} at 298 K). [77] For the hydrate-melt electrolyte, four FPMD simulations were executed using different independent initial configurations to improve the statistical accuracy and diminish the dependency of simulation results on their selection (Figure 4.2). Because four independent trajectories finally showed the similar energy values, the dependency on the initial structure should be negligible in the liquid structure analyses. The computational values in the hydrate-melt system were evaluated as averages together with the standard errors by using a two-sided 95% confidence interval. In each DFT-MD simulation with the Nosé thermostat [78], we carried out 9.7 ps (10^5 MD steps) sampling after the equilibration and calculated the statistical values. The simulation temperature was set to 350 K following many previous DFT-MD studies on aqueous

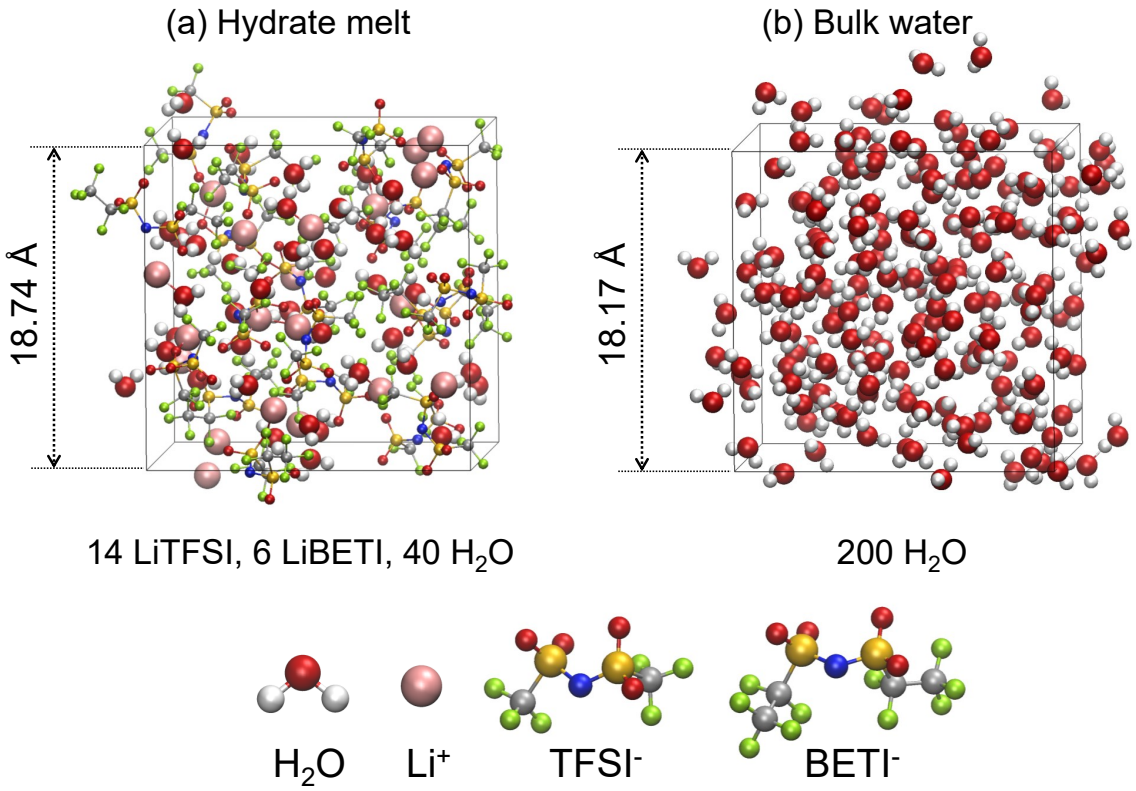

Figure 4.1: Simulation supercells of (a) $Li(TFSI)_{0.7}(BETI)_{0.3}\cdot 2H_2O$ hydrate melt and (b) bulk water. These two configurations are typical snapshots extracted from the CPMD trajectories.

solutions. The time step and fictitious electrlectric mass were set to 4 a.u. ($\cong$ 0.10 fs) and 500 a.u., respectively. The PBE functional with van der Waals correction by Grimme's D2 method was employed for the calculation of exchange-correlation energy. [79] The energy cutoff of the plane wave basis set was set to 90 Ry with Goedecker-Teter-Hutter-type normconserving pseudopotentials for C, H, O, N, S, F, and Li. [80, 81]

4.2.2 Hydrogen and ionic bond analyses

For H-bond analyses, we employed the following geometric criteria: $135° \leq \angle OHY \leq 180°$ and distance O-Y < 3.5 Å for he acceptor Y of H-bonds between Y and H_2O molecules (Figure 4.3). [82, 83] Here, the O atom of H_2O and O, N, and F atoms of the anions (TFSI

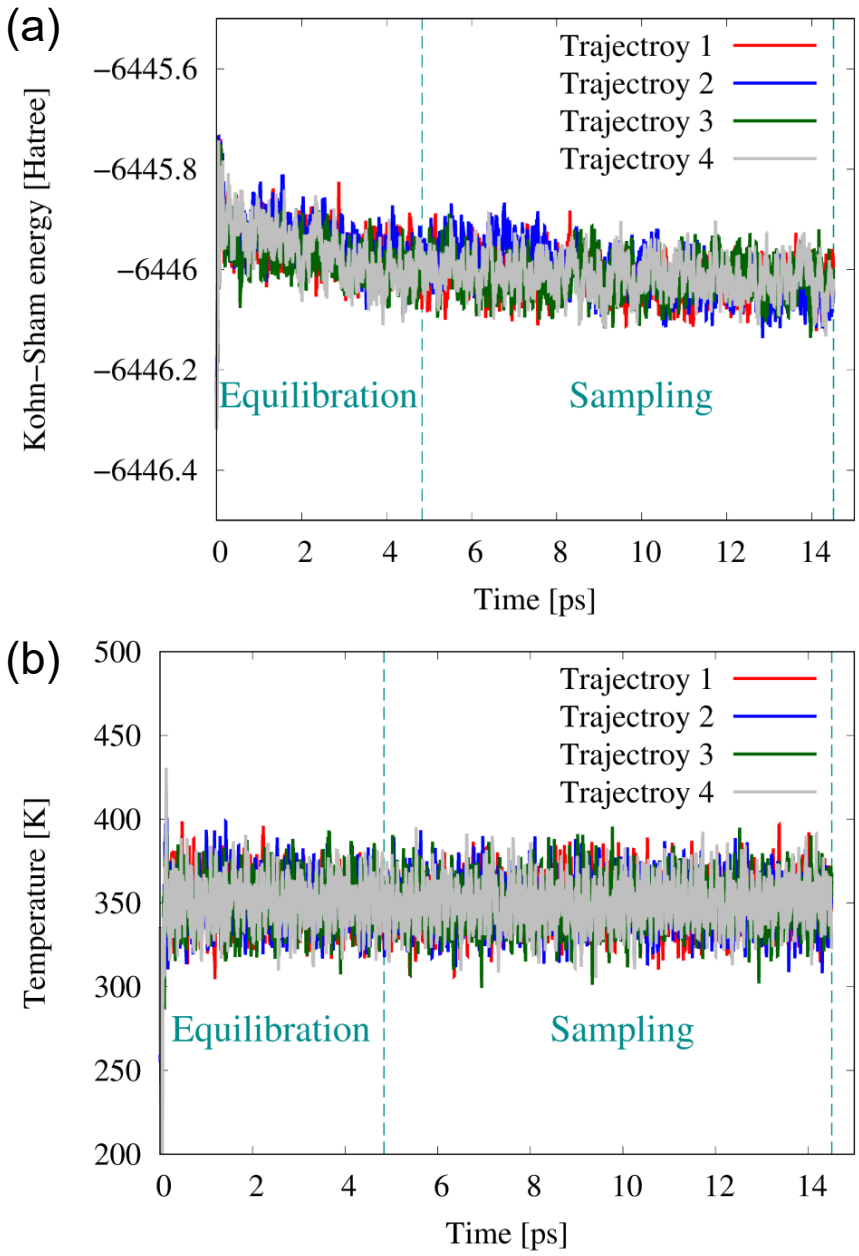

Figure 4.2: (a) Energy and (b) Temperature trajectories of four independent CPMD simulations with Nosé thermostat set to 350 K in this work. After 4.8 ps (5×10^4 MD steps) equilibration, we carried out 9.7 ps (10^5 MD steps) sampling between ca. 4.8-14.5 ps for each run.

and BETI) were employed as acceptors of H-bonds since they have negative charges by population analyses of quantum chemical calculations in the gas phase. Then, we defined a group of H_2O molecules linked by H_2O-H_2O H-bonds as an H_2O cluster in the hydrate

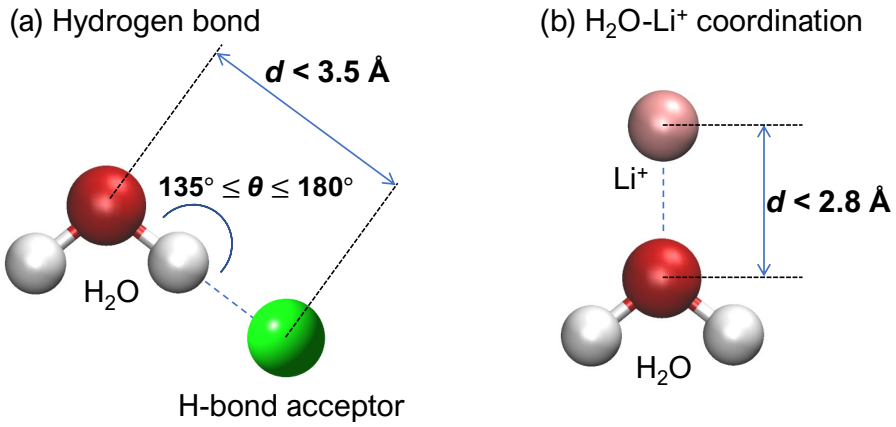

Figure 4.3: Schematic illustrations of geometric criteria.

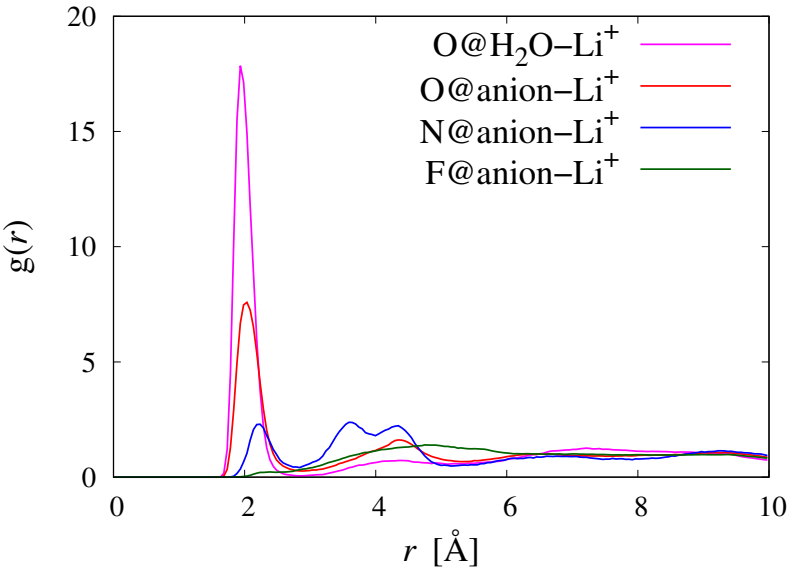

Figure 4.4: RDFs from Li^+ in $Li(TFSI)_{0.7}(BETI)_{0.3}\cdot 2H_2O$ hydrate melt.

melt. For H_2O-Li^+ coordination, the threshold distance of Li^+-O was set to 2.8 Å which corresponds to the first minimum of the radial distribution function (RDF) (Figure 4.4).

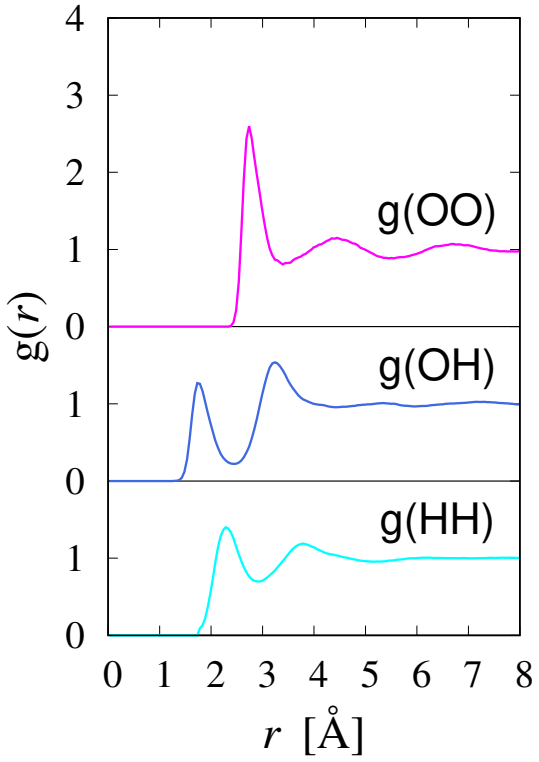

Figure 4.5: RDFs in bulk water. In each panel, g(OO), g(OH), and g(HH) represent RDFs between O atoms, between O atoms and H atoms, and between H atoms, respectively. In g(OH) and g(HH), intramolecular pairs are excluded.

4.3 Results and discussion

4.3.1 Drastic decrease in hydrogen bonds between water molecules

First, we examined the RDFs for pairs of water molecules in bulk water (Figure 4.5). In the bulk water system, three RDFs were found to agree well with experimental neutron diffraction results. [84] In particular, CPMD based on the PBE-D2 functional, which we applied hereafter, successfully reproduced more accurate experimental RDFs of bulk water in comparison with other DFT methods. [85] Thus, the calculation accuracy of the present FPMD simulations is adequate for analyzing the solution structures of aqueous systems.

To elucidate the solution structures of the targeted hydrate melt, we estimated the

numbers of H_2O-H_2O and and H_2O-anion (TFSI or BETI) H-bonds, as well as the coordination number of water molecules to Li^+ cations (denoted as H_2O-Li^+ coordination). Figure 4.6 shows the numbers of H-bonds and H_2O-Li^+coordination per water molecule calculated based on the empirical but reliable geometric criteria (Figure 4.3), in the hydrate melt and bulk water. The average number of H_2O-H_2O H-bonds in the hydrate melt was 0.52, whereas that in bulk water was 3.58, which is in good agreement with experimental data (3.3-3.76). [83, 86] Importantly, the number of H_2O-H_2O H-bonds in the hydrate melt (0.52) is remarkably lower than 2.605 in the water-in-salt with a molar ratio of LiTFSI : H_2O = 1 : 2.7, characterizing the hydrate melt as distinctive from water-in-salt electrolytes. [87] Although the number of H_2O-H_2O H-bonds is significantly decreased in the hydrate melt, isolation into single water molecules is not complete. The much larger numbers of H_2O-anion H-bonds and H_2O-Li^+ coordination per water molecule in the hydrate melt, 1.12 and 0.91, respectively, strongly reflect the preferential coordination of water molecules with Li^+ cations and anions rather than the formation of an H_2O-H_2O H-bond network in the hydrate melt.

4.3.2 Isolated water molecules.

Since the number of H_2O-H_2O H-bonds is significantly decreased in the hydrate melt, most of the water molecules should be isolated from each other. To confirm this, we evaluated the size of H_2O clusters by determining whether each water molecule was connected via H-bond to another water molecule in a snapshot. Figure 4.7a-c shows a typical example configuration of water molecules extracted from a representative FPMD trajectory. In

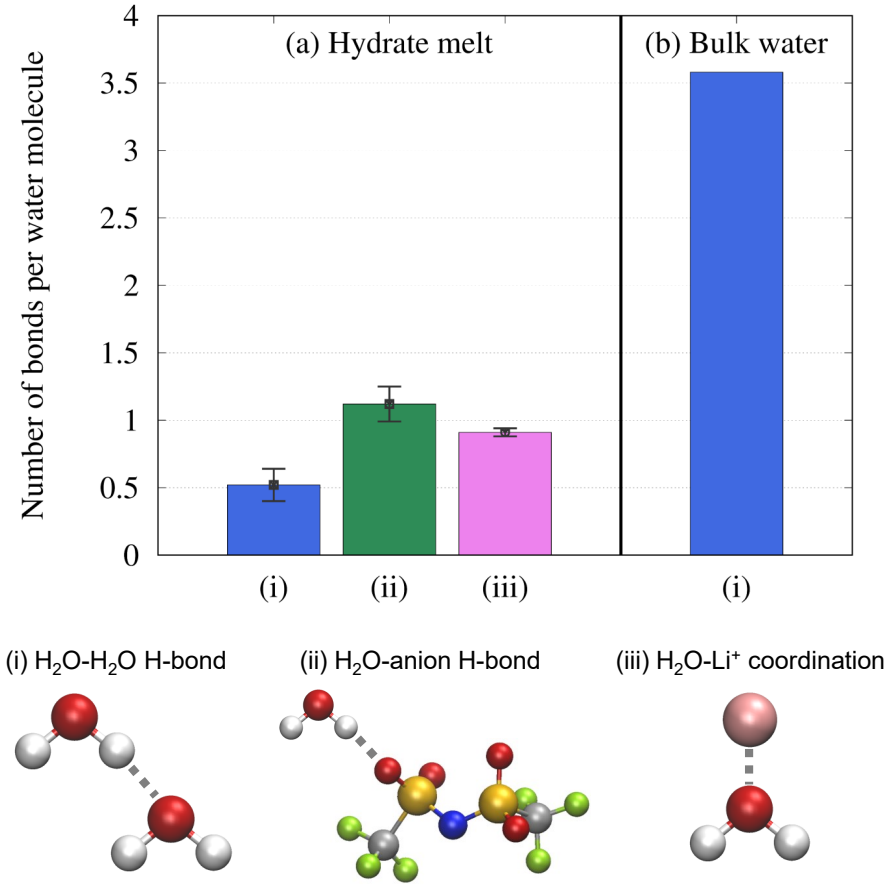

Figure 4.6: Average numbers of H-bonds and H_2O-Li^+ coordination per water molecule in (a) $Li(TFSI)_{0.7}(BETI)_{0.3}\cdot 2H_2O$ hydrate melt and (b) bulk water. Schematic pictures of the H-bonds and H_2O-Li^+ coordination are also shown.

contrast to the bulk water system, where all the water molecules are linked by the H-bond network, the water molecules in the hydrate melt were dispersed without the formation of connected H-bond networks. However, evidence of incomplete isolation was found in the existence of a small amount of water molecules forming isolated clusters, such as dimers and trimers, even at the extremely high salt concentration of the hydrate melt.

Figure 4.7d shows the histogram of H_2O cluster sizes obtained by evaluating their averaged numbers during the FPMD simulations. In the hydrate melt, more than half of the water molecules exist as monomers without any H-bonds to other water molecules.

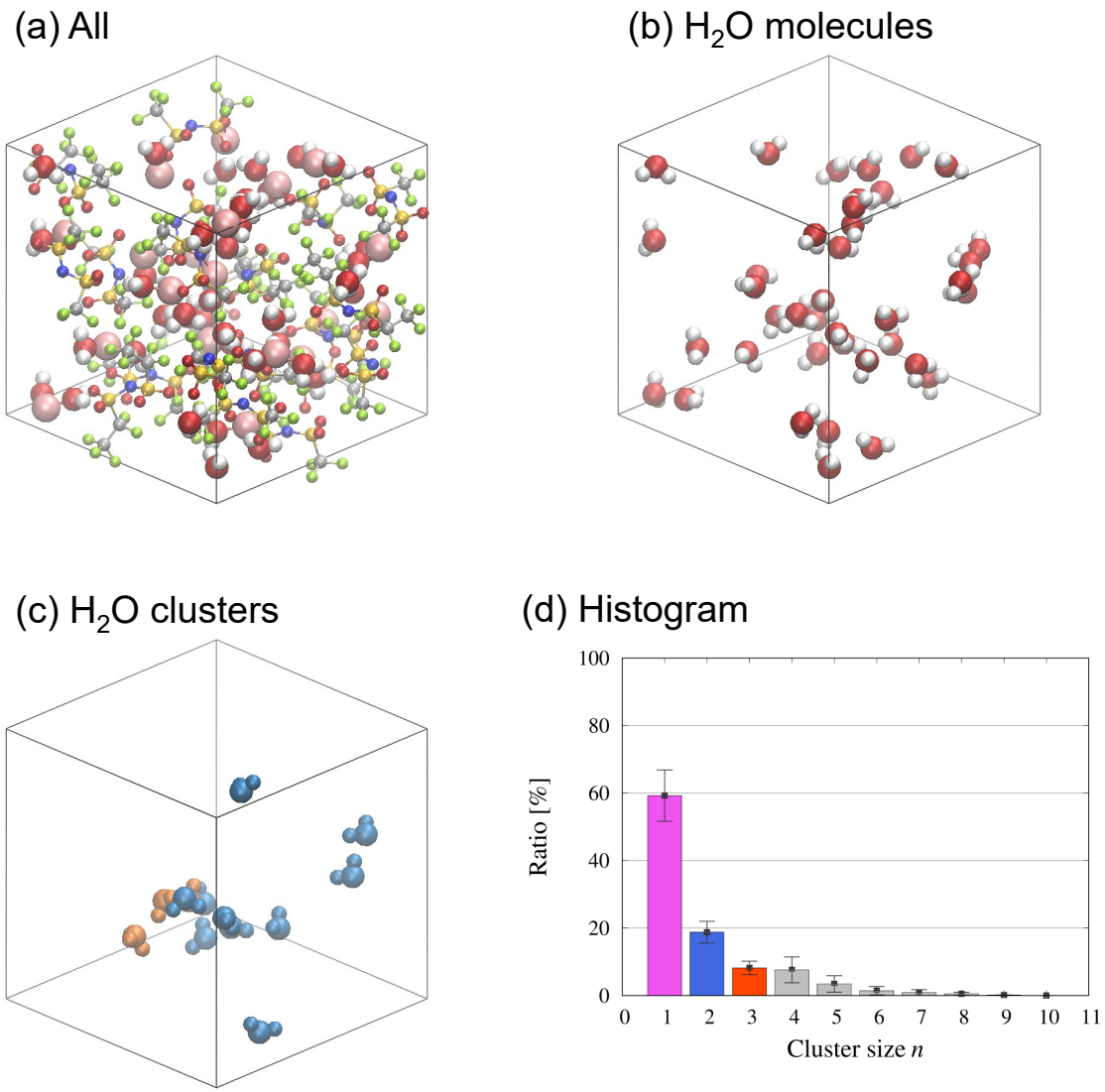

Figure 4.7: (a) Snapshot of (a) $Li(TFSI)_{0.7}(BETI)_{0.3}\cdot 2H_2O$ hydrate melt obtained by FPMD simulations. (b) All H_2O molecules and (c) H_2O dimers (blue) and trimers (orange) extracted from (a). (d) Histogram of H_2O clusters in the hydrate melt based on the geometric definition (Figure 4.3). The histogram represents the averaged cluster sizes over four trajectories.

The remaining H_2O molecules form clusters, with the number of H_2O clusters drastically decreasing as cluster size, n, increases. Especially, the amount of H_2O clusters with $n > 5$ is only 0.6 %, which is negligible considering the whole electrolyte solution. We conclude, therefore, that the water molecules in the hydrate melt exist in isolated states as either monomers or small clusters. In contrast to the hydrate melt, it was suggested

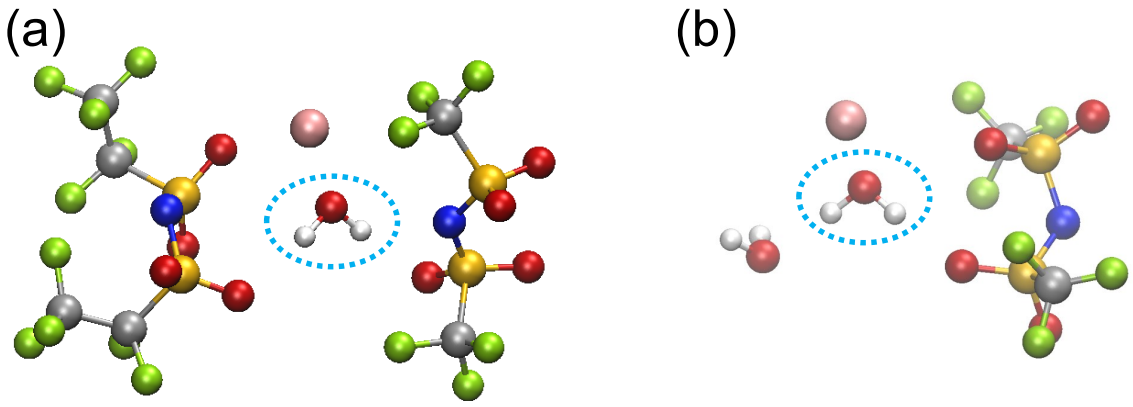

Figure 4.8: Typical snapshots of $Li(TFSI)_{0.7}(BETI)_{0.3}\cdot 2H_2O$ hydrate melt. (a) An H_2O molecule surrounded by only ions (monomer). (b) An H_2O molecule surrounded by ions and another H_2O molecule.

in water-in-salt (with a molar ratio of LiTFSI : H_2O = 1 : 2.7) that the nano-order (1.0-2.0 nm) water-rich region exists by neutron scattering, IR spectroscopy, and classical MD simulation. [87, 88] Such a difference between hydrate melt and water-in-salt seem to be originated from the concentration. Namely, the number of H_2O-H_2O H-bond in the hydrate-melt electrolyte is too small to form the water-rich domain. In order to investigate the local environment of individual H_2O molecules, we analyzed what other molecular species (i.e., H_2O, Li^+, and anions) are coordinated with each water molecule during the FPMD simulations. Here, we categorized the coordination form of individual H_2O molecules into three types, i.e., H_2O molecules surrounded by (i) only ions (Figure 4.8a), (ii) ions and other H_2O molecules (Figure 4.8b), and (iii) only other H_2O molecules. The averaged ratios obtained from four FPMD trajectories are (i) 59.2 %, (ii) 38.2 %, and (iii) 2.6 % in the hydrate melt. Thus, 97.4 % of H_2O molecules are coordinated with ions (cations and/or anions), which is in agreement with our previous experimental study. [75]

Throughout the whole analyses, it is notable that the intramolecular geometries of

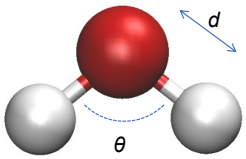

Δd : Difference between two O-H bond distances in a water molecule

	(a) Hydrate melt	(b) Bulk water
θ	104.3 ± 0.05	104.7
d	0.987 ± 0.001	0.999
Δd	0.029 ± 0.002	0.033

Figure 4.9: Comparison of each parameter for a water molecule between (a) $Li(TFSI)_{0.7}(BETI)_{0.3}\cdot 2H_2O$ hydrate melt and (b) bulk water. The values of (a) are averages of four trajectories.

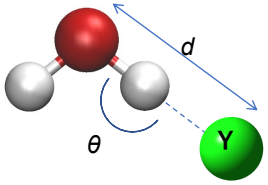

θ

Y	(a)	(b)
$O@H_2O$	154.6 ± 0.61	156.8
O@TFSI	152.0 ± 0.16	-
O@BETI	151.9 ± 0.52	-
N@TFSI	151.1 ± 0.52	-
N@BETI	152.0 ± 0.72	-
F@TFSI	147.3 ± 0.17	-
F@BETI	157.6 ± 0.21	-

d

Y	(a)	(b)
$O@H_2O$	2.92 ± 0.022	2.87
O@TFSI	3.00 ± 0.007	-
O@BETI	3.02 ± 0.016	-
N@TFSI	3.06 ± 0.014	-
N@BETI	3.09 ± 0.019	-
F@TFSI	3.19 ± 0.008	-
F@BETI	3.20 ± 0.005	-

Figure 4.10: Comparison of each parameter for H-bonds between (a) $Li(TFSI)_{0.7}(BETI)_{0.3}\cdot 2H_2O$ hydrate melt and (b) bulk water. The values of (a) are averages of four trajectories.

H_2O, such as O-H distance and H-O-H angle, in the hydrate melt are quite similar to those in bulk water (Figure 4.9). Additionally, there is no significant difference between the intermolecular geometries of H-bonds, such as lengths and angles, in the hydrate melt versus bulk water (Figure 4.10). Therefore, the structural description of the hydrate melt can be simplified as most H_2O-H_2O H-bonds being geometrically replaced with H_2O-anion H-bonds and/or H_2O-Li^+ coordination without any changes in the H-bonding

character itself.

4.3.3 Electronic structures

Figure 4.11 shows the PDOSs of a typical snapshot from equilibrium trajectories in the hydrate melt. The overall trend of the PDOSs was not dependent on the several equilibrium geometries obtained during the FPMD simulations (Figure 4.12). Similar to the characteristic feature reported in super-concentrated organic electrolytes, the LUMO is located on the BETI or TFSI anions. [72, 73] This indicates that the TFSI or BETI anions

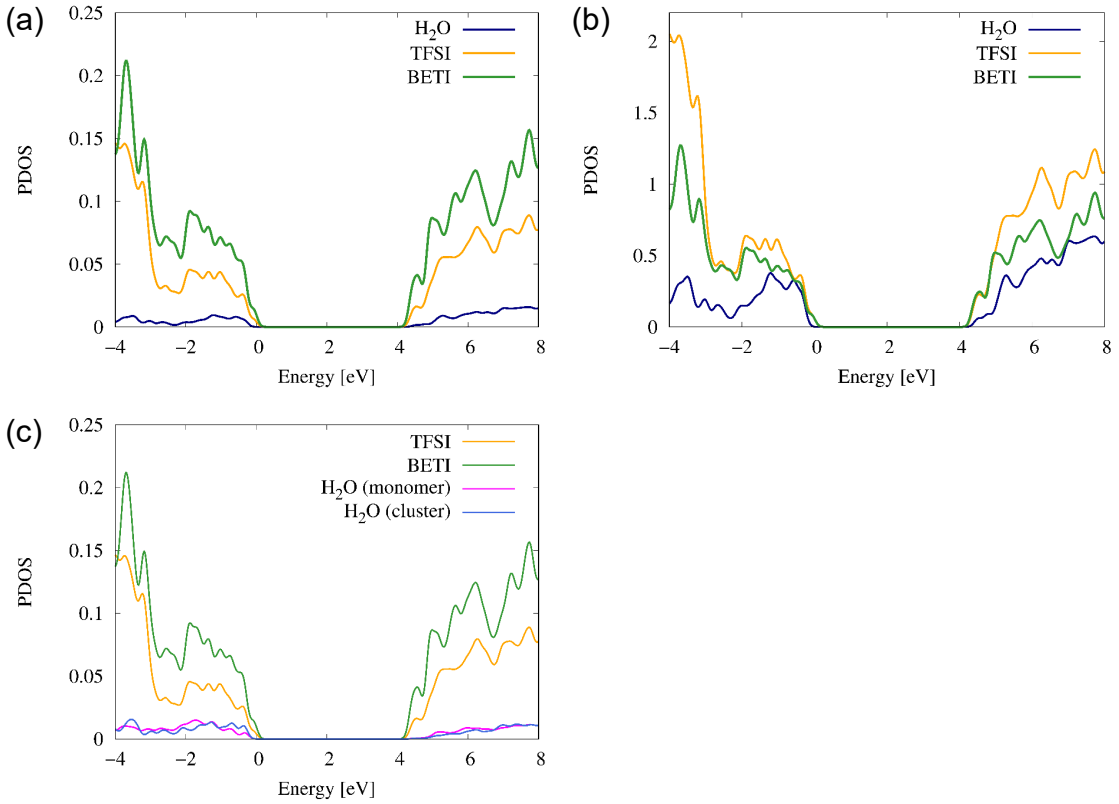

Figure 4.11: PDOSs of a typical snapshot from equilibrium trajectories of $Li(TFSI)_{0.7}(BETI)_{0.3}\cdot 2H_2O$ hydrate melt. These were calculated from the same snapshot. (a) Normalized PDOS (per ion/molecule). (b) Unnormalized PDOS which reflects the number of molecules/ions. (c) H_2O PDOS divided into monomer and cluster (with normalization by the number of molecules/ions).

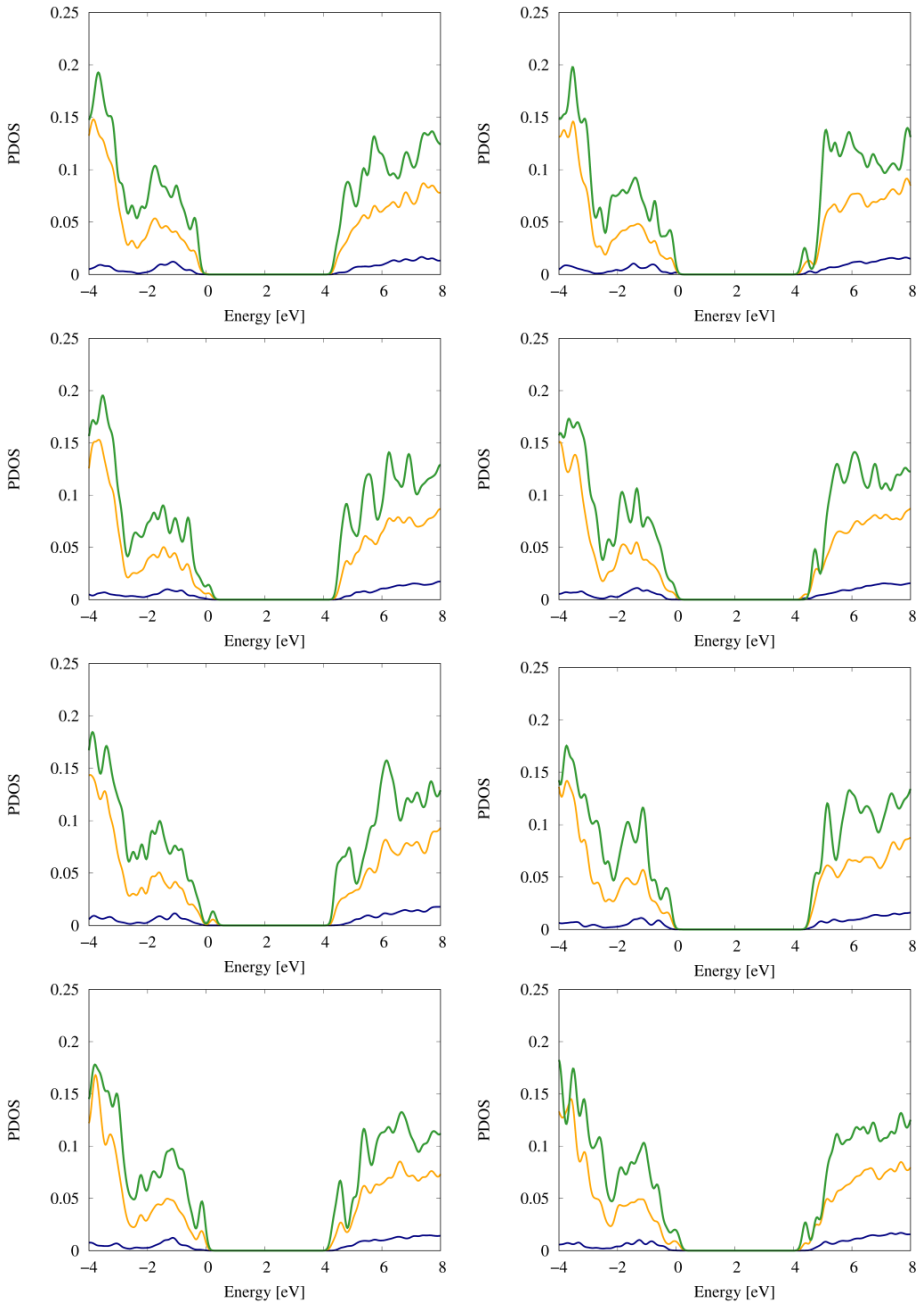

Figure 4.12: Examples of PDOSs in $Li(TFSI)_{0.7}(BETI)_{0.3}\cdot 2H_2O$ hydrate melt. The same as in Figure 4.11, the navy, orange, and green lines correspond to H_2O, $TFSI^-$, and $BETI^-$, respectively. Each PDOS is normalized by the number of molecules/ions.

are predominantly reduced in the hydrate melt, which is consistent with experimental observations of SEI films mainly derived from the reductive decomposition products of anions such as LiF and some S-containing species. [74, 75, 89, 90] Noteworthy, anion-

Table 4.1: Averaged number of Li^+ cations contacting each anion in $Li(TFSI)_{0.7}(BETI)_{0.3}\cdot 2H_2O$ hydrate melt. The values are averages of four trajectories.

	$TFSI^-$	$BETI^-$
Number of contacting Li^+	2.1 ± 0.13	1.9 ± 0.28

decomposition pathways in super-concentrated systems have already been verified either theoretically or experimentally. [28,72,91,92] According to previous theoretical research, [90] the Coulombic energy gain of anions induced by the existence of Li^+-anion ionic bonds should cause the preferential reduction of the anions. Our FPMD simulations of the hydrate melt also show that the TFSI and BETI anions are coordinated with approximately two Li^+ cations (Table 4.1). Thus, the present analysis clearly demonstrates that the formation of such aggregated structures promotes the reduction of the anions by changing their electronic states.

Finally, we examine the PDOSs associated with the isolated or clustered water molecules, which are shown in Figure 4.11c. These demonstrate that the overall shape is almost the same regardless of the presence of intra-cluster H_2O-H_2O H-bonds. This is because most of the water molecules in small clusters are coordinated with ions in the same manner as the water monomers (as shown in Figure 4.13). Namely, the electrostatic interactions with cations/anions, rather than intra-cluster H-bonding with other water molecules, dominates the electronic state of the water molecules in the hydrate melt. However, the electronic structure of water molecules (either as monomers or in small clusters) in the hydrate melt is significantly different from that in bulk water, [93] as characterized by, for example, wider HOMO-LUMO gap, which makes anion as major constituent element of LUMO.

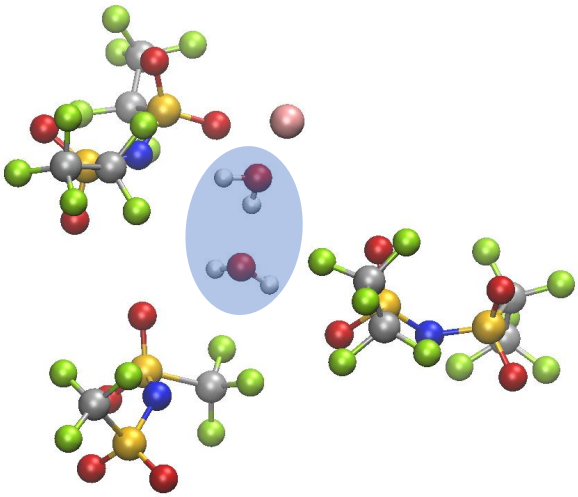

Figure 4.13: Example of surrounding environment of an H_2O-dimer in $Li(TFSI)_{0.7}(BETI)_{0.3}\cdot 2H_2O$ hydrate melt.

Thereby, the predominant reductive decomposition of the anions may occur prior to the reduction of water. It should be noted that the electronic structure might change in the interfacial region on the electrode surface. At the electrode-electrolyte interface, not only the contact frequency to the electrode but also the kinetics of electron transfer should be important. Although it is suggested that the ratio of water molecules increases at the negative electrode interface, [89] the hydrate-melt electrolyte could possibly retain its high electrochemical stability as long as the number of the small clusters ($n < 5$) would increase.

4.4 Conclusion

In summary, by applying FPMD simulations, the detailed solution structure of the hydrate melt $Li(TFSI)_{0.7}(BETI)_{0.3}\cdot 2H_2O$ has now been clarified. As expected, the number of H_2O-H_2O H-bonds is significantly smaller than that in bulk water, and most H_2O molecules

exist as monomers or small H_2O clusters ($n \leq 5$ at a 99.4 % presence) that are coordinated to one or more ions (Li^+ or anions). This unique local environment largely modifies the electronic states of the hydrate melt such that the LUMO of the water molecules is higher in energy than that of the TFSI or BETI anions. This makes reduction of the anions preferential over reduction of the water molecules, leading to the formation of a stable anion-derived SEI film on the negative electrode. Emphasis is given to the small H_2O clusters ($n \leq 5$, ca. 99.4 % presence), which energetically behave similarly to completely isolated H_2O molecules. It is difficult for these clusters to be reduced to generate hydrogen, and thus instead they can contribute to the formation of the anion-derived stable SEI.

Chapter 5 First-Principles Study on the Cationic-Dependent Water Environment in Li/Na/K-Hydrate-Melt Electrolytes

5.1 Introduction

LIBs, which have been used for nearly 30 years, are becoming more important and require greater reform [1] for expanding applications. Most desired application is a large-scale energy charging device which enables the efficient use of renewable energy and long-distance driving of electric vehicles [3]. However, these goals cannot be achieved simply by enlarging the current battery size because the issues on the production cost, safety, and performance are fatal problems to be solved for the practical applications. [4, 5] Aqueous Na and K ion batteries have potential to solve these problems and replace the commercially available LIB. In fact, the aqueous electrolytes are excellent candidates of conventional organic ones in terms of safety and production cost. [70] Furthermore, in contrast to Li, Na and K are widely and abundantly distributed over the earth. If Na and K ion batteries with an aqueous electrolyte is available for practical use, the safe and low-cost secondary battery can be stably supplied. Thus, the development of high performance Na and K based aqueous electrolytes is one of the urgent issues.

Toward the development of high performance aqueous electrolytes, our research group has discovered a series of hydrate-melt electrolytes for Li, Na, and K. [34, 75, 94] These hydrate-melt electrolytes indicate extraordinary electrochemical stability compared to the diluted aqueous solution ($\sim$ 1 mol L^{-1}). Especially, Li-salt based monohydrate melt, $Li(TFSI)_{0.4}(PTFSI)_{0.6}{\cdot}H_2O$ (PTFSI = $N(SO_2CF_3)(SO_2C_2F_5)^-$) has the remarkable wide electrochemical potential window ($\sim$ 5V) [94]. On the other hand, by introducing the third anion, OTf^- ($SO_2CF_3^-$), $Na(OTf)_{0.21}(TFSI)_{0.14}(PTFSI)_{0.65} \cdot 3H_2O$ and $K(OTf)_{0.8}(TFSI)_{0.08}(PTFSI)_{0.12} \cdot 2H_2O$ have been discovered as Na- and K-based hydrate melts, respectively. [34] These Na/K hydrate-melt electrolytes show greater electrochemical stability than the diluted aqueous electrolytes. [73] Although the super concentrating approach seems to be useful for Na and K based aqueous electrolytes, the electrochemical potential window became narrower in the order of Li, Na and K systems [34, 75, 94]. Such experimental tendency suggests that the kind of alkali cation strongly affects the electrochemical stability of the aqueous electrolyte.

In this study, to reveal the origin of the different electrochemical stability of Li, Na, and K based hydrate-melt electrolytes, we performed FPMD simulations. In the analyses, we employed the Li, Na and K based hydrate-melt electrolytes with the lowest water ratio as shown in Table 5.1. [34, 94] First, we investigated the difference of solvation structures between three hydrate melts. Then, we evaluated the size distribution of H_2O clusters by quantifying the hydrogen bonds (H-bonds) between H_2O molecules. Subsequently, we analyzed the projected density of states (PDOS) to clarify the relationships between

Table 5.1: Composition of each hydrate melt investigated in this study

	Composition
Li hydrate melt	$Li(TFSI)_{0.4}(PTFSI)_{0.6}\cdot H_2O$
Na hydrate melt	$Na(OTf)_{0.21}(TFSI)_{0.14}(PTFSI)_{0.65}\cdot 3H_2O$
K hydrate melt	$K(OTf)_{0.8}(TFSI)_{0.08}(PTFSI)_{0.12}\cdot 2H_2O$

solution structure and electrochemical stability.

5.2 Method

The CPMD simulation was conducted to investigate solution structures and electronic states of three hydrate melts shown in Table 5.1. The calculation procedure of the present FPMD simulations is common to that of the previous ones in Li dehydrate melt. [94] The calculation models are shown in Figure 5.1, where the volume of each cubic supercell is determined so as to fit the experimental mass densities, i.e., 1.86, 1.76, and 1.81 g cm^{-1} for Li, Na, and K hydrate melts [34, 94], respectively. To improve the statistical accuracy, four independent CPMD simulations from different initial structures were executed for each hydrate melt. The computational values in three hydrate-melt systems were evaluated as averages of four independent trajectories together with the standard errors by using a two-sided 95 % confidence interval. In each DFT-MD simulation with the Nosé thermostat [78] we carried out 9.7 ps (10^5 MD steps) sampling after the equilibration and calculated the statistical values. For H-bond analyses, we employed the same geometrical criteria as the previous report. [95]

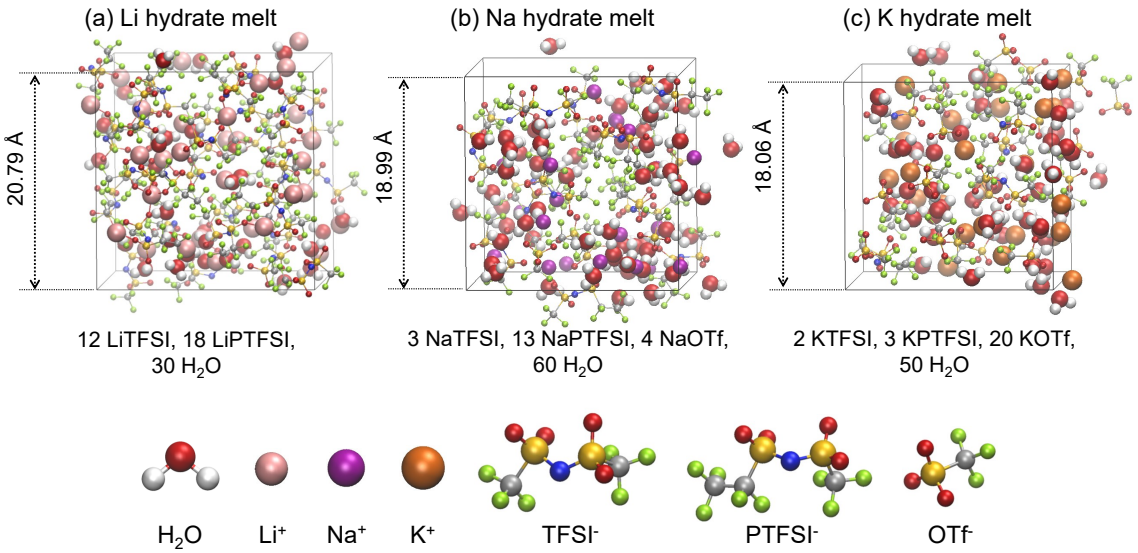

Figure 5.1: Simulation supercells of (a) Li, (b) Na, and (c) K hydrate melt. These three configurations are typical snapshots extracted from the CPMD trajectories.

5.3 Results and discussion

5.3.1 Change in cationic solvation shell in Li/Na/K hydrate melts

First, to investigate the solvation structures around cations in each hydrate melt, we analyzed RDFs (Figure 5.2). In the order of Li, Na, and K, the first peaks of all the distributions shifted to right side along the horizontal axis and became broader. Further, the peak heights of O(H_2O)-cation and O(anion)-cation distributions decreased in the same order. These results clearly show that the first solvation shells of cations become larger along with the weaker coordination of cations to H_2O and anions. Especially, the coordination strength of cation-H_2O became weaker in the order of Li, Na and K systems (see pink curves of Figure 5.2). In Li hydrate melt, the peak height of O(H_2O)-Li^+ distribution was highest (Figure 5.2a). In contrast, in K hydrate melt, the peak height of O(H_2O)-K^+ was similar to that of O(anion)-K^+ (Figure 5.2c). This degree of strength can

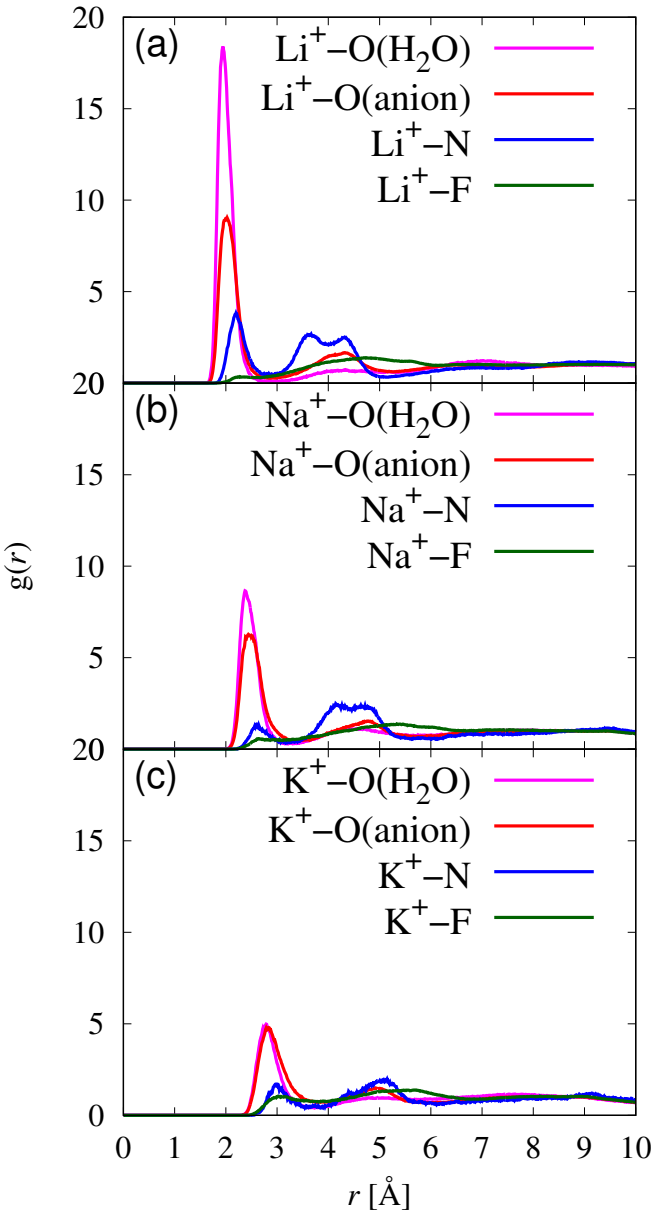

Figure 5.2: Radial distribution functions from alkali cation in (a) Li, (b) Na, and (c) K hydrate melt.

be readily understood as the order of the ionic radius, i.e., Li < Na < K. In fact, the binding energies and equilibrium distance of cation-H_2O dimer became smaller and longer in the order of ionic radius (Figure 5.3).

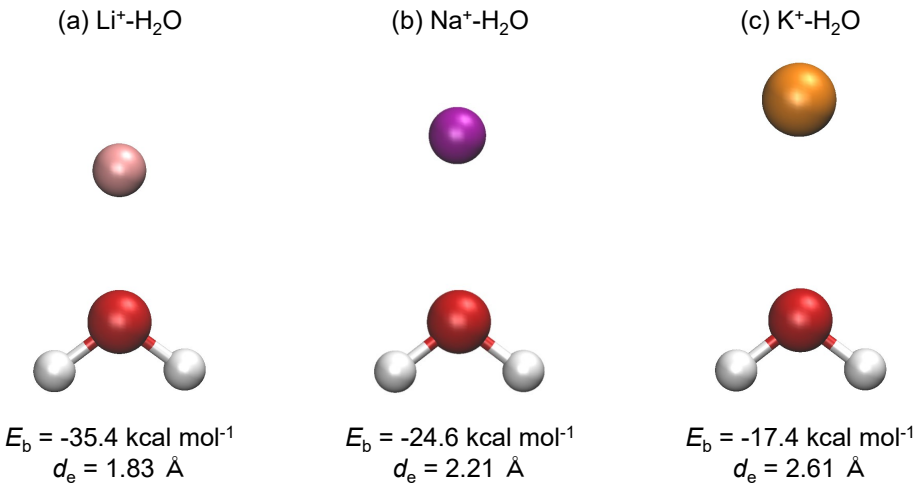

Figure 5.3: Binding energies of cation-H_2O dimer and equilibrium distances between cation and oxygen atom calculated by B3LYP/6-311++g(3df,3pd) in gas phase.

Table 5.2: Averaged number of water cluster size in each system. The values are averages of four trajectories.

	Li hydrate melt	Na hydrate melt	K hydrate melt
Cluster size	1.30 ± 0.13	10.44 ± 3.88	6.19 ± 0.86

5.3.2 Enhancement of H_2O-H_2O aggregation

Next, to investigate the surrounding environment of H_2O molecules in Li, Na, and K hydrate melt, we analyzed the histograms of H_2O cluster (Figure 5.4) and average size of water cluster (Table 5.2).In the analyses, we evaluated the size of H_2O clusters by determining whether each water molecule was connected via H-bond to another water molecule. [95] It is common that all the hydrate melts contain the isolated monomer H_2O molecules in comparison to the bulk water. [74] Especially, in the Li hydrate melt, most H_2O molecules exist as a monomer or small H_2O clusters ($n \leq 5$) (see Figure 5.4a). However, in the Na and K hydrate melt, average sizes of water cluster were larger than that in Li system along with the presence of larger water clusters ($n > 5$) (Figure 5.4b and c).

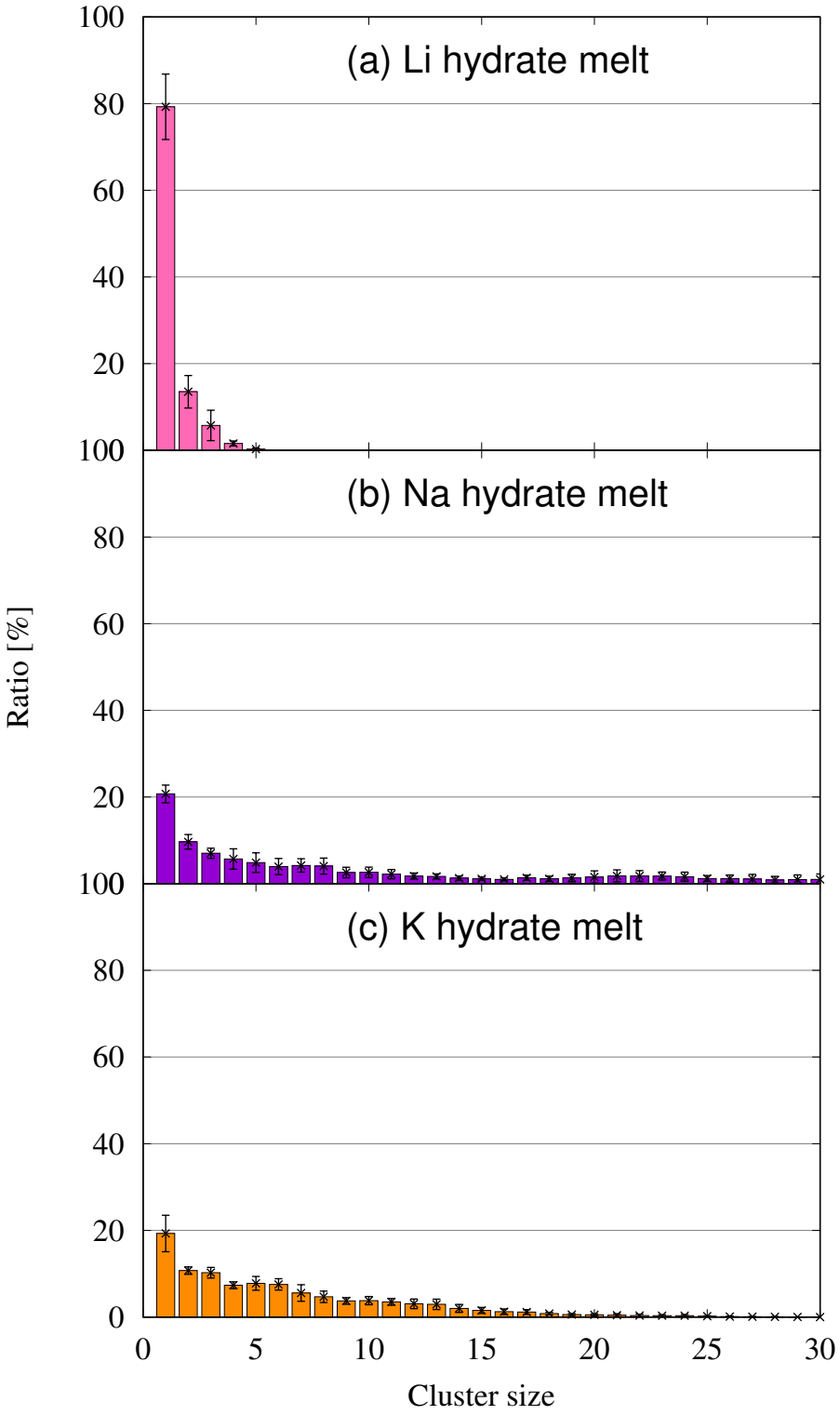

Figure 5.4: Histograms of H_2O cluster in (a) Li, (b) Na, and (c) K hydrate melt.

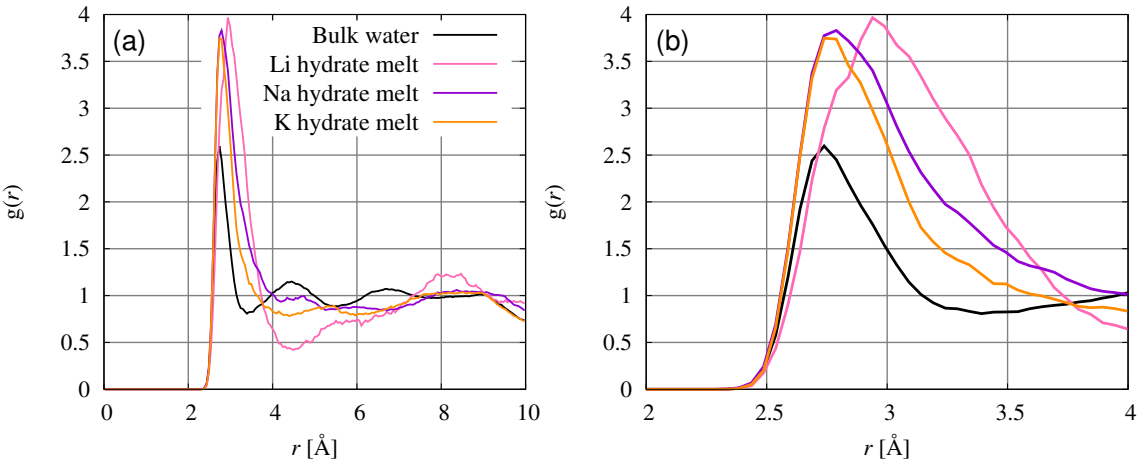

Figure 5.5: RDFs of two O atoms of H_2O molecule. Black, pink, purple, and orange lines represent RDFs in bulk water, Li hydrate melt, Na hydrate melt, and K hydrate melt, respectively. The RDF of bulk water is quoted from previous report [95]. Panel (b) is an enlargement of the panel (a).

Then, Figure 5.5 shows the RDFs between oxygen atoms of H_2O molecules in the three hydrate melts. As a result, the shape of first peaks in the hydrate melt was found to be close to that in the bulk water in the order of Li, Na and K systems. This indicates that the H_2O-H_2O H-bonds in the hydrate melt become stronger in the same order. In fact, comparing between Li and K dehydrate melts which include the same amount of H_2O molecules, the ratio of the monomer H_2O in the K system was 19.3 % (Figure 5.4c), whereas that in the Li system was 59.2 %. [95] Furthermore, the histogram of the Na trihydrate melt (Figure 5 17b) was very similar to that of the K dihydrate melt with a smaller water content (Figure 5.4). Namely, it can be said that the H_2O molecules in the hydrate melt are easily associated in the order of Li, Na and K systems. It is concluded, therefore, that the H-bonds between H_2O molecules in the hydrate melt significantly increase due to the increase in the ionic radius and decrease in the Lewis acidity.

Table 5.3: The average number of cations contacting to an anion in each hydrate melt. 2.8, 3.3, and 3.8 Åare used as threshold distance of coordination to alkali cation of O/N/F atoms of anion in Li, Na and K hydrate melts, respectively.

	Li hydrate melt	Na hydrate melt	K hydrate melt
Number of cations	3.06 ± 0.38	2.77 ± 0.39	3.75 ± 0.78

5.3.3 Electronic structures of water molecules and anions

Finally, we investigated the electronic states of three hydrate melts by analyzing PDOSs. Figure 5.6, Figure 5.7, and Figure 5.8 show the examples of PDOS of Li, Na, and K hydrate melts, respectively. In the Li system, the LUMO of H_2O molecules was located at higher level than that of anions, suggesting that the predominant reductive decomposition of the anions occur prior to the reduction of water. This feature is common in all the snapshots extracted from MD trajectory. Thus, in the Li monohydrate-melt electrolyte, the stable anion-derived SEI film can be formed as with the Li dihydrate-melt electrolyte [75, 95] and super concentrated organic electrolytes. [71–73] However, in Na and K hydrate melts, the LUMO of H_2O was located at the similar or smaller levels than that of anions. Such unstable LUMO of anions in the Na and K systems should prevent the formation of anion-derived SEI, which can suppress the hydrogen evolution reactions on the negative electrode.

The previous theoretical research proposed that the increase in the coordination number of Li^+ cations with anions is associated with the preferential anion reduction in the highly concentrated aqueous electrolyte [90]. However, as shown in Table 5.3, the coordination number of K^+ was higher than that of Li^+ although the LUMO of anions was unstable

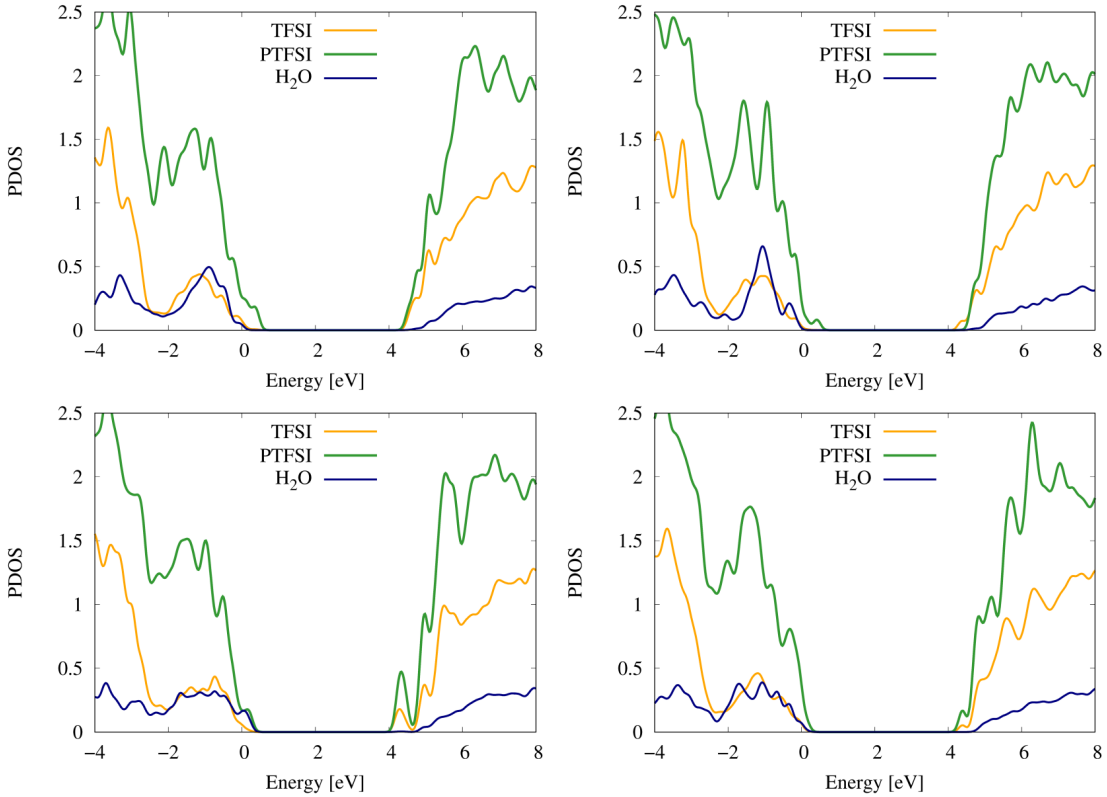

Figure 5.6: Examples of PDOSs in Li hydrate melt. The navy, orange, and green lines correspond to H_2O, $TFSI^-$, and $PTFSI^-$, respectively. Each PDOS is Unnormalized and reflects the number of molecules/ions.

in the K system. On the other hand, the Coulomb interaction between alkali cation and anion becomes weaker in the order of Li, Na, and K as shown in Figure 5.3. Thus, the weaker Coulomb interaction between alkali cation and anion should be dominant to make the LUMO of anions unstable in Na and K systems. Therefore, the increase in the ionic radius of alkali cations should cause the unfavorable electronic states of the hydrate-melt electrolytes.

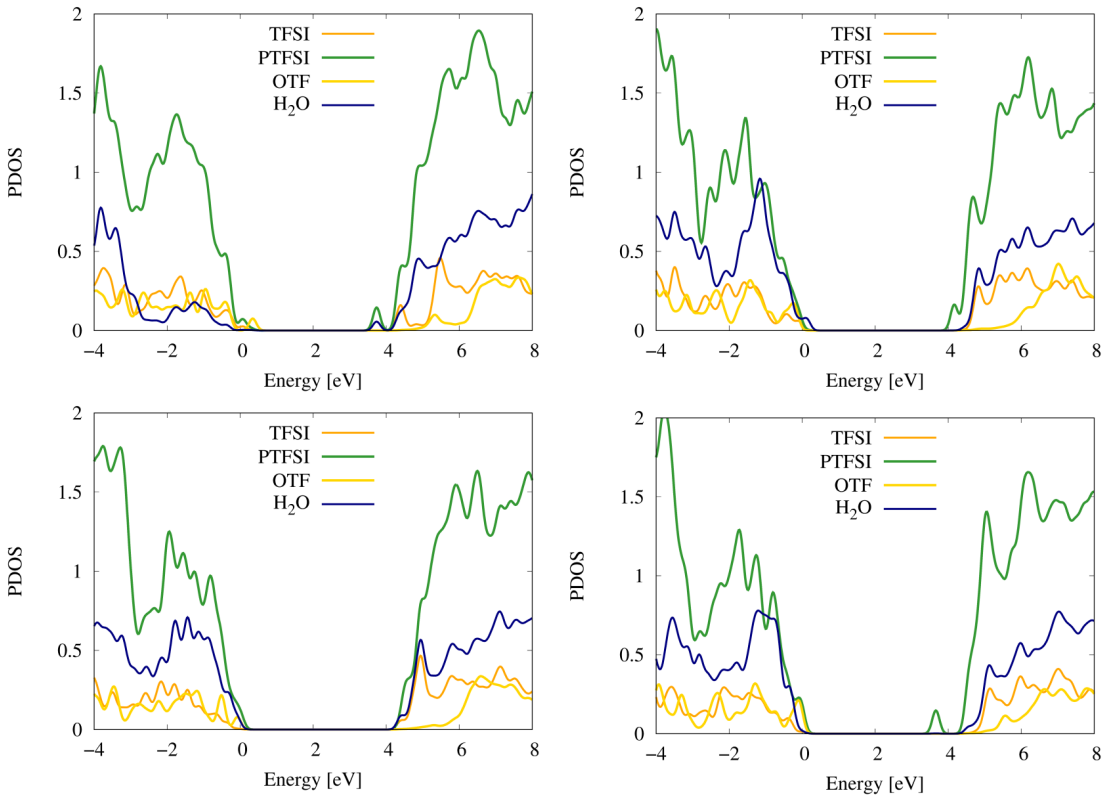

Figure 5.7: Examples of PDOSs in Na hydrate melt. The navy, orange, green, and yellow lines correspond to H_2O, $TFSI^-$, $PTFSI^-$, and OTf^- respectively. Each PDOS is Unnormalized and reflects the number of molecules/ions.

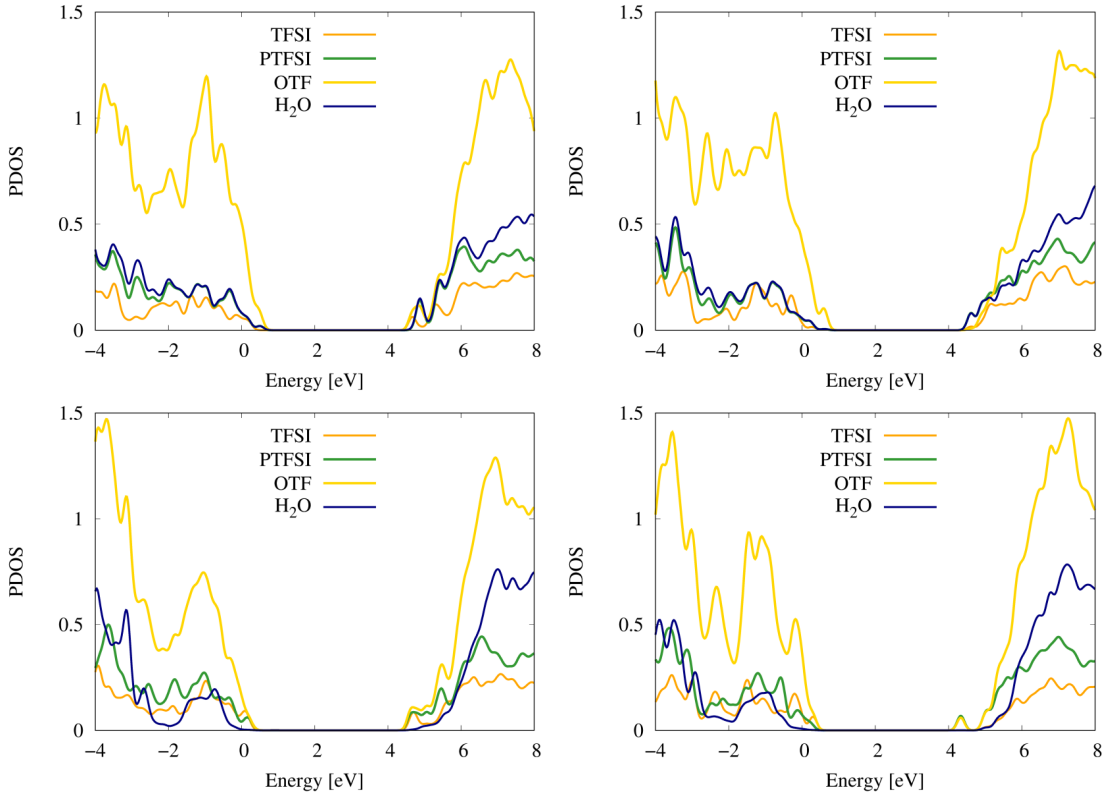

Figure 5.8: Examples of PDOSs in K hydrate melt. The navy, orange, green, and yellow lines correspond to H_2O, $TFSI^-$, $PTFSI^-$, and OTf^- respectively. Each PDOS is Unnormalized and reflects the number of molecules/ions.

5.4 Conclusion

In this study, to reveal the origin of narrower electrochemical window in the order of Li, Na, and K based hydrate-melt electrolytes, their solution structures and electronic states were surveyed by FPMD simulations. The increase in the ionic radius weaken the cation-H_2O coordination in the hydrate melt. As a result, such weaker interaction between cations and H_2O molecules enhances the aggregation of H_2O molecules in the larger alkali cation systems, preventing the isolation of water. Further, the strong association of water and weakened cation-anion Coulomb interaction in the Na and K hydrate melts should prevent the formation of anion-derived SEI film like in Li system. This indicates that the lower Lewis acidity of the alkali cation affects the electrochemical stability of the aqueous electrolyte. Thus, to form the stable SEI film and widen the potential window in Na and K hydrate melt electrolytes, more concentration or the addition of additives that prevent the water aggregation may be effective. For example, the addition of small amount of strong Lewis acid like Al^{3+} may be effective. In fact, the hydration free energy of Al^{3+} (-4525 kJ mol^{-1}) is known to be much larger than that of Na^+ (-365 kJ mol^{-1}) and K^+ (-295 kJ mol^{-1}). [96] Thus, it is expected that the water aggregation might be reduced owing to the strong coordination interaction between Al^{3+} and H_2O. On the other hand, from the aspect of the ionic conductivity, the lower Lewis acidity of Na^+ and K^+ has an advantage in comparison to Li^+. It was reported that the order of ionic conductivity is Li (3.0 mS cm^{-1} in di-hydrate melt) < Na (14.0 mS cm^{-1} in tri-hydrate melt) < K (34.6 mS cm^{-1} in di-hydrate melt). [34, 75] Namely, it is considered that the electrochemical

stability and ionic conductivity are in a trade-off relationship. Thus, the Na and K ion aqueous batteries have a potential to exceed the state-of-the-art LIB in terms of the material cost and ionic conductivity.

Chapter 6 Concluding Remarks

In this thesis, I focused on the SEI film, and tried to elucidate its formation mechanism from a microscopic viewpoint at the atomic level by molecular simulation.

In Chapter 1, I described the problems of LIB for future application expansion. Especially, I discussed on the detail of the SEI film that provides a clue to solving the problem. The SEI film formation process is a complex research subject consisting of a lot of interfacial reactions at the non-equilibrium state during the device operation. To understand such complex phenomena, the use of computational chemistry is necessary as a complementary approach to the experiment. The purpose of this research is to provide the design guideline of the electrolyte in terms of the computational chemistry by clarifying the key factors contributing to the electrochemical stability of the electrolyte based on the molecular simulations.

In Chapter 2, I introduced an overview of computational chemistry, and described the details of the principle and theory of the molecular simulation methods used in this thesis.

In Chapter 3, to explore the conditions for the stable SEI film formation from a microscopic viewpoint, I focused on cyclic carbonates *t*-BC and *c*-BC, which are geometrical

isomers. SEI film formation in *t*-BC-based electrolyte and *c*-B*C*-based electrolytes were simulated by RM method. The results revealed that the SEI film formed in *c*-B*C*-based electrolytes contains fewer dimerized products, which are primary components of a good SEI film; this lower number of dimerized products can cause reduced film stability. As one of the origins of the decreased dimerization in *c*-BC, we identified the larger solvation energy of *c*-BC for the intermediate species and its smaller diffusion constant, which largely diminishes the dimerization. Moreover, the correlation between the Li^+ intercalation behavior and nature of the SEI film was found to be common for EC/PC and *t*-BC/*c*-BC electrolytes, confirming the importance of solvation of the intermediates and SEI film components in the stability of SEI film. These results suggest that use of solvents that satisfy both the weak solvation and low solubility is one possible way to stabilize the SEI film so as to achieve a better charge-discharge performance.

In Chapter 4, I dealt with Li hydrate melt, which is a novel aqueous electrolyte. In this study, to understand the origin of its high electrochemical stability, I investigated the solution structure and electronic states based on the FPMD. It was found that water molecules in the hydrate melt exist as isolated monomers or clusters consisting of only a few ($\leq$5) H_2O molecules. Both the monomers and clusters have electronic structures largely deviating from that in bulk water, where the lowest unoccupied states are higher in energy than that of the Li-salt anions, which preferentially causes anion reduction leading to formation of an anion-derived SEI film. This clearly shows the role of characteristic electronic structure inherent to the peculiar water environment for the extraordinary

electrochemical stability of hydrate melts.

!n Chapter 5, I focused on hydrate-melt electrolytes with other kinds of alkali cations, i.e., Na and K from an elemental strategic perspective. To obtain the design guidelines for Na and K hydrate-melt electrolytes, I investigated the microscopic origin of narrower potential window (lower electrochemical stability) of Na and K hydrate-melt electrolytes by using the FPMD. As a result, the solvation shell of the alkali cation became larger, weakening the coordination of H_2O molecules to cation/anion in the order of ion radius. Then, it was found that the weaker interaction between cations and H_2O molecules in the Na and K hydrate melts increases the number of H-bonds and enhances the aggregation of H_2O molecules. Furthermore, the strong association of water and weakened cation-anion Coulomb interaction should make the LUMO of anions unstable so as to prevent the anion-derived SEI film. Thus, to improve the electrochemical stability of Na and K hydrate-melt electrolytes, it may be required to further decrease the water content and add the additive which is able to suppress the water association.

Through this thesis, I proposed the basic guideline of electrolyte design by clarifying the microscopic mechanism of the electrochemical stability based on the molecular simulations. In summary,

1. The stability of the SEI film is strongly affected by both the generation and elution rate of the SEI components. From the viewpoint of the generation, the use of electrolyte solvent that weakly solvates to chemical species is effective so as not to

interfere with their production reaction and aggregation of the species contributing to the stable SEI film formation. It is also important to use a solvent that have low solubility of the SEI components.

2. In the aqueous electrolytes, there is a trade-off relationship between electrochemical stability and ionic conductivity. The use of alkali cation with strong Lewis acidity leads to the isolation of water and the formation of a stable anion-derived SEI film, while the ion transport ability is significantly deteriorated due to the strong interaction. It is essential to optimize the balance between the two. Especially in the case of aqueous electrolyte containig alkali cations with low Lewis acidity (e.g., K^+) as current carriers, it is worth conducting that researches to discover a novel additive that enhances both water isolation and transport ability of alkari cations. Once the studies completed, human begins could enjoy secondary batteries with much lower cost, more safety, and higher performance than the state-of-the-art LIBs.

These findings provide the guideline of material design toward the stable SEI film formation. The present simulations have clarified that the difference in the coordination structure depending on the geometric isomers and salt concentration greatly modulates the diffusion and electronic states of components in the electrolyte, and also strongly affects the SEI film formation. Namely, the SEI film formation process that governs the stability of the electrolyte is greatly influenced by behaviors of components in the electrolyte rather than the nature of each component. Therefore, to design the new electrolyte that forms good SEI film, the theoretical analyses based on the molecular simulations must be efficient

as a complementary approach to experiments.

Acknowledgements

I would like to express my gratitude to all people who have supported my Ph.D. course.

First of all, I would like to show my greatest appreciation to Professor Atsuo Yamada, who has offered continuing support and constant encouragement as supervisor. I was very impressed with his encyclopedic knowledge and skills to lead sophisticated discussions.

I would like to offer my special thanks as well to coauthors of my papers contained in this thesis. Hospitable support and encouragement from Professor Masataka Nagaoka (Nagoya University) were indispensable to conduct my study. Professor Yoshitaka Tateyama (National Institute for Materials Science) gave me a lot of knowledge of FPMD simulation and theoretical advice, which greatly improved my study. I have greatly benefited from Lecturer Yuki Yamada. His advice was always helpful to improve my work and papers. Assistant Professor Norio Takenaka cared a lot about my work and gave many valuable suggestions to me. Dr. Eriko Watanabe, former Assistant Professor of Yamada-Okubo group, has provided me with generous support since I joined this group.

Besides coauthors, I am also grateful to all stuffs, students, and alumni of Yamada-Okubo group for their helpful support. Associate Professor Masashi Okubo gave me

critical comments and advice from an objective point of view. Ms. Minako Koyama, Ms. Miwako Hiramine, Ms. Kazumi Suzuki, and Ms. Kuniko Yamaguchi supported my research activities as secretaries of Yamada-Okubo group. Without their guidance and persistent help, this thesis would not have been completed.

I would also like to thank Professor Hirotoshi Mori, Chuo University (former Associate Professor in Ochanomizu University), who was my supervisor in baccalaureate and master's degree program at Ochanomizu University and alumni of Mori group. Studies in Mori group were exciting and meaningful for me. The experience and knowledge obtained there helped me with conducting research activities in Yamada-Okubo group.

I owe a very important debt to Professor Kazuhiro Takanabe, Professor Akira Nakayama, Associate Professor Ryuji Kikuchi, Professor Hiromi Nakai (Waseda University) for giving me valuable advice to improve my thesis as vice chairs in my dissertation committee.

Finally, let me show a feeding of gratitude to my family for their heartfelt support.

Kasumi Miyazaki

Reference

[1] Matthew Li, Jun Lu, Zhongwei Chen, and Khalil Amine. 30 Years of Lithium-Ion Batteries. *Advanced Materials*, Vol. 30, No. 33, p. 1800561, aug 2018.

[2] J.-M. Tarascon and M Armand. Issues and challenges facing rechargeable lithium batteries. *Nature*, Vol. 414, p. 359, nov 2001.

[3] Languang Lu, Xuebing Han, Jianqiu Li, Jianfeng Hua, and Minggao Ouyang. A review on the key issues for lithium-ion battery management in electric vehicles. *Journal of Power Sources*, Vol. 226, pp. 272–288, 2013.

[4] Kai Liu, Yayuan Liu, Dingchang Lin, Allen Pei, and Yi Cui. Materials for lithium-ion battery safety. *Science Advances*, Vol. 4, No. 6, p. eaas9820, jun 2018.

[5] Qingsong Wang, Binbin Mao, Stanislav I Stoliarov, and Jinhua Sun. A review of lithium ion battery failure mechanisms and fire prevention strategies. *Progress in Energy and Combustion Science*, Vol. 73, pp. 95–131, 2019.

[6] Kang Xu. Electrolytes and interphases in Li-ion batteries and beyond. *Chemical Reviews*, Vol. 114, No. 23, pp. 11503–11618, 2014.

[7] Arthur von Cresce and Kang Xu. Electrolyte Additive in Support of 5 V Li Ion Chemistry. *Journal of The Electrochemical Society*, Vol. 158, No. 3, pp. A337–A342, mar 2011.

[8] Zhengcheng Zhang, Libo Hu, Huiming Wu, Wei Weng, Meiten Koh, Paul C Redfern, Larry A Curtiss, and Khalil Amine. Fluorinated electrolytes for 5 V lithium-ion battery chemistry. *Energy & Environmental Science*, Vol. 6, No. 6, pp. 1806–1810, 2013.

[9] Aiping Wang, Sanket Kadam, Hong Li, Siqi Shi, and Yue Qi. Review on modeling of the anode solid electrolyte interphase (SEI) for lithium-ion batteries. *npj Computational Materials*, Vol. 4, No. 1, p. 15, 2018.

[10] A N Dey and B P Sullivan. The Electrochemical Decomposition of Propylene Carbonate on Graphite. *Journal of The Electrochemical Society*, Vol. 117, No. 2, pp. 222–224, feb 1970.

[11] Rosamaría Fong, Ulrich von Sacken, and J R Dahn. Studies of Lithium Intercalation into Carbons Using Nonaqueous Electrochemical Cells. *Journal of The Electrochemical Society*, Vol. 137, No. 7, pp. 2009–2013, jul 1990.

[12] Tetsuya Osaka, Daikichi Mukoyama, and Hiroki Nara. Review–Development of Diagnostic Process for Commercially Available Batteries, Especially Lithium Ion Battery, by Electrochemical Impedance Spectroscopy. *Journal of The Electrochemical Society*, Vol. 162, No. 14, pp. A2529–A2537, jan 2015.

[13] S S Zhang, K Xu, and T R Jow. EIS study on the formation of solid electrolyte interface in Li-ion battery. *Electrochimica Acta*, Vol. 51, No. 8, pp. 1636–1640, 2006.

[14] Kang Xu. Nonaqueous Liquid Electrolytes for Lithium-Based Rechargeable Batteries. *Chemical Reviews*, Vol. 104, No. 10, pp. 4303–4418, 2004.

[15] Seong Jin An, Jianlin Li, Claus Daniel, Debasish Mohanty, Shrikant Nagpure, and David L Wood. The state of understanding of the lithium-ion-battery graphite solid electrolyte interphase (SEI) and its relationship to formation cycling. *Carbon*, Vol. 105, pp. 52–76, 2016.

[16] Rachid Yazami. Surface chemistry and lithium storage capability of the graphite-lithium electrode. *Electrochimica Acta*, Vol. 45, No. 1, pp. 87–97, 1999.

[17] Arthur v. Cresce, Selena M Russell, David R Baker, Karen J Gaskell, and Kang Xu. In Situ and Quantitative Characterization of Solid Electrolyte Interphases. *Nano Letters*, Vol. 14, No. 3, pp. 1405–1412, mar 2014.

[18] Rujia Zou, Zhe Cui, Qian Liu, Guoqiang Guan, Wenlong Zhang, Guanjie He, Jianmao Yang, and Junqing Hu. In situ transmission electron microscopy study of individual nanostructures during lithiation and delithiation processes. *Journal of Materials Chemistry A*, Vol. 5, No. 38, pp. 20072–20094, 2017.

[19] Gabriel M Veith, Mathieu Doucet, J Kevin Baldwin, Robert L Sacci, Tyler M Fears, Yongqiang Wang, and James F Browning. Direct Determination of Solid-Electrolyte

Interphase Thickness and Composition as a Function of State of Charge on a Silicon Anode. *The Journal of Physical Chemistry C*, Vol. 119, No. 35, pp. 20339–20349, sep 2015.

[20] Satu Kristiina Heiskanen, Jongjung Kim, and Brett L Lucht. Generation and Evolution of the Solid Electrolyte Interphase of Lithium-Ion Batteries. *Joule*, Vol. 3, No. 10, pp. 2322–2333, 2019.

[21] Victor A Agubra and Jeffrey W Fergus. The formation and stability of the solid electrolyte interface on the graphite anode. *Journal of Power Sources*, Vol. 268, pp. 153–162, 2014.

[22] Alejandro A Franco, Alexis Rucci, Daniel Brandell, Christine Frayret, Miran Gaberscek, Piotr Jankowski, and Patrik Johansson. Boosting Rechargeable Batteries R&D by Multiscale Modeling: Myth or Reality? *Chemical Reviews*, Vol. 119, No. 7, pp. 4569–4627, apr 2019.

[23] Mahesh Datt Bhatt and Colm O'Dwyer. Recent progress in theoretical and computational investigations of Li-ion battery materials and electrolytes. *Physical Chemistry Chemical Physics*, Vol. 17, No. 7, pp. 4799–4844, 2015.

[24] Tao Li and Perla B Balbuena. Theoretical studies of the reduction of ethylene carbonate. *Chemical Physics Letters*, Vol. 317, No. 3, pp. 421–429, 2000.

[25] Doron Aurbach, Mikhail D Levi, Elena Levi, and Alexander Schechter. Failure and Stabilization Mechanisms of Graphite Electrodes. *The Journal of Physical Chemistry B*, Vol. 101, No. 12, pp. 2195–2206, mar 1997.

[26] Masamichi Onuki, Shinichi Kinoshita, Yuuichi Sakata, Miwa Yanagidate, Yumiko Otake, Makoto Ue, and Masaki Deguchi. Identification of the Source of Evolved Gas in Li-Ion Batteries Using 13C-labeled Solvents. *Journal of The Electrochemical Society*, Vol. 155, No. 11, pp. A794–A797, nov 2008.

[27] Kevin Leung and Joanne L Budzien. Ab initio molecular dynamics simulations of the initial stages of solid-electrolyte interphase formation on lithium ion battery graphitic anodes. *Physical Chemistry Chemical Physics*, Vol. 12, No. 25, pp. 6583–6586, 2010.

[28] Keisuke Ushirogata, Keitaro Sodeyama, Yukihiro Okuno, and Yoshitaka Tateyama. Additive Effect on Reductive Decomposition and Binding of Carbonate-Based Solvent toward Solid Electrolyte Interphase Formation in Lithium-Ion Battery. *Journal of the American Chemical Society*, Vol. 135, No. 32, pp. 11967–11974, aug 2013.

[29] Adri C T van Duin, Siddharth Dasgupta, Francois Lorant, and William A Goddard. ReaxFF: A Reactive Force Field for Hydrocarbons. *The Journal of Physical Chemistry A*, Vol. 105, No. 41, pp. 9396–9409, oct 2001.

[30] Hiroaki Nishizawa, Yoshifumi Nishimura, Masato Kobayashi, Stephan Irle, and Hiromi Nakai. Three pillars for achieving quantum mechanical molecular dynamics simulations of huge systems: Divide-and-conquer, density-functional tight-binding, and massively parallel computation. *Journal of Computational Chemistry*, Vol. 37, No. 21, pp. 1983–1992, aug 2016.

[31] Chien-Pin Chou, Aditya Wibawa Sakti, Yoshifumi Nishimura, and Hiromi Nakai. Development of Divide-and-Conquer Density-Functional Tight-Binding Method for

Theoretical Research on Li-Ion Battery. *The Chemical Record*, Vol. 19, No. 4, pp. 746–757, apr 2019.

[32] Kyosuke Doi, Yuki Yamada, Masaki Okoshi, Junichi Ono, Chien-Pin Chou, Hiromi Nakai, and Atsuo Yamada. Reversible Sodium Metal Electrodes: Is Fluorine an Essential Interphasial Component? *Angewandte Chemie International Edition*, Vol. 58, No. 24, pp. 8024–8028, jun 2019.

[33] Masaki Okoshi, Chien-Pin Chou, and Hiromi Nakai. Theoretical Analysis of Carrier Ion Diffusion in Superconcentrated Electrolyte Solutions for Sodium-Ion Batteries. *The Journal of Physical Chemistry B*, Vol. 122, No. 9, pp. 2600–2609, mar 2018.

[34] Qifeng Zheng, Shota Miura, Kasumi Miyazaki, Seongjae Ko, Eriko Watanabe, Masaki Okoshi, Chien-Pin Chou, Yoshifumi Nishimura, Hiromi Nakai, Takeshi Kamiya, Tsunetoshi Honda, Jun Akikusa, Yuki Yamada, and Atsuo Yamada. Sodium- and Potassium-Hydrate Melts Containing Asymmetric Imide Anions for High-Voltage Aqueous Batteries. *Angewandte Chemie International Edition*, Vol. 58, No. 40, pp. 14202–14207, oct 2019.

[35] Masataka Nagaoka, Yuichi Suzuki, Takuya Okamoto, and Norio Takenaka. A hybrid MC/MD reaction method with rare event-driving mechanism: Atomistic realization of 2-chlorobutane racemization process in DMF solution. *Chemical Physics Letters*, Vol. 583, pp. 80–86, 2013.

[36] Takuya Fujie, Norio Takenaka, Yuichi Suzuki, and Masataka Nagaoka. Red Moon methodology compatible with quantum mechanics/molecular mechanics framework:

Application to solid electrolyte interphase film formation in lithium-ion battery system. *The Journal of Chemical Physics*, Vol. 149, No. 4, p. 044113, jul 2018.

[37] Norio Takenaka, Yuichi Suzuki, Hirofumi Sakai, and Masataka Nagaoka. On electrolyte-dependent formation of solid electrolyte interphase film in lithium-ion batteries: Strong sensitivity to small structural difference of electrolyte molecules. *Journal of Physical Chemistry C*, Vol. 118, No. 20, pp. 10874–10882, 2014.

[38] Norio Takenaka, Hirofumi Sakai, Yuichi Suzuki, Purushotham Uppula, and Masataka Nagaoka. A Computational Chemical Insight into Microscopic Additive Effect on Solid Electrolyte Interphase Film Formation in Sodium-Ion Batteries: Suppression of Unstable Film Growth by Intact Fluoroethylene Carbonate. *Journal of Physical Chemistry C*, Vol. 119, No. 32, pp. 18046–18055, 2015.

[39] Amine Bouibes, Norio Takenaka, Takuya Fujie, Kei Kubota, Shinichi Komaba, and Masataka Nagaoka. Concentration Effect of Fluoroethylene Carbonate on the Formation of Solid Electrolyte Interphase Layer in Sodium-Ion Batteries. *ACS Applied Materials & Interfaces*, Vol. 10, No. 34, pp. 28525–28532, 2018.

[40] Amine Bouibes, Norio Takenaka, Soumen Saha, and Masataka Nagaoka. Microscopic Origin of the Solid Electrolyte Interphase Formation in Fire-Extinguishing Electrolyte: Formation of Pure Inorganic Layer in High Salt Concentration. *The Journal of Physical Chemistry Letters*, Vol. 10, No. 19, pp. 5949–5955, oct 2019.

[41] Norio Takenaka, Takuya Fujie, Amine Bouibes, Yuki Yamada, Atsuo Yamada, and Masataka Nagaoka. Microscopic Formation Mechanism of Solid Electrolyte Inter-

phase Film in Lithium-Ion Batteries with Highly Concentrated Electrolyte. *Journal of Physical Chemistry C*, Vol. 122, No. 5, pp. 2564–2571, 2018.

[42] Andrew R Leach and Andrew R Leach. *Molecular modelling: principles and applications*. Pearson education, 2001.

[43] Attila Szabo and Neil S Ostlund. *Modern quantum chemistry: introduction to advanced electronic structure theory*. Courier Corporation, 2012.

[44] Frank Jensen. *Introduction to computational chemistry*. John wiley & sons, 2017.

[45] R Car and M Parrinello. Unified Approach for Molecular Dynamics and Density-Functional Theory. *Physical Review Letters*, Vol. 55, No. 22, pp. 2471–2474, nov 1985.

[46] Dominik Marx and Jürg Hutter. *Ab initio molecular dynamics: basic theory and advanced methods*. Cambridge University Press, 2009.

[47] Michiel Sprik and Giovanni Ciccotti. Free energy from constrained molecular dynamics. *The Journal of Chemical Physics*, Vol. 109, No. 18, pp. 7737–7744, nov 1998.

[48] E A Carter, Giovanni Ciccotti, James T Hynes, and Raymond Kapral. Constrained reaction coordinate dynamics for the simulation of rare events. *Chemical Physics Letters*, Vol. 156, No. 5, pp. 472–477, 1989.

[49] Bernd Ensing, Alessandro Laio, Michele Parrinello, and Michael L Klein. A Recipe for the Computation of the Free Energy Barrier and the Lowest Free Energy Path of

Concerted Reactions. *The Journal of Physical Chemistry B*, Vol. 109, No. 14, pp. 6676–6687, apr 2005.

[50] Yuichi Suzuki, Yoshiyuki Koyano, and Masataka Nagaoka. Influence of Monomer Mixing Ratio on Membrane Nanostructure in Interfacial Polycondensation: Application of Hybrid MC/MD Reaction Method with Minimum Bond Convention. *The Journal of Physical Chemistry B*, Vol. 119, No. 22, pp. 6776–6785, jun 2015.

[51] Kentaro Matsumoto, Masayoshi Takayanagi, Yuichi Suzuki, Nobuaki Koga, and Masataka Nagaoka. Atomistic chemical computation of Olefin polymerization reaction catalyzed by (pyridylamido)hafnium(IV) complex: Application of Red Moon simulation. *Journal of Computational Chemistry*, Vol. 40, No. 2, pp. 421–429, jan 2019.

[52] P B Balbuena and Y Wang. *Lithium-ion Batteries: Solid-electrolyte Interphase*. Imperial College Press, 2004.

[53] Pallavi Verma, Pascal Maire, and Petr Novák. A review of the features and analyses of the solid electrolyte interphase in Li-ion batteries. *Electrochimica Acta*, Vol. 55, No. 22, pp. 6332–6341, 2010.

[54] Lidan Xing, Xiongwen Zheng, Marshall Schroeder, Judith Alvarado, Arthur von Wald Cresce, Kang Xu, Qianshu Li, and Weishan Li. Deciphering the Ethylene Carbonate-Propylene Carbonate Mystery in Li-Ion Batteries. *Accounts of Chemical Research*, Vol. 51, No. 2, pp. 282–289, feb 2018.

[55] Geun-Chang Chung, Hyung-Jin Kim, Seung-Il Yu, Song-Hui Jun, Jong-wook Choi, and Myung-Hwan Kim. Origin of Graphite Exfoliation An Investigation of the Important Role of Solvent Cointercalation. *Journal of The Electrochemical Society*, Vol. 147, No. 12, p. 4391, 2000.

[56] Geun-chang Chung. Reconsideration of SEI stability : reversible lithium intercalation into graphite electrodes in trans-2 , 3-butylene carbonate. *Journal of Power Sources*, Vol. 104, pp. 7–12, 2002.

[57] Geun Chang Chung, Hyeong Jin Kim, Song Hui Jun, and Myung Hwan Kim. New cyclic carbonate solvent for lithium ion batteries: Trans-2,3-butylene carbonate. *Electrochemistry Communications*, Vol. 1, No. 10, pp. 493–496, 1999.

[58] P Ganesh, P R C Kent, and De-en Jiang. Solid-Electrolyte Interphase Formation and Electrolyte Reduction at Li-Ion Battery Graphite Anodes: Insights from First-Principles Molecular Dynamics. *The Journal of Physical Chemistry C*, Vol. 116, No. 46, pp. 24476–24481, nov 2012.

[59] D Aurbach, B Markovsky, A Shechter, Y Ein-Eli, and H Cohen. A Comparative Study of Synthetic Graphite and Li Electrodes in Electrolyte Solutions Based on Ethylene Carbonate-Dimethyl Carbonate Mixtures. *Journal of The Electrochemical Society*, Vol. 143, No. 12, pp. 3809–3820, 1996.

[60] David Case, Thomas Darden, Thomas Cheatham, Carlos Simmerling, J Wang, Robert Duke, Ray Luo, Kenneth Merz, David Pearlman, Michael Crowley, R C Walker, W Zhang, Bing Wang, Seth Hayik, A E. Roitberg, Gustavo Seabra, K F Wong,

F Paesani, Xiongwu Wu, and P A Kollman. Amber 9, University of California, San Francisco, 2006.

[61] D A Case, D S Cerutti, T E Cheateham, T A Darden, R E Duke, T J Giese, H Gohlke, A W Goetz, D Greene, N Homeyer, and Others. AMBER16. 2016.

[62] Junmei Wang, Romain M Wolf, James W Caldwell, Peter A Kollman, and David A Case. Development and testing of a general amber force field. *Journal of Computational Chemistry*, Vol. 25, No. 9, pp. 1157–1174, 2004.

[63] Zhiping Liu, Shiping Huang, and Wenchuan Wang. A Refined Force Field for Molecular Simulation of Imidazolium-Based Ionic Liquids. *The Journal of Physical Chemistry B*, Vol. 108, No. 34, pp. 12978–12989, 2004.

[64] Christopher I Bayly, Piotr Cieplak, Wendy Cornell, and Peter A Kollman. A well-behaved electrostatic potential based method using charge restraints for deriving atomic charges: the RESP model. *The Journal of Physical Chemistry*, Vol. 97, No. 40, pp. 10269–10280, oct 1993.

[65] Jean-Paul Ryckaert, Giovanni Ciccotti, and Herman J C Berendsen. Numerical integration of the cartesian equations of motion of a system with constraints: molecular dynamics of n-alkanes. *Journal of Computational Physics*, Vol. 23, No. 3, pp. 327–341, 1977.

[66] H J C Berendsen, J P M Postma, W F van Gunsteren, A DiNola, and J R Haak. Molecular dynamics with coupling to an external bath. *The Journal of Chemical Physics*, Vol. 81, No. 8, pp. 3684–3690, oct 1984.

[67] Kikuko Hayamizu, Yuichi Aihara, Shigemasa Arai, and Cirilo Garcia Martinez. Pulse-Gradient Spin-Echo 1H, 7Li, and 19F NMR Diffusion and Ionic Conductivity Measurements of 14 Organic Electrolytes Containing LiN(SO2CF3)2. *The Journal of Physical Chemistry B*, Vol. 103, No. 3, pp. 519–524, jan 1999.

[68] Kazutaka Kondo, Mitsuru Sano, Akio Hiwara, Takehiko Omi, Miho Fujita, Akio Kuwae, Masayasu Iida, Koichi Mogi, and Haruhiko Yokoyama. Conductivity and Solvation of Li+ Ions of LiPF6 in Propylene Carbonate Solutions. *The Journal of Physical Chemistry B*, Vol. 104, No. 20, pp. 5040–5044, may 2000.

[69] Kang Xu. Whether EC and PC Differ in Interphasial Chemistry on Graphitic Anode and How. *Journal of The Electrochemical Society*, Vol. 156, No. 9, pp. A751–A755, sep 2009.

[70] Ali Eftekhari. High-Energy Aqueous Lithium Batteries. *Advanced Energy Materials*, Vol. 1801156, p. 1801156, 2018.

[71] Yuki Yamada. Developing New Functionalities of Superconcentrated Electrolytes for Lithium-ion Batteries. *Electrochemistry*, Vol. 85, No. 9, pp. 559–565, 2017.

[72] Yuki Yamada, Keizo Furukawa, Keitaro Sodeyama, Keisuke Kikuchi, Makoto Yaegashi, Yoshitaka Tateyama, and Atsuo Yamada. Unusual Stability of Acetonitrile-Based Superconcentrated Electrolytes for Fast-Charging Lithium-Ion Batteries. *Journal of the American Chemical Society*, Vol. 136, No. 13, pp. 5039–5046, apr 2014.

[73] Keitaro Sodeyama, Yuki Yamada, Koharu Aikawa, Atsuo Yamada, and Yoshitaka Tateyama. Sacrificial Anion Reduction Mechanism for Electrochemical Stability

Improvement in Highly Concentrated Li-Salt Electrolyte. *The Journal of Physical Chemistry C*, Vol. 118, No. 26, pp. 14091–14097, jul 2014.

[74] Liumin Suo, Oleg Borodin, Tao Gao, Marco Olguin, Janet Ho, Xiulin Fan, Chao Luo, Chunsheng Wang, and Kang Xu. "Water-in-salt" electrolyte enables high-voltage aqueous lithium–on chemistries. *Science*, Vol. 350, No. 6263, pp. 938 LP – 943, nov 2015.

[75] Yuki Yamada, Kenji Usui, Keitaro Sodeyama, Seongjae Ko, Yoshitaka Tateyama, and Atsuo Yamada. Hydrate-melt electrolytes for high-energy-density aqueous batteries. *Nature Energy*, Vol. 1, p. 16129, aug 2016.

[76] CPMD, http://www.cpmd.org/.

[77] P.J. Linstrom and W.G. Mallard. *NIST Chemistry WebBook, NIST Standard Reference Database Number 69*.

[78] Shuichi Nosé. A unified formulation of the constant temperature molecular dynamics methods. *The Journal of Chemical Physics*, Vol. 81, No. 1, pp. 511–519, jul 1984.

[79] Stefan Grimme. Semiempirical GGA-type density functional constructed with a long-range dispersion correction. *Journal of Computational Chemistry*, Vol. 27, No. 15, pp. 1787–1799, nov 2006.

[80] S Goedecker, M Teter, and J Hutter. Separable dual-space Gaussian pseudopotentials. *Physical Review B*, Vol. 54, No. 3, pp. 1703–1710, jul 1996.

[81] M Krack. Pseudopotentials for H to Kr optimized for gradient-corrected exchange-correlation functionals. *Theoretical Chemistry Accounts*, Vol. 114, No. 1, pp. 145–152, 2005.

[82] Debostuti Ghoshdastidar and Sanjib Senapati. Ion-water wires in imidazolium-based ionic liquid/water solutions induce unique trends in density. *Soft Matter*, Vol. 12, No. 12, pp. 3032–3045, 2016.

[83] Debostuti Ghoshdastidar and Sanjib Senapati. Nanostructural Reorganization Manifests in Sui-Generis Density Trend of Imidazolium Acetate/Water Binary Mixtures. *Journal of Physical Chemistry B*, Vol. 119, No. 34, pp. 10911–10920, 2015.

[84] A K Soper. The radial distribution functions of water and ice from 220 to 673 K and at pressures up to 400 MPa. *Chemical Physics*, Vol. 258, No. 2, pp. 121–137, 2000.

[85] K Laasonen, M Sprik, M Parrinello, and R Car. "Ab initio" liquid water. *The Journal of Chemical Physics*, Vol. 99, No. 11, pp. 9080–9089, dec 1993.

[86] Jared D Smith, Christopher D Cappa, Kevin R Wilson, Benjamin M Messer, Ronald C Cohen, and Richard J Saykally. Energetics of Hydrogen Bond Network Rearrangements in Liquid Water. *Science*, Vol. 306, No. 5697, pp. 851 LP – 853, oct 2004.

[87] Joonhyung Lim, Kwanghee Park, Hochan Lee, Jungyu Kim, Kyungwon Kwak, and Minhaeng Cho. Nanometric Water Channels in Water-in-Salt Lithium Ion Battery Electrolyte. *Journal of the American Chemical Society*, Vol. 140, No. 46, pp. 15661–15667, nov 2018.

[88] Oleg Borodin, Liumin Suo, Mallory Gobet, Xiaoming Ren, Fei Wang, Antonio Faraone, Jing Peng, Marco Olguin, Marshall Schroeder, Michael S. Ding, Eric Gobrogge, Arthur Von Wald Cresce, Stephen Munoz, Joseph A. Dura, Steve Greenbaum, Chunsheng Wang, and Kang Xu. Liquid Structure with Nano-Heterogeneity Promotes Cationic Transport in Concentrated Electrolytes. *ACS Nano*, Vol. 11, No. 10, pp. 10462–10471, 2017.

[89] Jenel Vatamanu and Oleg Borodin. Ramifications of Water-in-Salt Interfacial Structure at Charged Electrodes for Electrolyte Electrochemical Stability. *Journal of Physical Chemistry Letters*, Vol. 8, No. 18, pp. 4362–4367, 2017.

[90] Liumin Suo, Dahyun Oh, Yuxiao Lin, Zengqing Zhuo, Oleg Borodin, Tao Gao, Fei Wang, Akihiro Kushima, Ziqiang Wang, Ho-Cheol Kim, Yue Qi, Wanli Yang, Feng Pan, Ju Li, Kang Xu, and Chunsheng Wang. How Solid-Electrolyte Interphase Forms in Aqueous Electrolytes. *Journal of the American Chemical Society*, Vol. 139, No. 51, pp. 18670–18680, dec 2017.

[91] Yoshitaka Tateyama, Jochen Blumberger, Michiel Sprik, and Ivano Tavernelli. Density-functional molecular-dynamics study of the redox reactions of two anionic, aqueous transition-metal complexes. *The Journal of Chemical Physics*, Vol. 122, No. 23, p. 234505, jun 2005.

[92] Pekka Peljo and Hubert H Girault. Electrochemical potential window of battery electrolytes: the HOMO-LUMO misconception. *Energy & Environmental Science*, Vol. 11, No. 9, pp. 2306–2309, 2018.

[93] David Prendergast, Jeffrey C Grossman, and Giulia Galli. The electronic structure of liquid water within density-functional theory. *The Journal of Chemical Physics*, Vol. 123, No. 1, p. 14501, jul 2005.

[94] Seongjae Ko, Yuki Yamada, Kasumi Miyazaki, Tatau Shimada, Eriko Watanabe, Yoshitaka Tateyama, Takeshi Kamiya, Tsunetoshi Honda, Jun Akikusa, and Atsuo Yamada. Lithium-salt monohydrate melt: A stable electrolyte for aqueous lithium-ion batteries. *Electrochemistry Communications*, Vol. 104, p. 106488, 2019.

[95] Kasumi Miyazaki, Norio Takenaka, Eriko Watanabe, Shota Iizuka, Yuki Yamada, Yoshitaka Tateyama, and Atsuo Yamada. First-Principles Study on the Peculiar Water Environment in a Hydrate-Melt Electrolyte. *The Journal of Physical Chemistry Letters*, pp. 6301–6305, sep 2019.

[96] Yizhak Marcus. Thermodynamics of solvation of ions. Part 5.–Gibbs free energy of hydration at 298.15 K. *Journal of the Chemical Society, Faraday Transactions*, Vol. 87, No. 18, pp. 2995–2999, 1991.